TUNING THE RESONANCES OF HIGH Q-FACTOR WHISPERING GALLERY MODE RESONATORS FOR OPTOELECTRONIC APPLICATIONS

A DISSERTATION SUBMITTED TO

THE GRADUATE SCHOOL OF ENGINEERING AND SCIENCE

OF BILKENT UNIVERSITY

IN PARTIAL FULFILLMENT OF THE REQUIREMENTS FOR

THE DEGREE OF

DOCTOR OF PHILOSOPHY

IN

MATERIALS SCIENCE AND NANOTECHNOLOGY

By

Ersin Hüseyinoğlu

July 2022

TUNING THE RESONANCES OF HIGH Q-FACTOR WHISPERING GALLERY MODE RESONATORS FOR OPTOELECTRONIC APPLICATIONS

By Ersin Hüseyinoğlu

July 2022

We certify that we have read this dissertation and that in our opinion it is fully adequate, in scope and in quality, as a dissertation for the degree of Doctor of Philosophy.

Bülend Ortaç(Advisor)

Aykutlu Dâna(Co-Advisor)

F. Ömer İlday

Alpan Bek

İbrahim Sarpkaya

Hamza Kurt

Approved for the Graduate School of Engineering and Science:

Orhan Arıkan
Director of the Graduate School

ABSTRACT

TUNING THE RESONANCES OF HIGH Q-FACTOR WHISPERING GALLERY MODE RESONATORS FOR OPTOELECTRONIC APPLICATIONS

Ersin Hüseyinoğlu
Ph.D. in Materials Science and Nanotechnology
Advisor: Bülend Ortaç
Co-Advisor: Aykutlu Dâna
July 2022

Optical resonators allow highly efficient light-matter interaction; therefore, they are promising tools for optoelectronics and photonics. Especially optical resonators with high Q-factors such as toroidal resonators can be instrumentalized to develop efficient light sources, modulators, converters, and sensitive detectors. They are already being used for photonics research; however, some significant obstacles hinder their mass utilization in the industry. One of those obstacles is the current limitations of the fabrication method used to produce toroidal resonators. Due to the method used to achieve surface tension-induced microresonators (STIM), their fabrication is time-consuming. A new approach was presented to mass-produce STIMs. Instead of a fixed position laser, a raster scan laser was used to reflow the microresonators with different geometry types to overcome the mass-fabrication limitations. As a result, high-Q-factor (10^6) toroidal resonators were fabricated. Reflowing of elliptical and racetrack resonators were also demonstrated. Another problem that hinders the utilization of toroidal resonators is their high susceptibility to any errors originating from the fabrication process. Any deviation from the designed parameters leads to resonators with different resonant modes. A method for post-production tuning resonant mode of chalcogenide coated resonator was demonstrated. By using a thin $Ge_2Sb_2Te_5$ layer coated silica toroidal resonator, 0.01 nm and 0.02 nm permanent mode shifts were achieved from 5 nm thick coated and 10 nm thick coated resonators, respectively.

Keywords: Optical Resonators, Surface Tension-Induced Resonators, Optical Fiber Tapering, Light Coupling, Chalcogenide glasses, Photonics, Microtoroids, Resonant Mode Shift, Resonant Mode Tuning, Whispering Gallery Modes.

ÖZET

OPTOELEKTRONİK UYGULAMALAR İÇİN YÜKSEK K-FAKTÖRLÜ OPTİK MİKROREZONATÖRLERİN REZONANT MODLARININ DEĞİŞTİRİLMESİ

Ersin Hüseyinoğlu
Malzeme Bilimi ve Nanoteknoloji, Doktora
Tez Danışmanı: Bülend Ortaç
İkinci Tez Danışmanı: Aykutlu Dâna
Temmuz 2022

Yüksek ışık-madde etkileşimine izin verdikleri için, optik rezonatörler, fotonik ve optoelektronikte kullanım için gelecek vaadeden yapılardır. Yüksek kalite faktörüne sahip mikrorezonatörlerin kullanılması ile, verimli ışık kaynakları, ışık dönüştürücü ve modülatörleri, ve çok duyarlı algılayıcıların geliştirilmesi mümkündür. Optik rezonatörler, fotonik araştırmalarında kullanılıyor olsa da, bazı engeller sebebi ile ticari uygulamalarda yaygın bir şekilde kullanılmamaktadır. Bu engellerden biri, toroid rezonatörlerin üretiminde kullanılan metodların günümüzdeki teknik kısıtlamalarıdır. Yüzey gerilimi ile üretilmiş rezonatörlerin yapılması oldukça zaman alan bir süreçtir. Bu tip rezonatörlerin toplu olarak üretimi için yeni bir metod önerilmiştir. Sabit hizalı bir lazer yerine, tarama şablonlu bir lazer kullanılarak farklı geometrilerde rezonatörler toplu olarak ısıtılıp yeniden şekillendirilmiştir. Bu şekilde eliptik ve parkur şekilli rezonatörler elde edildiği gibi, 10^6 yüksek kalite faktörlü toroid rezonatörler de elde edilmiştir. Toroid rezonatörlerin yaygın bir şekilde kullanılmasının önünde duran bir diğer engel de, bu yapıların üretim sürecinden kaynaklı hatalara karşı oldukça hassas olmasıdır. Planlanan parametrelerden herhangi bir sapma durumunda, rezonant modları istenilenden farklı rezonatörlerin elde edilmesi ile sonuçlanır. Üretim sonrası rezonant modların kalıcı olarak ayarlanması için bir yöntem önerilmiştir. Silika toroid rezonatörler, 5 nm ve 10 nm olmak üzere iki farklı kalınlıkta $Ge_2Sb_2Te_5$ tabakası ile kaplanmıştır. Kaplı rezonatörlerin rezonant modları, önerilen yöntem ile, kalıcı olarak ayarlanmıştır.

Anahtar sözcükler: Optik Rezonatörler, Yüzey Gerilimi ile üretilmiş Rezonatörler, Optik Fiber Çekimi, Işık Bağdaştırma, Kalkojen camlar, Fotonik, Mikrotoroid, Rezonant Mod Kayması, Rezonant Mod Değişimi, Fısıldayan Galeri Modları.

Acknowledgement

First and foremost, I thank my dear family, my father Serhan Hüseyinoğlu, mother Tülay Hüseyinoğlu, sister Serap Saray, brother Erdem Hüseyinoğlu, and cousin Ece Atambay Ertürk, for their never-ending, consistent mental and spiritual support. Similar to all doctoral candidates in the world, I experienced troubling times during my PhD. My family was always there whenever I needed them. Their very existence and moral support gave me the strength that I needed. Thanks to their patience and support, it was possible to overcome the depressing times and find my way to achieve my goals. I also thank Gül Tunç, Gamze Tunç and Dilara Gökçen Buldu for their continuous moral support and encouragement. Their encouragement and words helped me over the years. Also, it was a joyful experience to know Buse Nur Buldu (*rest in peace*).

Similarly, I would like to remark my thankfulness to my academic advisor, Dr. Bülend Ortaç, for the solid support that he provided to me and his guidance and backing during my studies. His motivation helped me overcome some of the obstacles of my own making. Dr. Aykutlu Dâna also has my same appreciation for his continuous support and guidance. I am thankful to Dr. Bülend Ortaç and Dr. Aykutlu Dâna for their support, advice, and motivation. I thank Dr. F. Ömer İlday and Dr. Alpan Bek for their valuable feedback during academic discussions regarding my studies. I also thank to Dr. Hamza Kurt and Dr. İbrahim Sarpkaya for their participation, valuable input and support.

I would also like to thank my dear friends for their kindness, friendship, and support. Like family bonds, friendship is precious, and one may consider oneself lucky if surrounded by kind, honest, loyal, and understanding friends. I want to express my gratitude to Çetin Can Şahin, Eser Özkoçak, Mustafa Biçer, Duygu Torun, Dr. Erol Özgür, Ekin T. Tireki, İkra Gizem Yıldız, Esra Kendir, Esra Karaaslan, Dr. Hasan Yılmaz for their support during my studies. Çetin, Eser, Mustafa, and Duygu are my long-time friends, and I am happy to say that our bond is still solid after all these years. Even physical distance did not prevent Eser and Duygu from extending their constant moral support and friendship. I am thankful for their support and precious friendship over the years. Erol is the first friend I gained at Bilkent University. I am grateful not only for the

long academic discussions we had but also for his kind friendship, understanding, and never-ending support. Ekin is a precious friend that never wavered in her support for me. She was always there when I needed it, and the words may fail me if I try to express my gratitude for her company. İkra is a very dear friend, and I am happy to meet a kind soul like her at Bilkent. I always enjoyed her friendship and appreciated her moral support. Her companionship is something that I treasure. Esra Kendir and Esra Karaaslan are very dear friends, and I am pleased to meet them at Bilkent University. Their friendship and support helped me during the writing of the thesis. I hope they will remember my jokes fondly. My friends' friendship and support helped me immensely during my studies and troubled times, and I am grateful. It is my hope that these ties will continue as strong as it is.

I also thank my colleagues and friends in the Ortaç Research Group. Elif Yapar Yıldırım, Dr. Ali Karatutlu, and Seyit Ali Yaşar for their friendship, support, and both social and academic talks and discussions. I immensely enjoyed the fun and long conversations with Elif and Ali, and I appreciate their support and companionship. I would also like to thank Dr. Gökhan Bakan for his assistance during my studies and experiments. In a similar manner, I would like to thank my colleagues with whom I experienced working, Dr. Adem Yıldırım, Fahri Emre Öztürk, Bihter Dağlar (*rest in peace*), Dr. Tural Khudiyev, Ayşegül Abdelal, Dilara Öztürk, Neşe Özgür, Murat Dere, Dr. Pınar Beyazkılıç, Dr. Ozan Aktaş, Dr. Pelin Tören Özgün. I thank them for their friendship and support.

I would like to express my gratitude to The Scientific and Technological Research Council of Turkey, TÜBİTAK, for the Ph.D. Scholarship I have benefited throughout my studies. I also thank Bilkent University and The National Nanotechnology Research Center for the infrastructure they provided for my studies.

As the last word, I dedicate my thesis to my parents and all graduate students. The support of my parents was crucial, so this is my way of thanking them. The enthusiasm and curiosity of graduate students are indispensable and irreplaceable in research and development. It is frustrating that their physical and mental health, as well as happiness in social life, are mostly ignored by the scientific community in the grand scheme of things. I hope all graduate students will succeed in their studies and get what they deserve soon.

In the realm of ideas, everything
depends on enthusiasm . . .
In the real world, all rests on
perseverance.

Johann Wolfgang von Goethe

Contents

1 Introduction **1**

1.1 Light and the Emergence of the Optical Resonators 1

1.2 Thesis Outline 3

2 Optical Microresonators **4**

2.1 Introduction 4

2.2 Resonator Types 5

2.3 Resonator Theory 9

2.3.1 Electromagnetic Theory of Whispering Gallery Modes . . . 13

2.3.2 Free Spectral Range 15

2.3.3 Quality Factor (Q-Factor) and Mode Volume 16

2.4 Microtoroid Fabrication 17

3 Optical Fiber Tapering and Light Coupling **28**

3.1 Light Coupling 28

3.2 Evanescent Field Coupling 31

3.3 Fiber Tapering 34

3.3.1 Fiber Tapering with Carbondioxide Laser 35

3.3.2 Fiber Tapering with Hydrogen Torch 39

4 Mass Production of Toroidal Resonators by Fast Reflowing with Scanning LASER **44**

4.1 Fabrication Process of Silica Toroidal Resonator and Its Limitations 44

4.2 Mass Reflowing by Using Commercial CO_2 Laser Engraver 47

4.2.1 LASER Engraver 48

4.2.2 Fabrication Process and Reflowing 50

5 Permanent Shift on Resonant Modes of Chalcogenide Coated Silica Microtoroids 57
5.1 Chalcogenides 59
5.2 Fabrication of Chalcogenide Coated Silica Resonators 61
5.3 Permanent Mode Tuning 65

6 Conclusions 71

List of Figures

2.1 Schematic representation of a Fabry-Perot (two-mirror planar) resonator. 6
2.2 Drawing of a disk resonator on a pillar. 7
2.3 Drawing of a ring resonator on a substrate. 7
2.4 Drawing of a toroidal resonator on a pillar. 8
2.5 Light rays in a circular resonator. 9
2.6 Ray path in circular geometry due to TIR. 10
2.7 Resonant modes represented by each peak and free spectral range between consecutive modes. 15
2.8 Spin Coating of a silicon substrate (gray color) with a thermal oxide layer (blue color) on top. (a) Diced substrate, (b) HMDS (yellow color) spin-coated substrate, (c) Photoresist (red color) coated substrate. 18
2.9 Graphical representation of one of the masks used. Black circles are the chromium layer on the mask, while the rest of the mask is transparent to allow ultraviolet light to pass through. 19
2.10 (a) UV Photolithography was done on the substrate, followed by (b) the developing process. 20
2.11 (a) Developed substrate with photoresist patterns on it, (b) Substrate after silica etching. 20
2.12 Silica microdisk on a silicon pillar after silicon etching by SF_6, following a dry etch process achieved by inductively coupled plasma technique. 21
2.13 Wedged silica microdisk on a silicon pillar after silicon etching by SF_6, following a wet etch process achieved by buffered oxide etchant. 22

2.14 Optical microscopy images of a substrate. (a) After photolithography (5X objective). (b) After silica etching by HF (5X objective). (c) After silica etching by HF (100X objective). 23
2.15 Isotropic etching of silicon layer under the silica disk. (a) Before silicon etching, (b) After silicon etching. 24
2.16 Illustration of the disk reflowing setup with carbondioxide laser. . 25
2.17 Toroidal resonators formed from silica disk resonators by the reflowing process. (a) Disk resonator, (b) Toroidal resonator after reflowing 26
2.18 SEM images of a fabricated silica toroidal resonator from (a) top view, (b) side view, (c) tilted view. 26
2.19 Tilted SEM image of a fabricated silica toroidal resonator. 27

3.1 Optical fiber half coupler utilized to couple light into the spherical resonator. 29
3.2 Incident light coupled into a spherical resonator by using a prism. 30
3.3 Light coupling into the toroidal resonator by using tapered optical fiber. 31
3.4 Top view of a schematic of an evanescent field coupling from tapered optical fiber into a resonator. 33
3.5 Illustration of an SMF-28 optical fiber detailing core (blue colored), cladding (light blue colored), and coating (light gray colored). . . 35
3.6 Fiber tapering setup with carbondioxide laser. The output of the diode laser is plugged to silica fiber and the other end of the silica fiber is plugged to the photodetector connected to the power meter. 2 cm. length of the fiber's coating is removed and that bare fiber is fixed between two fiber holders on two oppositely aligned linear piezeo stages. CO_2 laser and lens are aligned on top of the bare fiber. 36
3.7 The zinc selenide lens in the fiber tapering setup required to control the heating zone. 37
3.8 An optical image of a broken tapered fiber following to a failed tapering process. 38
3.9 An optical image of a non-adiabatic tapered optical fiber. 39

3.10 Drawing of the tapering system with hydrogen torch. 40
3.11 Transmission spectrum recorded during the fiber tapering process. 41
3.12 SEM images of a successfully tapered fiber. Three consecutive images were from the thickest to thinnest waist diameter. 42
3.13 Light coupling to a toroidal resonator from a tapered silica fiber. The fiber is moved to close proximity to the toroidal resonator while monitoring the transmission. The drop in the transmission indicates a successful light coupling. 43

4.1 Reflowing setup with fixed carbondioxide laser 45
4.2 (a) Array of microdisks produced on a chip by standard microfabrication techniques. (b) The array of microdisks is reflowed to produce high Q-factor microtoroids. 47
4.3 The effect of the distance on power density for reflowing and the observation of the CO_2 laser beam shape. (a) The thickness of the lines engraved onto the plexiglass substrate is considered the beam radius. The dashed line indicates the distance selected for the reflowing process. (b) Power density decreases with the inverse of the square of the spot radius. 49
4.4 Scanning electron microscope images of (a) A single toroid in the array and (b) array of toroids on a chip. 50
4.5 (a) Resonant mods recorded from a toroidal microresonator fabricated using raster scan diode laser. (b) One mod from the spectrum was chosen and detalied scan was conducted. 51
4.6 Resonant mod recorded from another toroidal microresonator fabricated using diode laser. 52
4.7 Resonant mod recorded from a toroidal microresonator fabricated using raster scan laser. Real data are shown with dots, and the line is a Lorentzian fit. Full width half maxima (FWHM) is measured as 0.5 pm and the Q-factor is 3 x 10^6. 53
4.8 Scanning electron microscope images of (a) A single racetrack resonator in the array and (b) an array of racetrack resonators on a chip. 54

4.9 Scanning electron microscope images of (a) A single ellipsoid resonator in the array and (b) an array of ellipsoid resonators on a chip. 55

5.1 Silica microtoroid fabrication procedure from wafer to a toroidal resonator. (a) 20x30mm rectangular substrates diced from the wafer. (b) HMDS coating (yellow color) onto the substrate to enhance the bonding between the oxide layer (blue color) and photoresist. (c) Photoresist coating (red color) onto the substrate. (d) A designed mask with patterns on it is used to pattern the substrate by using photolithography. (e) The photoresist developing process is done in order to harden the photoresist to allow patterns on the substrate. (f) By using buffer oxide etchant (BOE 7:1), silica etching is done. The area under photoresist patterns is protected while the rest is etched. (g) Silicon etching is done after silica etching. The area under the silica undergoes isotropic etching to form a pillar while the rest is etched completely. (h) The photoresist is removed from the structure since there is no need for it anymore. (i) Silica microdisks on silicon pillars produced as a result of microfabrication are reflowed by using a CO_2 laser engraver. 62
5.2 (a) Tilted view and (b) side view of a fabricated silica disk resonator taken by SEM. (c) Tilted view and (d) side view of a fabricated silica toroidal resonator. 63
5.3 GST chalcogenide layer coated onto the microtoroid arrays on the substrate, creating a layer on the silica microtoroids. 64
5.4 Optical images of a microtoroid coupled to a tapered silica fiber. (a) Side view of the resonator. (b) Top view of the resonator. . . . 65
5.5 (a) Resonant mode of a bare silica microtoroid within the first batch prior to GST coating. (b) Resonant mode of a 5 nm coated resonator. (c) Resonant mode of a bare silica microtoroid within the second batch prior to GST coating. (d) Resonant mode of a 10 nm coated resonator. 66

5.6 Permanent tuning of a resonant mode of 5 nm GST-coated Silica microtoroid. The transmission spectrum of the mode (a) prior to laser illumination, (b) during the laser illumination, and (c) after the laser illumination. 67
5.7 Permanent tuning of a resonant mode of 10 nm GST-coated Silica microtoroid. The transmission spectrum of the mode (a) prior to laser illumination, (b) during the laser illumination, and (c) after the laser illumination. 69

Chapter 1

Introduction

1.1 Light and the Emergence of the Optical Resonators

Light, the fastest-known entity in the universe, has always been an exciting topic for curious minds. The origin of light, the color of things, how it travels, and how fast it travels have been asked numerous times in the minds of early and contemporary scientists and researchers to reach a better understanding of light and our environment in the broader perspective of things. The light was crucial for scientific progress right from the beginning because the act of "observation" played a vital role in the early stage of experimentation since humankind relied on their "built-in optical sensors;" eyes that detect visual input from direct or indirect sources of light from the environment.

As humankind advanced in science and technology, better tools were being developed to be used in manufacturing and experiments. When electricity was used to power up the light bulbs, it was an outstanding achievement after the "invention" of the fire. After all, humankind did not have to rely on natural light sources such as the sun and fire. With expanding knowledge of humankind, observation techniques were diversified and complicated for gathering precise and accurate

data. Complicated tools for light measurement and sophisticated artificial light sources were developed. The invention of the LASER (light amplification by stimulated emission of radiation) greatly expanded scientific progress.

The importance of the LASER is its attribute of emitting an intense, collimated and coherent light beam, and that led to many scientific and technological advancements. This attribute relies on a "laser cavity" in which light gains coherence through a series of reflections between parallel mirrors with high reflectance. A laser cavity is essentially an "optical resonator" that traps light in its boundaries for specific states that satisfy constructive interference conditions and sustains an optical resonance within that boundaries. A similar phenomenon was introduced to scientific knowledge in the late 19th century. Lord Rayleigh noticed the traveling of sound waves through the boundary of a cathedral dome, and he published his findings of "whispering gallery waves," which is the traveling of a whisper sound due to the series of reflections of sound waves from the boundaries of the cathedral dome [1]. The dual nature of light [2] includes wave nature as well as particle nature; therefore, similar to acoustic (sound) waves, electromagnetic waves also show a similar effect with optical resonators (optical analogous of the cathedral dome in the sound wave example).

Light can be coupled into optical resonators at specific wavelengths that satisfy the constructive interference conditions [3, 4]. After coupling is achieved, the light begins to resonate within the boundary of the optical resonator, depending on its morphology. This resonance builds up the light intensity within the resonator that can be utilized for various applications involving detection and sensing [5, 6, 7, 8, 9, 10, 11], light switching and modulation [12, 13, 14, 15], light generation [6, 16, 17, 18], and nonlinear photonics [17, 19, 20, 21]. Due to their wide range of applications and utilization, extensive research is being done on optical resonators, including fabrication methods as well as their possible applications. This thesis consists of research on the fabrication process and applications of toroidal optical resonators in order to provide methods for improving the fabrication process of the resonators and achieving a standardization procedure. Studies presented in this thesis involve the fabrication of silica ring resonators on silica on a silicon wafer and forming toroidal silica resonators by

reflowing, tapering the optical fiber to achieve light coupling into the resonators, and experiments on chalcogenide coated toroidal resonators.

1.2 Thesis Outline

The contents of this thesis are organized in order of theory and then experiments in chronological sequence. Contents of individual chapters are explained, and any collaboration with colleagues is stated as follows:

Chapter 2 is an introductory chapter giving theory about optical microresonators, different types of microresonators, the fabrication process of toroidal resonators as well as the materials used for the process. Development and optimization of the fabrication process were done in collaboration with Erol Özgür.

Chapter 3 covers the explanation of optical coupling and different types of coupling. The tapering of silica optical fiber is also detailed in this chapter. The setup used for fiber tapering was developed and optimized in cooperation with Erol Özgür and Ozan Aktaş.

Chapter 4 gives a new technique for the mass production of optical resonators with different geometries. Reflowing of resonators with raster scan laser was done in collaboration with Erol Özgür.

Chapter 5 explains a new method developed involving chalcogenide layer coating for the post-production tuning mode resonances of optical resonators. Coating the resonators with chalcogenide was done in collaboration with Gökhan Bakan.

Chapter 6 summarizes what has been done in experiments detailed in previous chapters and proposes several pointers for possible studies that can be done in the future.

Chapter 2

Optical Microresonators

2.1 Introduction

Optical resonators are physical structures used to trap light under specific conditions to utilize it for numerous tasks for scientific and technological applications [4]. Light, which inherits both wave and particle properties (dual nature of the light), is the fastest traveling entity known in the universe, depending on humankind's current level of cumulative knowledge. Imagining light trapped into a microscale structure – even a nanoscale for some applications – may sound unlikely, but that is a phenomenon researchers have been working on for some time. If the light is coupled into an optical resonator that can be achieved by a variety of means, which will be discussed in the later chapters, it begins to propagate within the resonator structure, generally following the boundaries of the structure with a series of internal reflections (total internal reflection, TIR) while manifesting whispering gallery modes [3, 4]. Lord Rayleigh first introduced the whispering gallery following his observations regarding sound waves traveling through the dome of St Paul's Cathedral [1]. The same principle can be applied to electromagnetic waves, which also applies to light. While light is propagating along the geometrical path it is confined into, it beings to interfere with more electromagnetic waves due to the continuous coupling into the resonator, and

whispering gallery modes (WGMs) occur for the conditions that satisfy constructive interference. The following equation represents the constructive interference condition;

$$OpticalPathLength = n \cdot \lambda_n \tag{2.1}$$

where n is the resonant mode number, and λ_n is the wavelength of the corresponding mode number. Optical path length (OPL) depends on the morphology (geometry) and the dielectric properties (refractive indices) of both the resonator material and the environment in which the resonator resides. Due to the dependency on morphology, whispering gallery mode resonators (WGMRs) can also be referred to as morphology-dependent resonators (MDRs). Each λ_n represents a WGM (or morphology-dependent resonance). Optical WGMs, which are optical analogous to acoustic resonant modes from Lord Rayleigh's observations, are also similar to electrical oscillations at a specific resonant frequency of an inductor-capacitor (LC) circuit. The combination of low material absorption and low losses contributes to optical microresonators' potential functionality for a variety of applications [5, 6, 7, 8, 9, 10, 11, 12, 13, 14, 15, 16, 17, 18, 19, 20, 21].

2.2 Resonator Types

There are several types of optical resonators depending on their geometries; Fabry-Perot [22, 23], disk [24, 25, 26, 27, 28], ring [26, 29, 30, 31], spherical [12, 16, 32], toroidal [33, 34, 35], and photonic crystal resonators [36, 37, 38] are the common types. Fabry-Perot type resonator is a structure that has two parallel mirrors (or parallel plates that are coated with highly reflective material) facing their reflective surfaces to each other with a separation between (Figure 2.1).

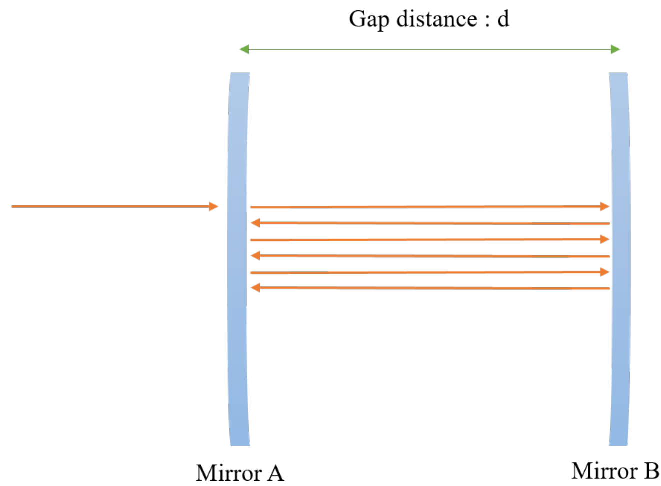

Figure 2.1: Schematic representation of a Fabry-Perot (two-mirror planar) resonator.

When a light incident to one plate, the portion of the light is transmitted into the structures, the cavity, and travels to the other end where it hits the second mirror's highly reflective surface. The series of reflections between two parallel surfaces create an environment with waves interfering with each other either constructively or destructively. If constructive interference condition stated in Eq. 2.1 is met, the constructive interference occurs between the transmitted wave and the reflected wave, and a resonant mode with a specific frequency (wavelength) appears. This type of cavity is widely used in LASERs to enhance the light intensity and provide an emission with a specific wavelength.

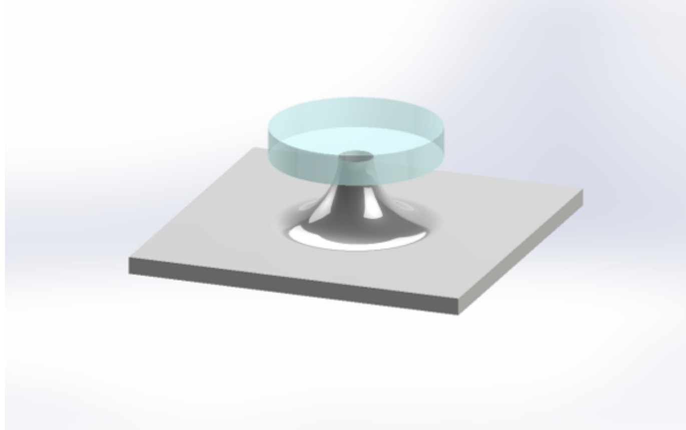

Figure 2.2: Drawing of a disk resonator on a pillar.

There are also disk-type resonators consisting of a disk-shaped block material as a resonator structure (Figure 2.2). The light that is coupled into the microdisk resonator propagates along the circumference of the disk. Ring resonators are like disk resonators, but as the name implies, they do not have the material at the center of the block, hence limiting the light into a more confined volume determined by the inner and outer radius (ring thickness) of the ring resonator (Figure 2.3). Microring and microdisk resonators have lower quality factors (Q-factors, described in Section 2.3.3) than microsphere resonators, primarily because of the lack of surface smoothness, unlike spherical resonators, which are often fabricated by utilizing surface tension methods.

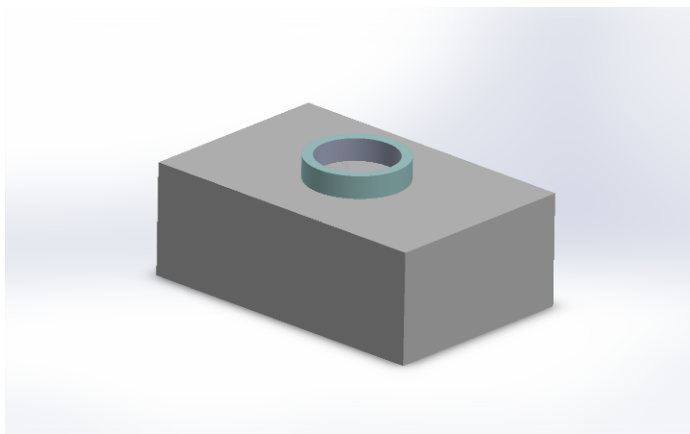

Figure 2.3: Drawing of a ring resonator on a substrate.

Another well-known resonator type is a spherical resonator. The light is coupled into the spherical resonators (microspheres), often by waveguides or optical fibers (coupling methods will be introduced in the forthcoming chapters). Although it is not an easy task to achieve, it is possible to couple light into resonators via the free-space coupling. When light is coupled into the microresonator, it begins to propagate through its circumference by a series of internal reflections due to the TIR from the material-environment interface, and depending on the absorption coefficient of the material, it can sustain thousands of cycles (which means one full length of the circle's perimeter) before the electromagnetic wave diminishes. If the electromagnetic waves constructively interfere at certain conditions (as stated in Eq. 2.1), resonant modes occur in those specific wavelengths. Microsphere resonators are known for their high-Q-factor values, which means high temporal confinement of light within the structure.

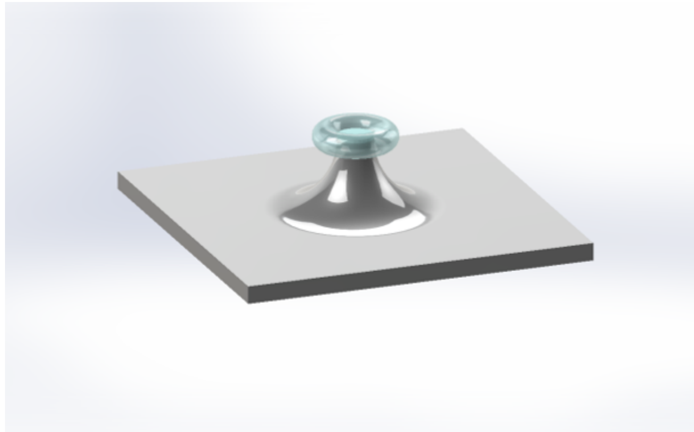

Figure 2.4: Drawing of a toroidal resonator on a pillar.

A toroidal microresonator (microtoroid) is another type of resonator which is fabricated by using a reflowing technique on a microdisk resonator (Figure 2.4). Reflowing is a technique in which the ring resonator is heated up until the material's softening temperature until the surface tension results in the reshaping of the microring into the microtoroid. They have higher Q-factors than the ring and disk-shaped microresonators and comparable values to microsphere resonators. They also have low mode volume values (which will be described in the next section) that imply high spatial confinement of the light within the boundaries of the resonator.

2.3 Resonator Theory

The work for understanding the WGMR theory was pioneered by Mie [39] and Debye [40]. Mie investigated the scattering of electromagnetic waves on spheres, and Debye studied dielectric and metallic spherical resonators. Later, Richtmyer [41] and Gastine [42] discussed the electromagnetic oscillations in dielectric media in their respective studies on the subject. Prior to continuing the explanation of various concepts, equations, and figures of merits related to the subject; microresonators, it should be noted that even though spherical and toroidal resonators have distinct morphologies, the path of the light in these resonators are similar (given that the light coupling mechanism is evanescent coupling).

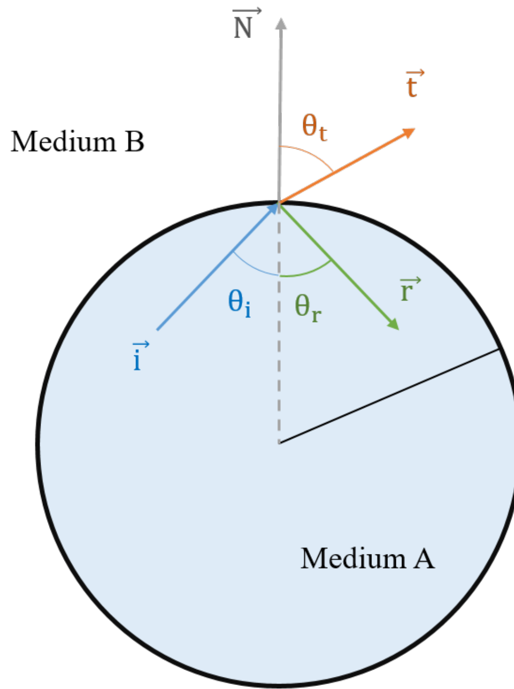

Figure 2.5: Light rays in a circular resonator.

Ray modeling can be considered while investigating WGMs in a circular path resonator (disk, ring, spherical or toroidal) in order to explain how light can be confined in a resonator (Figure 2.5). The light rays travel through the resonator's circular perimeter due to total internal reflection (TIR), resulting from the refractive index differences between the resonator materials and the surrounding

medium. The condition for the TIR can be derived from Snell's Law, which is;

$$n_A \cdot \sin\theta_i = n_B \cdot \sin\theta_t \tag{2.2}$$

where n is the refractive index of respective media, A, and B, whereas θ_i is the incident angle and θ_t is the angle of the refracted (transmitted) light. For TIR, the refractive index of medium A is required to be higher than medium B.

TIR means the light that incidents to the interface does not transmit any energy to the consecutive medium, and the energy is reflected into the medium that the light originated. This indicates that the light is not refracted (or transmitted) but reflected into the medium. The angle of reflectance, of course, is equal to the angle of incidence from a direct result of being in the same medium in accordance with Snell's law. TIR begins at some critical angle of incidence, depending on the refractive indices of both media, which in return, the angle of the refracted ray is 90° [43]. The light will be reflected in any incident angle equal to or bigger than this critical angle.

Suppose this TIR is sustained within the medium consecutively, which should be the case because the angle of reflection is equal to the angle of incident. In that case, the light begins to travel within a confined space, a circular path in our case by TIR (Figure 2.6).

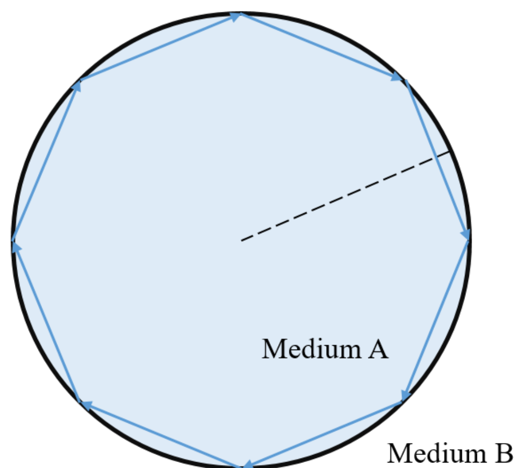

Figure 2.6: Ray path in circular geometry due to TIR.

TIR and the circulation of light can be explained by using ray optics equations. When an incident ray coincides with the interface, two separate equations can be derived for the reflection and for the refraction (transmission).

The vector formulation of Snell's law can be written as follows;

$$n_A\left(\overrightarrow{i} \times \overrightarrow{N}\right) = n_B\left(\overrightarrow{t} \times \overrightarrow{N}\right) \tag{2.3}$$

The equation can be rewritten as;

$$n_A\left(\overrightarrow{i} \times \overrightarrow{N}\right) - n_B\left(\overrightarrow{t} \times \overrightarrow{N}\right) = 0 \tag{2.4}$$

Hence,

$$\left(n_A\overrightarrow{i} - n_B\overrightarrow{t}\right) \times \overrightarrow{N} = 0 \tag{2.5}$$

This implies that the first part of the cross product should be parallel to the second part $\overrightarrow{N}$ since the cross-product of two vectors is zero if they are parallel to each other. Therefore, by using constant a , we can assume;

$$\left(n_A\overrightarrow{i} - n_B\overrightarrow{t}\right) = a\overrightarrow{N} \tag{2.6}$$

And by using equation 2.6, the refracted ray can be written as;

$$\overrightarrow{t} = \frac{1}{n_B}\left(n_A\overrightarrow{i} - a\overrightarrow{N}\right) \tag{2.7}$$

By taking the dot product of both sides of the equation with $\overrightarrow{N}$, the equation can be derived to;

$$\left(n_A\overrightarrow{i} - n_B\overrightarrow{t}\right) \cdot \overrightarrow{N} = a\overrightarrow{N} \cdot \overrightarrow{N} \tag{2.8}$$

So, the fact that the dot product of two parallel (or identical) vectors is 1, the equation can be simplified as follows;

$$a = \left(n_A\overrightarrow{i} - n_B\overrightarrow{t}\right) \cdot \overrightarrow{N} \tag{2.9}$$

Following equations can be written by distributing the vector $\overrightarrow{N}$ to the component in brackets and using the dot product of vectors;

$$a = n_A\overrightarrow{i} \cdot \overrightarrow{N} - n_B\overrightarrow{t} \cdot \overrightarrow{N} \tag{2.10}$$

$$a = n_A \ \cos\theta_i - n_B \ \cos\theta_t \tag{2.11}$$

It is possible to define constant a by using only incident angle and refractive indices of the medium and the resonator. By using Snell's law;

$$n_A^2 \cdot \Big(\cos\left(2\theta_i\right) - \cos^2\theta_i = n_B^2 \cdot \Big(\cos\left(2\theta_t\right) - \cos^2\theta_t\Big) \tag{2.12}$$

From the previous equation, the cosine of the refracted ray's angle can be derived as;

$$\cos^2\theta_t = -\frac{n_A^2\cos(2\theta_i)}{n_B^2} + \frac{n_A^2\cos^2\theta_i}{n_B^2} + \cos(2\theta_t) \tag{2.13}$$

Assuming $cos2\theta \approx 1$ for angles close to 90°;

$$\cos\theta_t = \sqrt{\frac{n_A^2\cos^2\theta_i}{n_B^2} - \frac{n_A^2}{n_B^2} + 1} \tag{2.14}$$

By using equation 2.14 to rewrite equation 2.11, constant a can be derived as;

$$a = n_A\cos\theta_i - n_A\sqrt{\cos^2\theta_i - 1 + \frac{n_B^2}{n_A^2}} \tag{2.15}$$

In a similar manner, a formulation for the reflection can be written in vectorial form.

$$n_A(\overrightarrow{i} \times \overrightarrow{N}) = n_B(\overrightarrow{r} \times \overrightarrow{N}) \tag{2.16}$$

Of course, in the case of reflection, the refractive indices on both sides of equation 1.16 are the same, as well as the incident and the reflection angles. Hence;

$$(\overrightarrow{i} - \overrightarrow{r}) \times \overrightarrow{N} = 0 \tag{2.17}$$

Therefore we can write;

$$(\overrightarrow{i} - \overrightarrow{r}) = b\overrightarrow{N} \tag{2.18}$$

where b is a constant and can be derived from the previous equation by taking the dot product of both sides;

$$b = \overrightarrow{N}\cdot\overrightarrow{i} - \overrightarrow{N}\cdot\overrightarrow{r} \tag{2.19}$$

$$b = 2\cos\theta_A \tag{2.20}$$

It is possible to use the above equations in order to determine the light ray's path, whether it is internally reflected or refracted out from the resonator.

2.3.1 Electromagnetic Theory of Whispering Gallery Modes

Due to the similar optical paths that are traveled by coupled light, it is possible to compare the toroidal WGM resonator to the spherical resonator. Wave solutions in a dielectric resonator can be found for spherical resonators. It is possible to derive vector solution of Maxwell's equations for a dielectric sphere by using Debye Potentials; U, V [44].

Maxwell's equations for an isotropic dielectric sphere can be written as follows;

$$\nabla \times \overrightarrow{E} = ik\overrightarrow{H} \tag{2.21}$$

$$\nabla \times \overrightarrow{H} = -ik\overrightarrow{E} \tag{2.22}$$

where wavenumber $k = k_0\sqrt{\varepsilon\mu}$. ε is the dielectric constant while μ is the magnetic permeability of the sphere, where $k_0 = \omega/c$. The solution of Maxwell's equations in a spherical coordinate system for transverse electric (TE) modes;

$$E_r = \left(\frac{\partial^2}{\partial r^2} + k^2\right)U \quad , \quad H_r = 0 \tag{2.23}$$

$$E_\vartheta = \frac{1}{r}\frac{\partial^2}{\partial r}\frac{U}{\partial\vartheta} \quad , \quad H_\vartheta = -ik\frac{1}{r}\frac{\partial U}{\partial\varphi} \tag{2.24}$$

$$E_\varphi = \frac{1}{r\sin\vartheta}\frac{\partial^2}{\partial r}\frac{U}{\partial\varphi} \quad , \quad H_\varphi = ik\frac{1}{r}\frac{\partial U}{\partial\vartheta} \tag{2.25}$$

and for transverse magnetic (TM) modes;

$$H_r = \left(\frac{\partial^2}{\partial r^2} + k^2\right)V \quad , \quad E_r = 0 \tag{2.26}$$

$$H_\vartheta = \frac{1}{r}\frac{\partial^2}{\partial r}\frac{V}{\partial\vartheta} \quad , \quad E_\vartheta = ik\frac{1}{r}\frac{\partial V}{\partial\varphi} \tag{2.27}$$

$$H_\varphi = \frac{1}{r\sin\vartheta}\frac{\partial^2}{\partial r}\frac{V}{\partial\varphi} \quad , \quad E_\varphi = -ik\frac{1}{r}\frac{\partial V}{\partial\vartheta} \tag{2.28}$$

The Debye potentials, U and V that are used in Equations 2.23 - 2.28 must satisfy the following scalar equation;

$$\frac{\partial^2 U}{\partial^2 r} + \frac{1}{r^2\sin\vartheta}\frac{\partial}{\partial\vartheta}\left(\sin\vartheta\frac{\partial U}{\partial\vartheta}\right) + \frac{1}{r^2\sin^2\vartheta}\frac{\partial^2 U}{\partial\varphi^2} + k^2 U = 0 \tag{2.29}$$

In Equation 2.29, $k = k_0\sqrt{\varepsilon\mu}$ inside the sphere and $k = k_0$ outside.

It is possible to represent the potential in a spherical coordinate system by;

$$U = R(r)\theta(\vartheta)\phi(\varphi) \tag{2.30}$$

By using Equations 2.29 and 2.30, we can obtain the following equations for the functions $R(r)$, $\theta(\vartheta)$, $\phi(\varphi)$.

$$\frac{d^2R}{dr^2} + \Big(k^2 - \frac{l(l+1)}{r^2}\Big)R = 0 \tag{2.31}$$

$$\frac{1}{\sin\vartheta}\frac{d}{d\vartheta} + \Big(\sin\vartheta\frac{d\theta}{d\vartheta}\Big) + \Big(l(l+1) - \frac{m^2}{\sin^2\vartheta}\Big)\theta = 0 \tag{2.32}$$

$$\frac{d^2\phi}{d\varphi^2} + m^2\phi = 0 \tag{2.33}$$

where l, and m are angular and azimuthal mode numbers, respectively, while $-l \leq m \leq l$.

Equation 2.31 can be rewritten as a Bessel equation by using $R(r) = \sqrt{kr}Z(kr)$;

$$\frac{d^Z}{dz^2} + \frac{1}{z}\frac{dZ}{dz} + \Big(1 - \frac{v^2}{z^2}\Big)Z = 0 \tag{2.34}$$

in which $z = kr$ and $v = l + 1/2$.

Since a wave traveling from infinity cannot exist, the solution outside the sphere must have the asymptotic form; therefore, the solution must be in the form of Hankel functions of the first kind. The solution for Equations 2.23 - 2.25 inside the dielectric sphere with a radius of a where $r \leq a$ is;

$$U^i_{lm}(r,\vartheta,\varphi) = C_iP^m_l(\cos\vartheta)\sqrt{kr}J_v(kr)e^{\pm im\varphi} \tag{2.35}$$

while the solution outside the sphere where $r > a$ is,

$$U^e_{lm}(r,\vartheta,\varphi) = C_eP^m_l(\cos\vartheta)\sqrt{kr}H^{(1)}_v(k_0r)e^{\pm im\varphi} \tag{2.36}$$

where C_i and C_e are arbitrary constants, J_v and $H^{(1)}_v$ are Bessel function and Hankel function of the first kind, respectively and P^m_l is Legendre polynomial [44].

2.3.2 Free Spectral Range

Free spectral range (abbreviated as FSR) is the separation between two consecutive resonant modes manifested. Depending on the choice, it can be defined in terms of frequency or wavelength.

The FSR of a circular (spherical, disk, ring, toroidal) resonator can be obtained from the following equation;

$$\Delta f_{FSR} = \frac{c}{2\pi na} \tag{2.37}$$

where c is the speed of light in the vacuum, n is the resonator's refractive index, and a is the radius of the resonator. Noting that Equation 2.37 gives the free spectral range of a resonator in terms of frequency, it is also possible to calculate the value in terms of wavelength by using the following formula;

$$\Delta\lambda_{FSR} = \frac{\lambda^2}{2\pi na} \tag{2.38}$$

where λ is the wavelength.

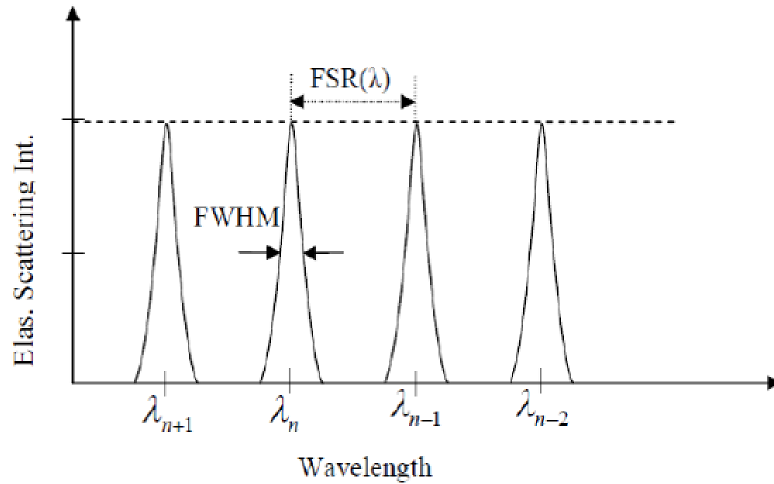

Figure 2.7: Resonant modes represented by each peak and free spectral range between consecutive modes.

In Figure 2.7, elastic scattering spectrum from a couple resonator with respect to wavelength was illustrated. In the figure the peaks shown are the actual resonant modes coupled into the resonator. When the light with specific wavelength

is coupled into the resonator, the transmission through the waveguide decreases, ideally, down to zero, whereas the scattering from resonator increases on those wavelengths since it means light is coupled into the resonator successfully.

2.3.3 Quality Factor (Q-Factor) and Mode Volume

The temporal confinement of light is essential for optical resonators since it is an indication of the energy storage capability of the resonator, which is essential for several applications such as lasing and sensing. The extent of the light energy stored within the resonator affects the light-matter interaction, whether it is with the resonator or surrounding material. Since the light-matter interaction is essential for the applications, resonators with better temporal confinement abilities are preferred over resonators with inferior confinement abilities.

The temporal confinement of light is tied to the loss mechanisms of the resonator, including material absorption, scattering loss, surface (absorption) loss, and radiation loss. Of course, loss due to the coupling to an external waveguide (i.e., optical fiber) –which is required for applications– contributes to the total loss mechanism.

Due to this loss mechanism, a photon inside the resonator has a lifetime, and the Q-factor describes the lifetime of the photon inside the resonator for a specific mode. The stored energy function is described as follows;

$$U(t) = U(0)e^{-t/\tau} \tag{2.39}$$

Equation 2.39 can be rewritten as;

$$U(t) = U(0)e^{-\frac{\omega_0 t}{Q}} \tag{2.40}$$

The Q-factor of the resonator is defined by the ratio of stored energy inside the cavity to the energy loss per cycle;

$$Q = 2\pi \frac{StoredEnergy}{EnergyLossperCycle} \tag{2.41}$$

From the previous equations, the quality factor, Q, can be deduced;

$$Q = \frac{\omega_0 U}{-\frac{dU}{dt}} \tag{2.42}$$

As well as temporal confinement, spatial confinement of the light is also crucial for optical resonators since it enhances the light-matter interaction, which is required for applications. The spatial confinement of the light is defined as mode volume. The more confined the light, the better for light-matter interaction since it means light is forced to travel through a route confined in much less volume. That is why toroidal resonators are ideal resonator types for photonics due to their very high Q-factors and very low mode volumes.

2.4 Microtoroid Fabrication

The wafers used in this study were acquired from private companies (Addison and University Wafers). 4-inch silicon wafers with different thicknesses of thermal oxide (1.0 µm, 1.8 µm, 2.0 µm, and 3.0 µm) layers grown on top were used. The fabrication of the toroidal microresonators begins with dicing of the whole wafer into 20 x 20 mm (or 20 x 30 mm) rectangular-shaped substrates. All of these substrates will be treated separately in order to fabricate a batch of microresonator sets. The fabrication process relies on the silicon microfabrication process, which was matured over years of silicon chip production. Before the microfabrication process, each substrate should be cleaned in order to remove any contaminants. In order to achieve the cleaning, the substrate was first cleaned with acetone for 120 seconds. After acetone cleaning, it was immersed into isopropanol alcohol (IPA) and left there for 120 seconds as well. Then the substrate was taken from the IPA solution and immersed in deionized water (DI-water) for 60 seconds. Then the substrate was rinsed with DI water using a nozzle and blow-dried using a nitrogen gun. Following blow-drying, the substrate was placed into a heater at 120°C for 120 seconds in order to evaporate any remnant water particles.

Following the cleaning, the substrate should be coated with the photoresist chemicals in order to pattern the surface of the wafer by lithography. Initially, hexamethyldisilazane (HMDS) was used to cover the surface of the silica layer by using a spin-coater. The reason for coating the layer with the HMDS is to enhance the bonding of photoresists onto the surface of the silica layer since better bonding of photoresists with the silica layer improves the photolithography process. A spin coater (Laurell) was used to spin coat the HMDS onto the silica layer with defined RPM (revolution per minute) and acceleration settings. During the optimization of the process, several RPM and acceleration values were tried to improve the process. Initial trials began with 5000 RPM and 2500 acceleration values, and later it was decreased to 3000 and 1500, respectively. Following the spin coating of the HMDS, the substrate needs to undergo a baking process in an electric heater for 300 seconds at 120°C to remove the solvents within the HMDS and make it a temporary solid layer on the substrate.

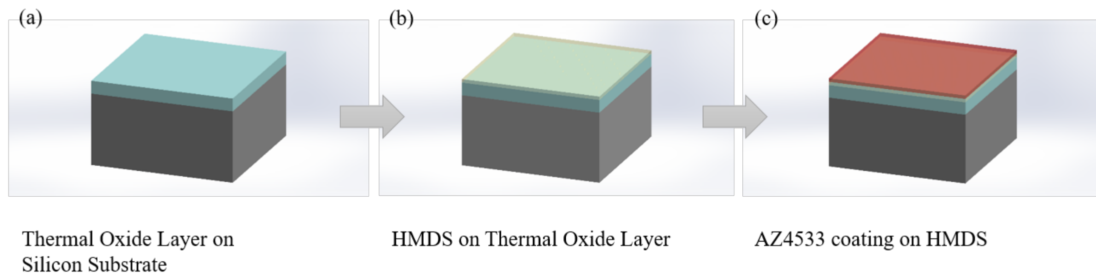

Figure 2.8: Spin Coating of a silicon substrate (gray color) with a thermal oxide layer (blue color) on top. (a) Diced substrate, (b) HMDS (yellow color) spin-coated substrate, (c) Photoresist (red color) coated substrate.

The HMDS-coated substrate was then spin-coated with an AZ4533 type photoresist. AZ4533 is a positive photoresist, which means that light exposure will soften photoresist bonds, making it easier to remove the parts exposed to the light. The same settings for the spin-coating device were used to coat the photoresist on top of the HMDS on the silica layer. The values were 3000 RPM and 1500 acceleration for 50 seconds. Following the spinning process, the resist was baked at 110oC for 50 seconds in the electric heater, similar to the HMDS coating process. As a result of this procedure, a 3.3 µm thick photoresist was coated onto the substrate (Figure 2.8).

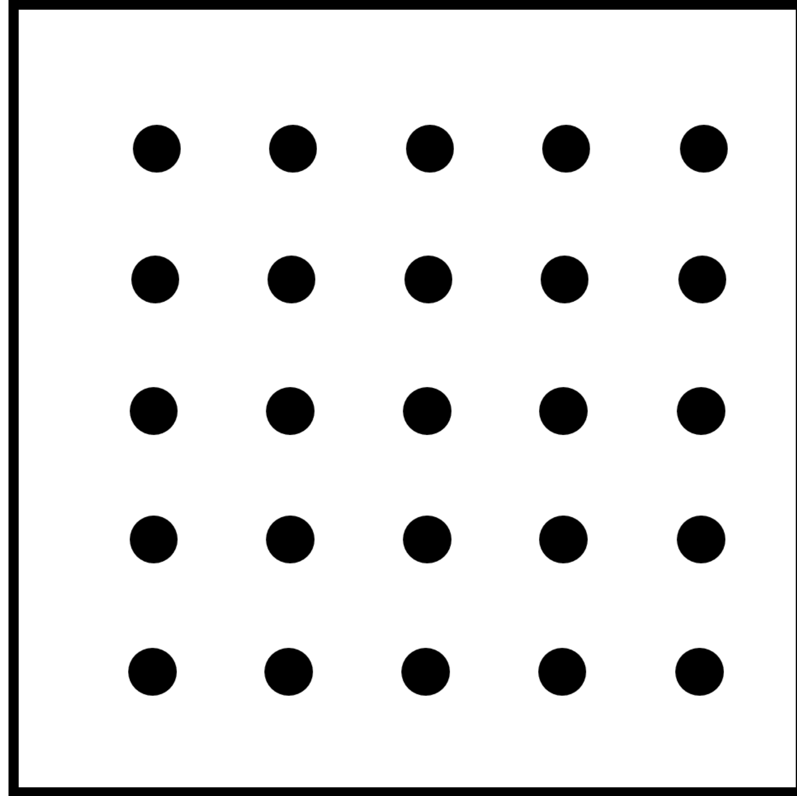

Figure 2.9: Graphical representation of one of the masks used. Black circles are the chromium layer on the mask, while the rest of the mask is transparent to allow ultraviolet light to pass through.

Following the cleaning and the photoresist coating, substrates were patterned by photolithography. In order to pattern the photoresist on the substrate, a mask (Figure 2.9) was designed with circular patterns on it using L-Edit software. Then the design was printed on a blank mask substrate by using a mask writer (Heidelberg Instruments). Later, this mask was used to pattern the substrate with Mask Aligner (EVG620).

The lithography was initiated by exposing an ultraviolet (UV) light onto the photoresist-coated substrate through the designed mask. The exposure was done with 200 µm proximity and 70 mJ/cm^2 dose intensity (Figure 2.10a). Following the lithography, the photoresist bonding is weakened in the areas exposed to UV light. In order to form the disk patterns on the surface, the sample with a photoresist was immersed into a developer solution. A developer solution is a

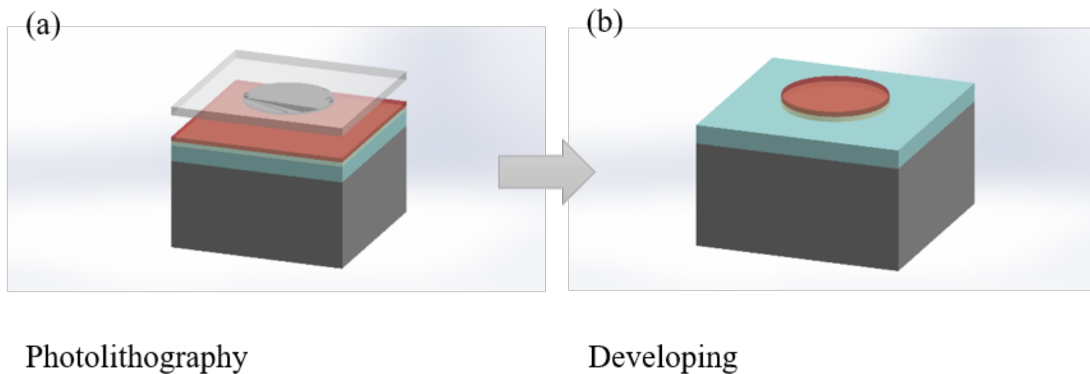

Figure 2.10: (a) UV Photolithography was done on the substrate, followed by (b) the developing process.

mixture of an AZ400K solvent chemical and deionized water with a volumetric ratio of 1:4, respectively. This solvent removes the weakened photoresist and leaves the areas that were not exposed to the UV light. The sample was immersed in this solvent, and a pattern of disk-shaped photoresist areas formed on the surface. Post-baking was done to the samples as well in order to improve the circular shape of the patterns after developing (Figure 2.10b). For the post-baking, samples were heated up in an electric heater for 60 seconds at 110°C.

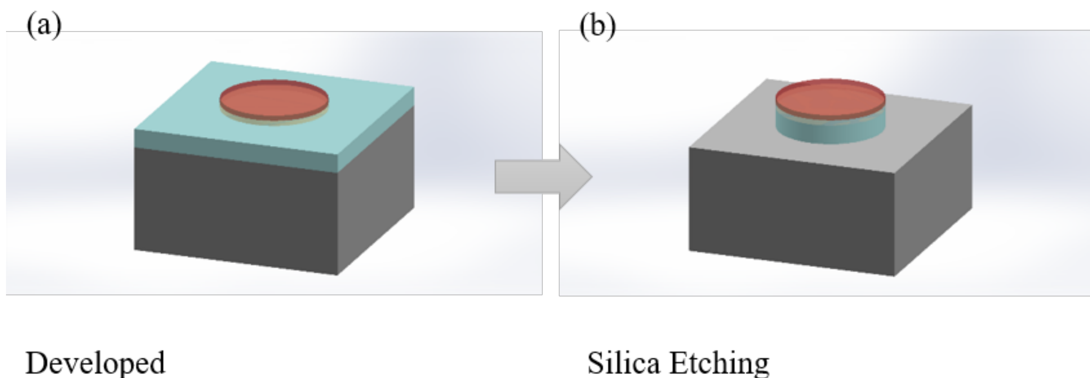

Figure 2.11: (a) Developed substrate with photoresist patterns on it, (b) Substrate after silica etching.

The sample then needs to undergo an etching process to pattern the silica layer to imprint the same pattern of the photoresist layer onto it, enabling silica disks that are required to fabricate toroidal resonators (Figure 2.11). There are two methods for etching the silica; wet etching and dry etching. Dry etching involves the usage of several gases while utilizing an inductively coupled plasma (ICP) source, while wet etching is done by a buffered oxide etchant (BOE 7:1) solution.

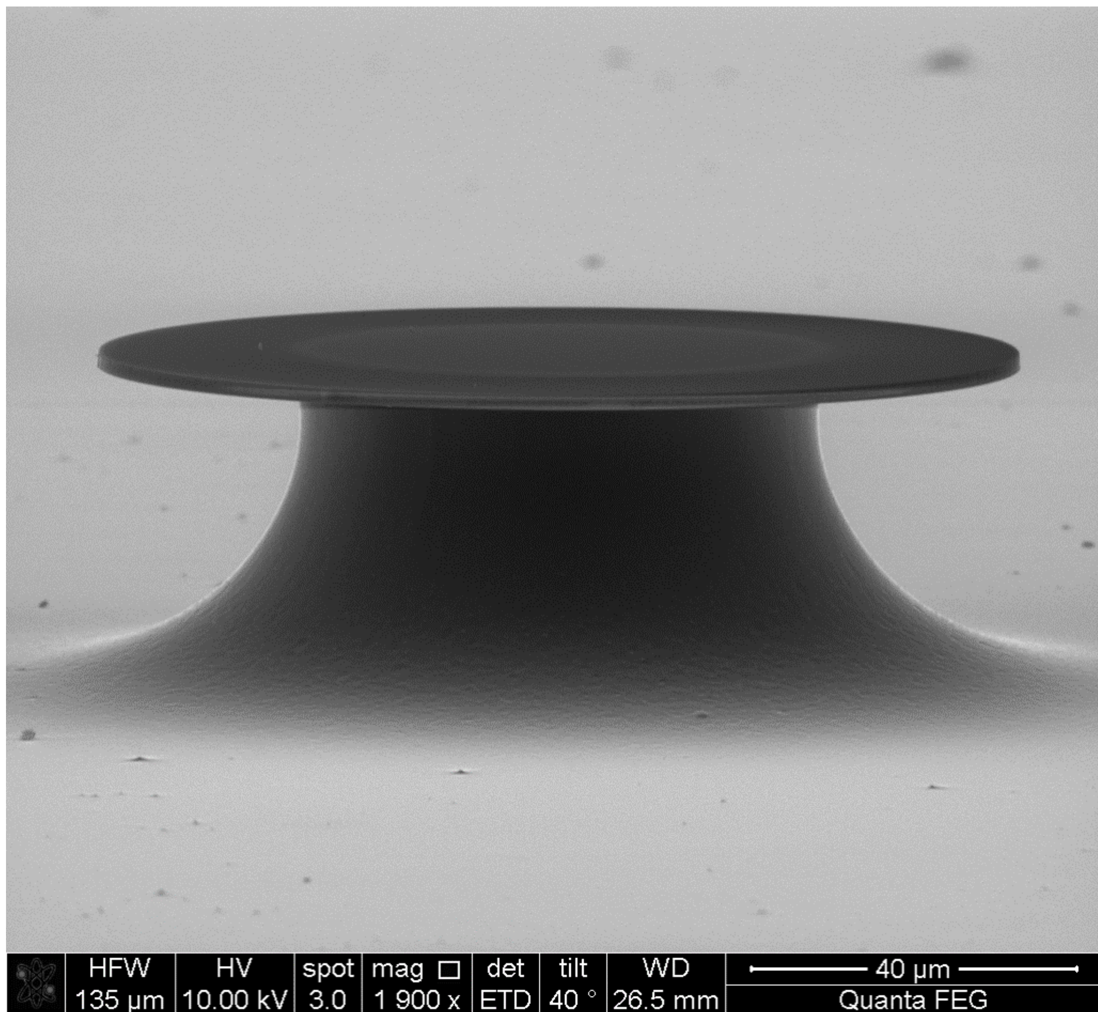

Figure 2.12: Silica microdisk on a silicon pillar after silicon etching by SF_6, following a dry etch process achieved by inductively coupled plasma technique.

In dry etching, the ICP is utilized in order to etch the silica with fluoroform (CHF_3) and oxygen (O_2) gases. The plasma formed by the ICP anisotropically etches the areas on the silica layer that are not protected by disk-shaped photoresist layers. The anisotropic etch of the silica layer results in the silica disks on top

of the silicon substrate (Figure 2.12). In this process, an ICP etch system (STS) was used with the forward coil power of 250 W and the forward (low-frequency RF) platen power of 30 W. The gas flow rates were 30 sccm (standard cubic centimeters per minute) and 100 sccm for O_2 and CHF_3 respectively.

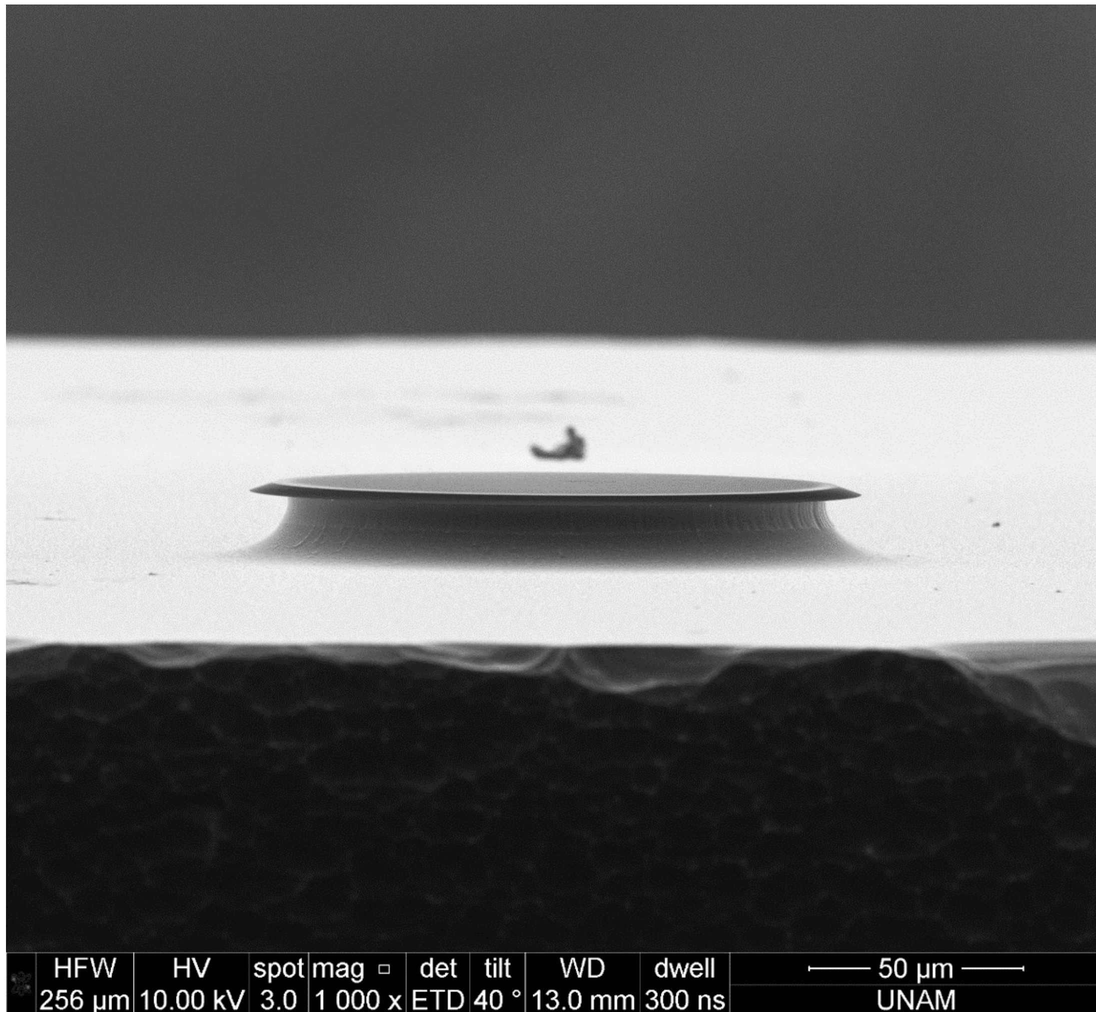

Figure 2.13: Wedged silica microdisk on a silicon pillar after silicon etching by SF_6, following a wet etch process achieved by buffered oxide etchant.

On the other hand, wet etching relies on the buffered oxide etchant, a mixture of a buffering agent and hydrofluoric acid (HF) in water. The process etches the silica isotropically; therefore, instead of perfectly disk-shaped silica layers on top, it creates a wedged disk structure (Figure 2.13). While producing microdisk resonators, ICP is preferred due to its anisotropic etch that leads to flat vertical disk walls. In order to fabricate microtoroid resonators, both methods can be

used since the final resonator structure is not a disk but a toroid that is formed by a reflowing process at the final stage. After several trials and optimizations, the wet etching method was chosen for this work. The silica was etched by the BOE with 1 nm etch per second. The 1.8 µm thick silica layer can be etched in 30 min, while the 3 µm thick silica layer needs 50 minutes. The silicon substrates with a 1.8 µm thick silica layer were etched for 30 minutes. The silica etching process transfers the photoresist pattern onto the silicon substrate leaving silica disks underneath (Figure 2.14).

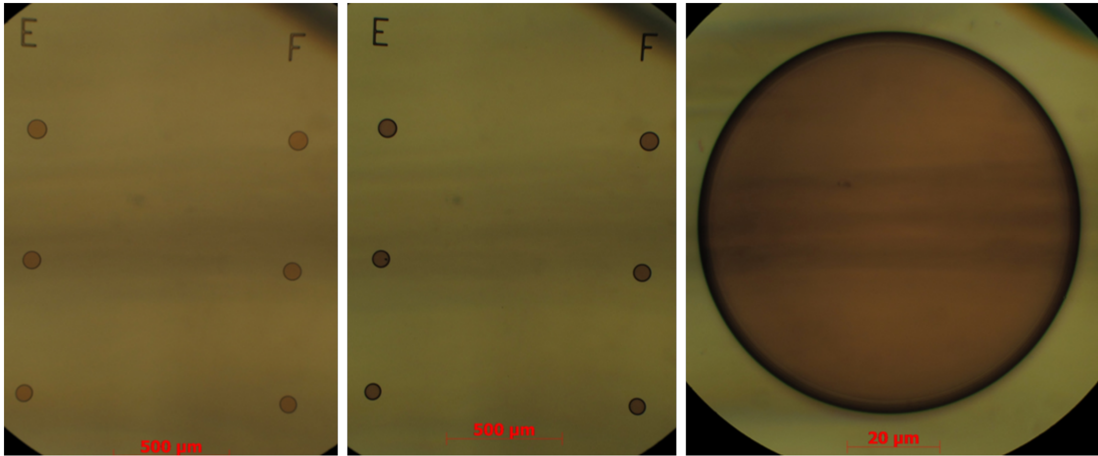

Figure 2.14: Optical microscopy images of a substrate. (a) After photolithography (5X objective). (b) After silica etching by HF (5X objective). (c) After silica etching by HF (100X objective).

Following the silica etching by the BOE, the sample needs to undergo a second etching process for silicon substrate in order to lead to the formation of silicon pillars under the silica disks (Figure 2.15). Prior to the etching, the sample was diced again in order to create smaller 2 x 20 mm (or 2 x 30 mm) substrates with sets of disks on them separately, so they can be efficiently utilized while coupling to the tapered optical fiber. There are two methods to achieve silicon etching; etching with SF_6 (ICP) and etching with XeF_2. In this work, the ICP (commercially available by STS) was used to etch the silicon with SF_6 gas with a flow rate of 130 sccm. Under the pressure of 50 mTorr, the power levels were set to 600 W and 8 W for coil forward and high-frequency platen, respectively.

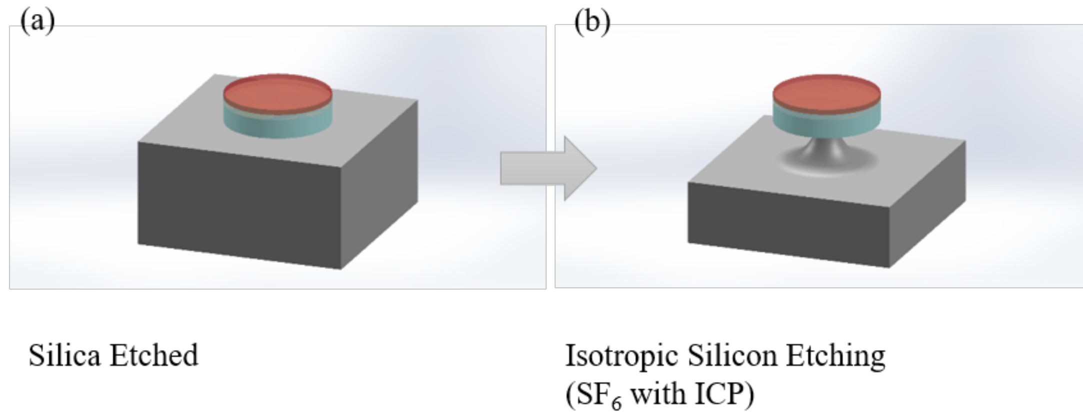

Figure 2.15: Isotropic etching of silicon layer under the silica disk. (a) Before silicon etching, (b) After silicon etching.

Finally, the samples are required to be cleaned from the photoresist and post-process remnants. For this, a mixture of oxygen and nitrogen gases with 30 sccm and 5 sccm flow rates, respectively, was used to form a plasma with 400 W RF power at a plasma cleaner (Asher) for an hour. Following the fabrication procedure in the cleanroom, slides of substrates with silica microdisks resonators on silicon pillars on top were produced. In order to achieve the final product, silica toroidal resonators, the disks should be reflowed, hence reshaped into toroids. Reflowing of the silica involves heating of the silica either under thermal or optical effect, i.e., flame or lasing. If silica is heated until it reaches its softening temperature (approx. 1700°C), it is possible to reshape the silica due to the softened material. This can be used for optical fibers in order to taper them to smaller diameters as well as to reflow silica disks into toroids. Reflowing silica is also widely used in producing spherical silica resonators from silica optical fiber tips. When a silica optical fiber tip is heated and its temperature is increased over its softening temperature, it reflows due to surface tension and forms a spherical structure.

A similar approach is also applicable for the fabrication of toroid resonators. It is known that the absorbance of the silica at the 10.6 μm wavelength range is very high, so if a laser light (with the wavelength highly absorbed by the silica) hits on a silica layer, the material absorbs the light. The energy build-up in the material

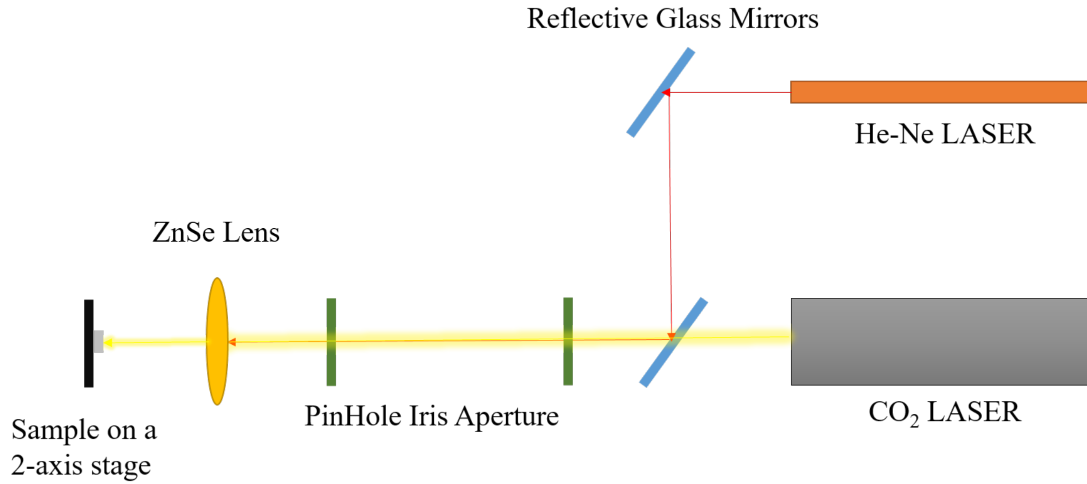

Figure 2.16: Illustration of the disk reflowing setup with carbondioxide laser.

manifests itself as the temperature increase, while the silicon pillar acts as a heat sink due to its relatively lower absorption. This temperature increase at the silica layer ends up reflowing the disk into toroid under surface tension. The resulting toroid has very low surface roughness, and due to surface roughness being one of the contributing factors to the Q-factor, the Q-factor of the toroidal resonator has a higher Q-factor than the disk resonator. In this work, commercially available (Coherent) continuous wave (CW) carbon dioxide (CO_2) laser operating at 10.6 µm wavelength was used to irradiate the samples with a set of disks on them (Figure 2.16).

The sample containing the disk array was fixed on a small flip motion stage. An optical setup was designed in such a way that a Thorlabs He-Ne laser (with a light emission at 633 nm) was used as an alignment laser, and Coherent CW CO_2 laser was focused over the sample through a zinc-selenide (ZnSe) plano-convex lens. The operating power of the carbon dioxide laser was controlled with customized software and kept around 10W. The reflowing process is the last step to fabricate silica toroidal resonators on the silicon pillars (Figure 2.17).

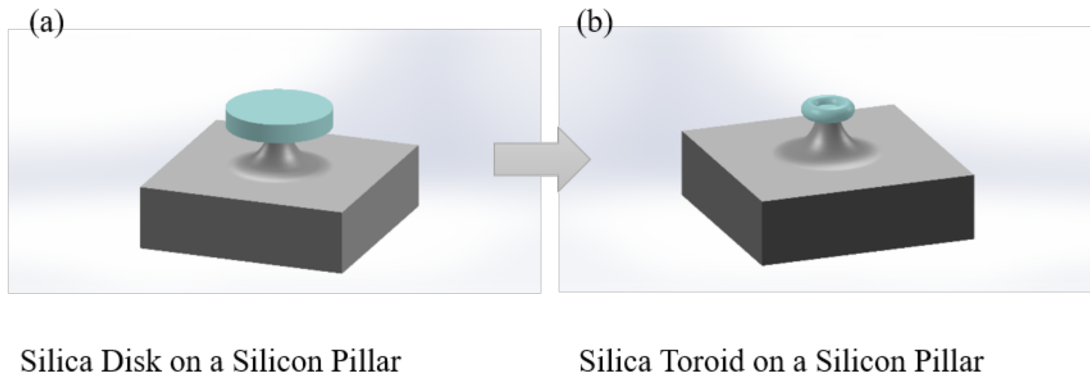

Figure 2.17: Toroidal resonators formed from silica disk resonators by the reflowing process. (a) Disk resonator, (b) Toroidal resonator after reflowing

The SEM images of a reflowed toroidal resonator can be seen in Figures 2.18 and 2.19.

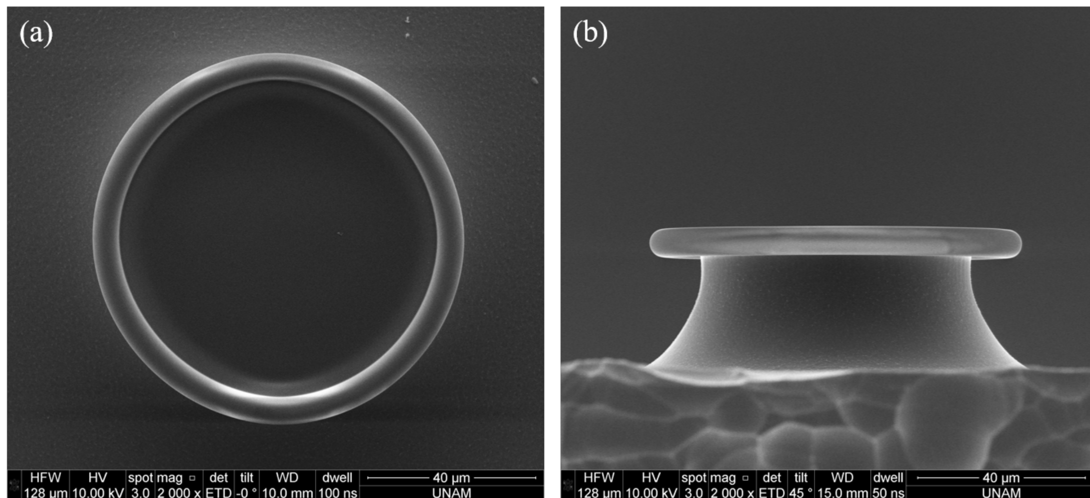

Figure 2.18: SEM images of a fabricated silica toroidal resonator from (a) top view, (b) side view, (c) tilted view.

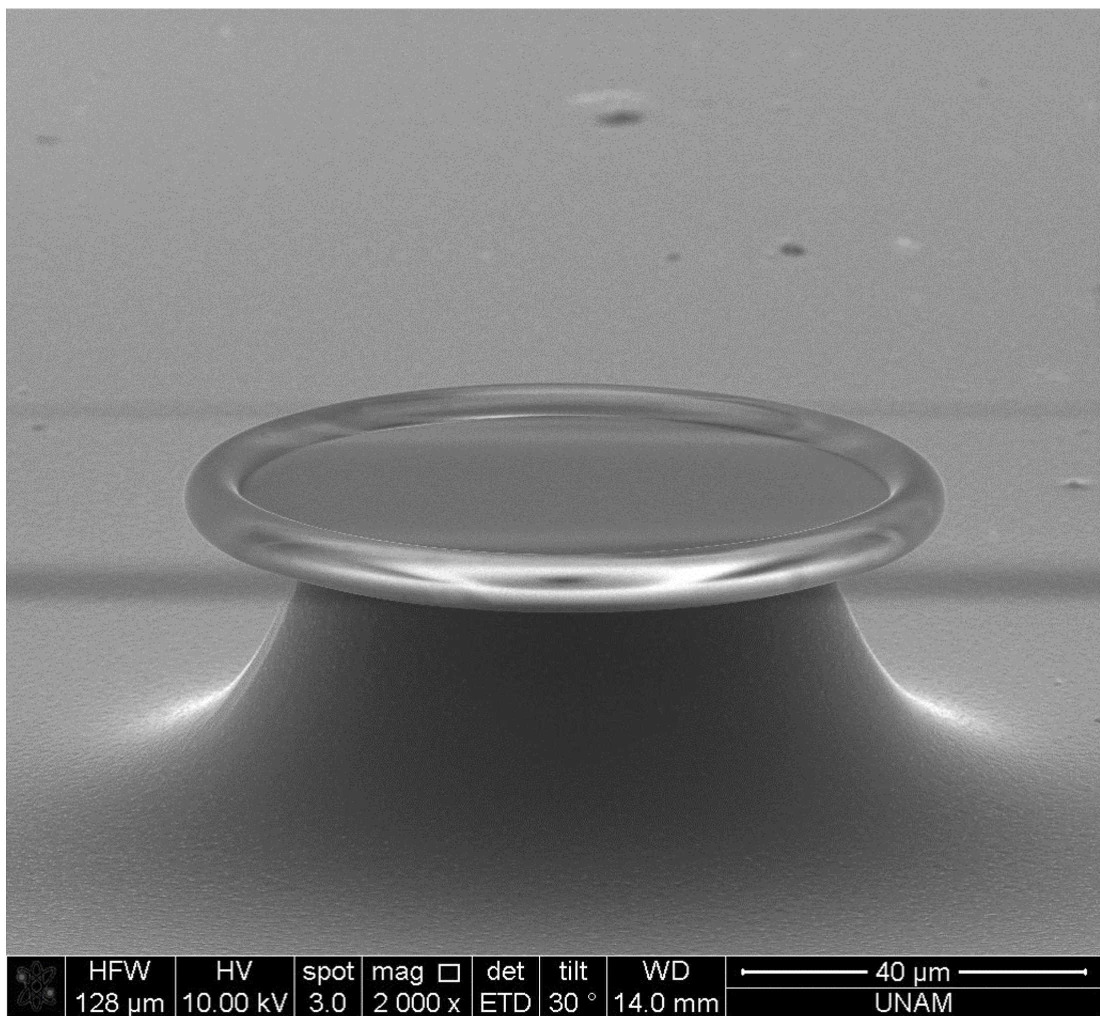

Figure 2.19: Tilted SEM image of a fabricated silica toroidal resonator.

Chapter 3

Optical Fiber Tapering and Light Coupling

3.1 Light Coupling

Optical resonators, while being useful for a variety of applications in the field of photonics, still require light – electromagnetic radiation – from an external source in order to utilize it for the desired purpose of the application. The electromagnetic radiation from the external source needs to be transferred into the resonator in an efficient and controllable fashion either by using a waveguide of a sort, or without it. A similar approach is also applicable in order to gather light from the resonator as well. Ideal coupling requires phase matching, spatial field overlap, and efficient (ideally 100%) energy exchange without any parasitic coupling of unwanted modes.

There are several coupling methods in order to couple light into a resonator and extract it from it. It is possible to couple light into a resonator via free-space coupling, in which light –generally laser light- is aligned to the coupler directly instead of utilizing any physical waveguide. Apart from free space coupling, there is a coupling type that utilizes optical fiber couplers – a glass slab that has

a trimmed, bent fiber embedded on top. It is also possible to use a prism for optical coupling. Another method is using a tapered fiber, in which case it is called evanescent field coupling.

Optical fiber couplers (OFCs) (Figure 3.1) are components compromised of an optical fiber and a glass slab. Glass slab is engraved in order to fit an optical fiber inside the engraved cut. Optical fiber was placed into the cut in such a way it formed an arc with a very high radius. Then the middle top part was trimmed slightly in order to let an electromagnetic field leak out of the fiber. If a resonator is placed on top of that region, the field interacts with it, which leads to optical coupling [12, 45, 46, 47]. OFC is a robust and good method for optical coupling, but due to its geometry, its application is limited and mostly used for spherical resonators.

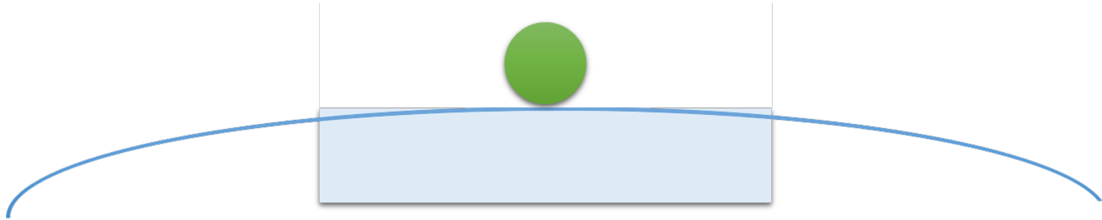

Figure 3.1: Optical fiber half coupler utilized to couple light into the spherical resonator.

As shown in Figure 3.2, prism coupling is also another option for optical coupling [48, 49, 50]. Instead of using a waveguide, a prism is utilized and incident light directed into the prism refracts to the other surface of the prism that shares a boundary with a resonator. By adjusting the incident angle, it is possible to achieve phase matching leading to successful optical coupling. Although they are useful for several applications, prism couplers are bulky, and it is challenging to utilize for some resonator geometries such as toroidal and ring.

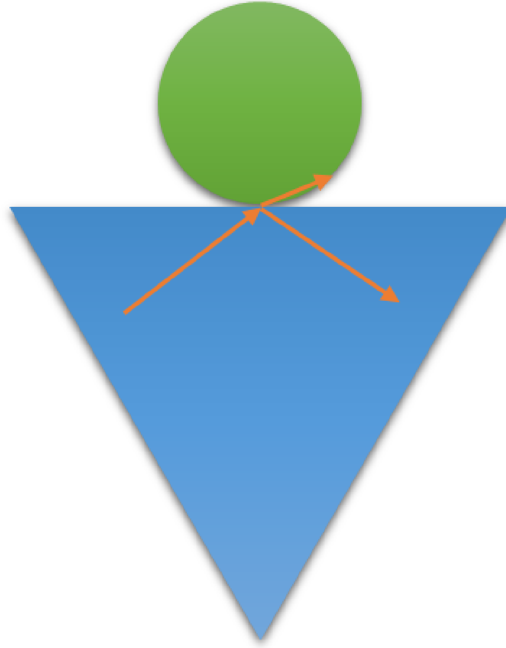

Figure 3.2: Incident light coupled into a spherical resonator by using a prism.

Another method for optical coupling is free space coupling [51, 52, 53, 54]. This method does not depend on a waveguide or an optical component for coupling. However, due to the need for precision, it generally requires optical components such as lenses and mirrors for precise optical alignment, which is crucial for optical coupling. The incident light is aligned onto the resonator directly, either a part of the resonator surface or the whole surface. If free space coupling is used in order to couple light into a resonator, then the application may require another method to gather light from the resonator. This may complicate the optical setup and introduce additional problems.

Among all of the methods, tapered optical fibers (Figure 3.3) are the most prominent method to couple light into a whispering gallery mode resonator in terms of coupling efficiency [55]. Therefore for both coupling efficiency and ease of application, tapered fiber was chosen for the experiments in this thesis. The reason for tapering the optical fiber is to enable and enhance the evanescent field coupling. It is possible to etch a fiber with etchants such as hydrofluoric acid (HF) to remove the cladding of the fiber and expose the core of the fiber in order to enhance the evanescent field coupling [56], however tapering process, which

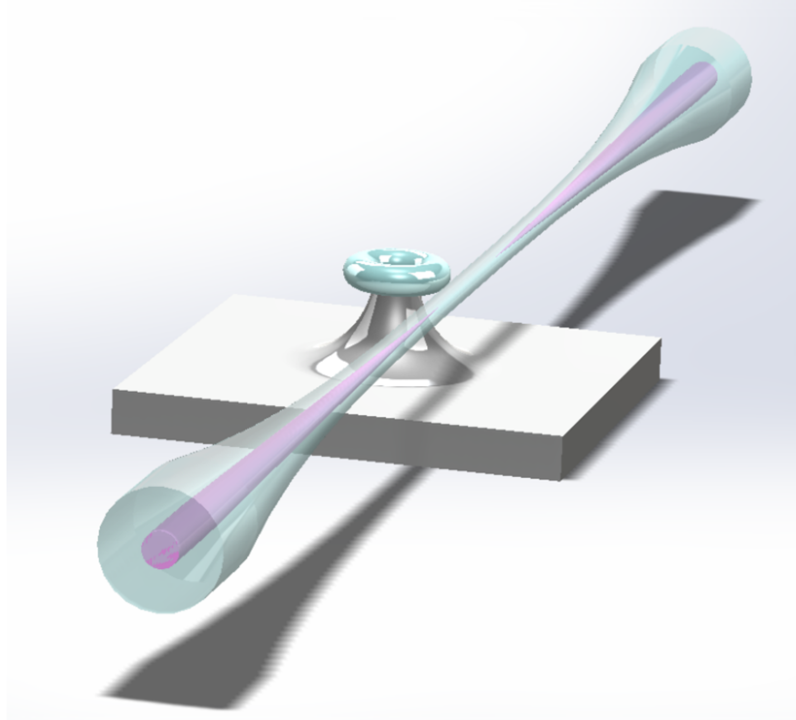

Figure 3.3: Light coupling into the toroidal resonator by using tapered optical fiber.

diminishes the core and allows light to move through cladding only, generates better results. Tapered fibers enable extremely efficient energy transfer (almost 100%) to optical resonators at critical coupling [57] and demonstrate high ideality [58].

3.2 Evanescent Field Coupling

Optical fiber consists of core, cladding, and (polymer) coating that offers mechanical durability to the enclosed core and cladding, which are glass. In order to achieve evanescent field coupling efficient enough for optical applications, the fiber needs to be tapered. This process involves removing the polymer coating of the fiber from the region selected for tapering and then increasing the temperature of that region either by torch or laser heating up to the temperature required to soften the fiber material (glass). Pulling fiber from both sides while heating

elongates the fiber. The diameter of the fiber begins to decrease while the length increases due to the conservation of volume [59].

Assuming that the fields of the optical fiber are linearly polarized, the fundamental mode can be written as;

$$F_o(a) = N_f \begin{cases} J_0^{-1}(k_f r) J_0(k_f a), & \text{if} \quad a \leq r \\ \exp\left[-\gamma_f (a - r)\right], & \text{if} \quad a > r \end{cases} \tag{3.1}$$

where a is the radial variable, r is the radius of the tapered fiber, while;

$$N_f = \alpha_f J_0(k_f r) \Big/ V_f \sqrt{\pi} J_1(k_f r) \tag{3.2}$$

$$\gamma_f = \alpha_f K_1(\alpha_f r) \Big/ K_0(\alpha_f r) \tag{3.3}$$

In Equations 3.1 - 3.3, J_0 and J_1 are the Bessel functions of zero and first order, K_0 and K_1 are the modified Hankel functions of zero and first order, while;

$$\alpha_f = \sqrt{\beta_f^2 - k^2 n_c l^2} \tag{3.4a}$$

$$k_f = \sqrt{k^2 n_c^2 - \beta_f^2} \tag{3.4b}$$

$$V_f = kr\sqrt{n_c^2 - n_{cl}^2} \tag{3.4c}$$

where n_c and n_{cl} are core and cladding refractive indices while β_f is propagation constant. By using the previous equations, the evanescent field of the tapered fiber can be calculated. It can be noted that the taper waist is an important factor for maximizing the evanescent field as well as achieving phase matching. It is desirable to use sub-wavelength tapers, which have a taper waist smaller than the wavelength of the transmitted light, in order to have efficient light coupling.

As mentioned previously, optical coupling depends on the phase matching between the resonator modes and waveguide modes and the spatial overlap of those modes. The experiments presented and detailed in this work utilized tapered optical fiber as a waveguide and toroidal resonators as a resonator. Although toroidal

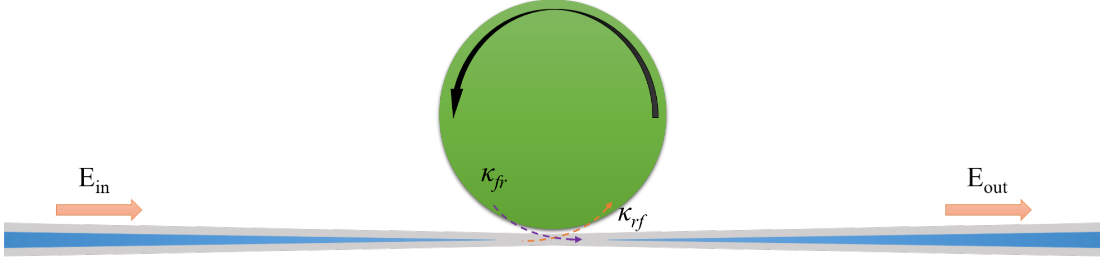

Figure 3.4: Top view of a schematic of an evanescent field coupling from tapered optical fiber into a resonator.

geometry differs from spherical geometry, it is possible to use spherical geometry to explain the theory of the evanescent field coupling for simplicity. In Figure 3.4, the schematic of a tapered fiber coupled with a resonator is shown. E_{in} and E_{out} indicate the incident and transmitted electric fields, respectively, while κ_{fr} and κ_{rf} are coupling coefficients to fiber-from-resonator and resonator-from-fiber.

The coupling coefficient, which indicates the strength of optical coupling between the resonator and the waveguide, is given by the following formula [60];

$$\kappa_{rf} = \frac{\omega \varepsilon_0}{4}(n_r^2 - n_0^2) N_f N_r \times \iiint_V (E_f^t \cdot E_r^t + E_f^z \cdot E_r^z) e^{i\Delta\beta z} dxdydz \tag{3.5}$$

in which, E_f^t and E_f^z represent the transversal and longitudinal components of the electric field of the fiber while E_r^t and E_r^z represent the same components of the resonator. V is the volume of the (spherical) resonator, while n_r and n_0 are the refractive indices of the resonator and the environment surrounding the resonator, which is air in our case. $\Delta\beta$ is the difference between the propagation constants of the resonator and fiber. N_r and N_f are used to normalize the power of the resonator and fiber, respectively.

In order to achieve phase matching, the propagation constants for both the resonator and the waveguide needs to be similar. Assuming that our waveguide is a tapered optical fiber and fundamental mode (HE_{11}) is being guided through the fiber, the propagation constant can be calculated by using [61].

$$\beta^2 = k^2 n_f^2 - 2.405^2 / r_f^2 \tag{3.6}$$

where k is wavevector, n_f and r_f are the refractive index of the fiber and radius of taper waist of the fiber, respectively. If the optical fiber is silica, then the

refractive index is $n_f = 1.44$. Effective refractive index (n_{eff}) of the fiber, then, can be calculated by using the following:

$$\beta = \frac{\omega}{c} n_{eff} \tag{3.7}$$

where ω is the angular frequency of light and c is the speed of light in the vacuum. Therefore, after calculating the effective refractive index of the fiber, the propagation constant difference can be estimated by:

$$\Delta\beta = \frac{\omega}{c} \left(n_{eff,f} - n_{eff,r} \right) \tag{3.8}$$

where $n_{eff,f}$ and $n_{eff,r}$ are effective refractive indices of the fiber and resonator, respectively. The smaller the difference between the propagation constants, the greater the phase matching between the resonator and the fiber. Optical coupling can be achieved much better with great phase matching achieved.

3.3 Fiber Tapering

Although earlier work for fiber tapering was done with carbondioxide laser, later, the tapering setup was altered, and the fibers were tapered by a hydrogen torch. Therefore, in this section, both methods will be covered. Essentially the major components of the experimental setup for achieving fiber tapering either by hydrogen torch or carbondioxide laser are the same, so the setup did not require major change apart from the heating elements, which are laser and torch for their respective methods. SMF-28 fiber was used in the experiments that are covered by this thesis. SMF-28 is a single-mode optical fiber with an 8 µm diameter silica core and 125 µm diameter silica cladding covered by a polymer (Figure 3.5). It is ideal for optical transmission for communication band (1550 nm).

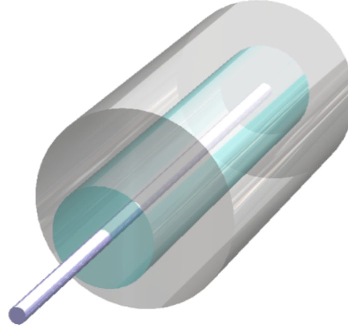

Figure 3.5: Illustration of an SMF-28 optical fiber detailing core (blue colored), cladding (light blue colored), and coating (light gray colored).

3.3.1 Fiber Tapering with Carbondioxide Laser

Since silica has good absorption at 10 µm wavelength band, it is possible to utilize carbondioxide laser in order to taper a silica optical fiber. The indicent light emitting from carbondioxide laser focused onto the silica fiber, and depending on the waist radius and the power of the carbondioxide laser, it is possible to reach a high temperature that is required to soften silica. After achieving softening of the silica it is possible to pull the silica fiber from both sides and make it elongated. Since the volume should stay the same, the elongation causes the waist diameter to decrease. The decrease in the waist diameter causes less power to be absorbed by the fiber; therefore, the beam diameter of the laser light should be reduced as well to keep up with the temperature requirements.

In Figure 3.6, the fiber tapering setup with carbondioxed laser is shown. SMF-28 optical fiber is first plugged into the laser (Santec) operating within the communication band (1550 nm). The other end of the fiber is connected to the optical detector, and the detector is connected to the optical power meter (ThorLabs). Powermeter and laser are plugged to the oscilloscope (Tektronix). Then part of the fiber – that is going to be heated for tapering – is cleaved, which means the removal of the polymer coating covers the cladding. The stripped region is

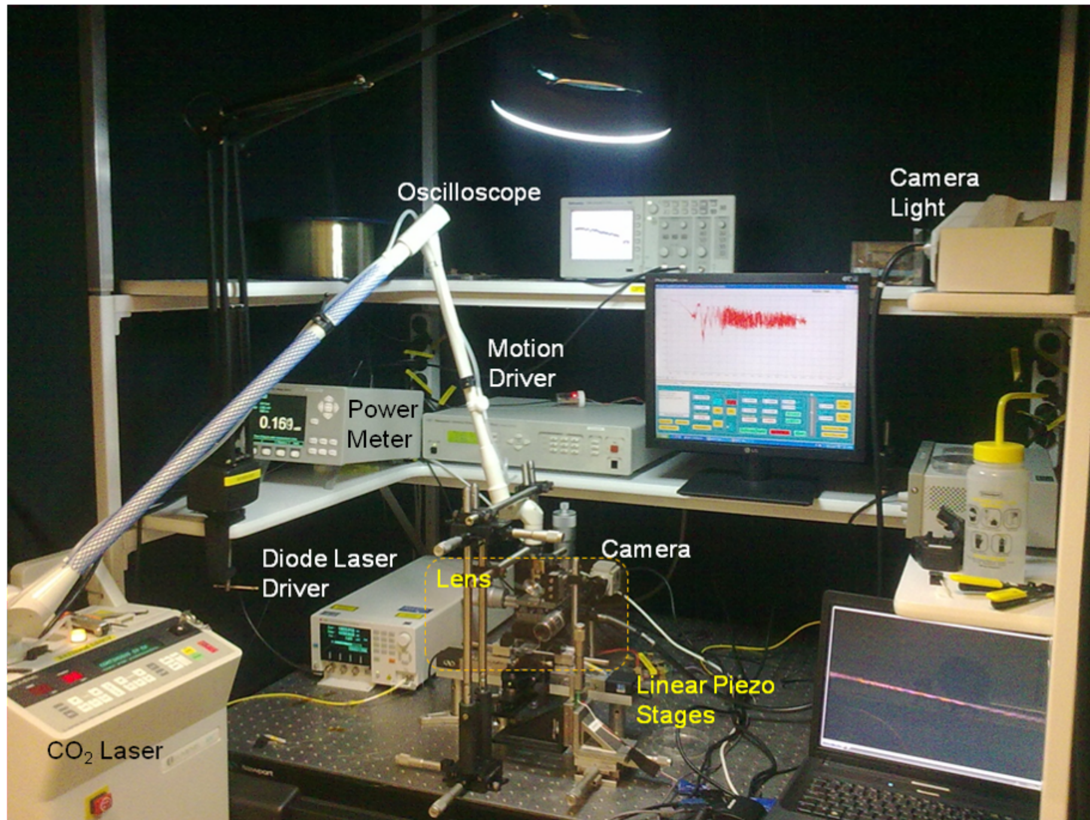

Figure 3.6: Fiber tapering setup with carbondioxide laser. The output of the diode laser is plugged to silica fiber and the other end of the silica fiber is plugged to the photodetector connected to the power meter. 2 cm. length of the fiber's coating is removed and that bare fiber is fixed between two fiber holders on two oppositely aligned linear piezeo stages. CO_2 laser and lens are aligned on top of the bare fiber.

cleaned from dust and remnants by using IPA, and then the fiber is placed onto the two fiber holders (Figure 3.7). Fiber holders are fixed onto the two separate linear stages that are controlled by a motion controller (Newport). Optical scope with a CCD camera plugged is placed to monitor the optical fiber clamped between two fiber holders. Finally, the carbondioxide laser is aligned on top of the optical fiber. A zinc selenide lens is used to focus the light coming from the carbondixoide laser, and it is utilized to modify the heating zone.

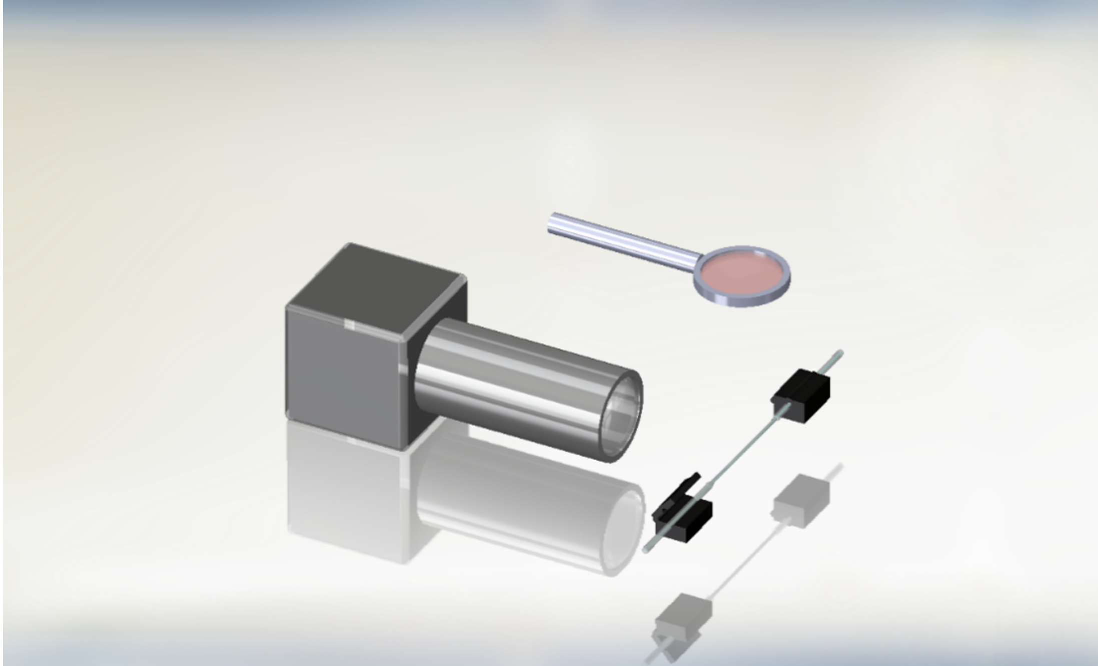

Figure 3.7: The zinc selenide lens in the fiber tapering setup required to control the heating zone.

In Figure 3.8, an optical image of a tapered fiber can be seen. The optical fiber shown in the image belongs to a tapered SMF-28 silica fiber following to failed tapering process. Tapering failure can happen due to a number of reasons. In most cases, it is due to the failure to supply enough heat to the fiber to sustain the softening temperature that allows the elongation of the fiber while pulling the fiber apart mechanically. While using carbondioxide laser to heat up the fiber, it is imperative to sustain enough heat while pulling the fiber apart since while tapering, the energy transfer to the fiber decreases. The absorption of the fiber naturally depends on the diameter of the fiber. As tapering progress, fiber diameter decrease; therefore, absorbed energy decrease resulting in less heat. This should be compensated by increasing the laser power or focusing the beam into a much smaller region (heat zone). In the setup pictured in figure 3.6, the rotating lens (detailed in 3.7) is used to change the heat zone area. The tapered fiber shown in Figure 3.8 did break due to the failure the keep up the heat on the fiber.

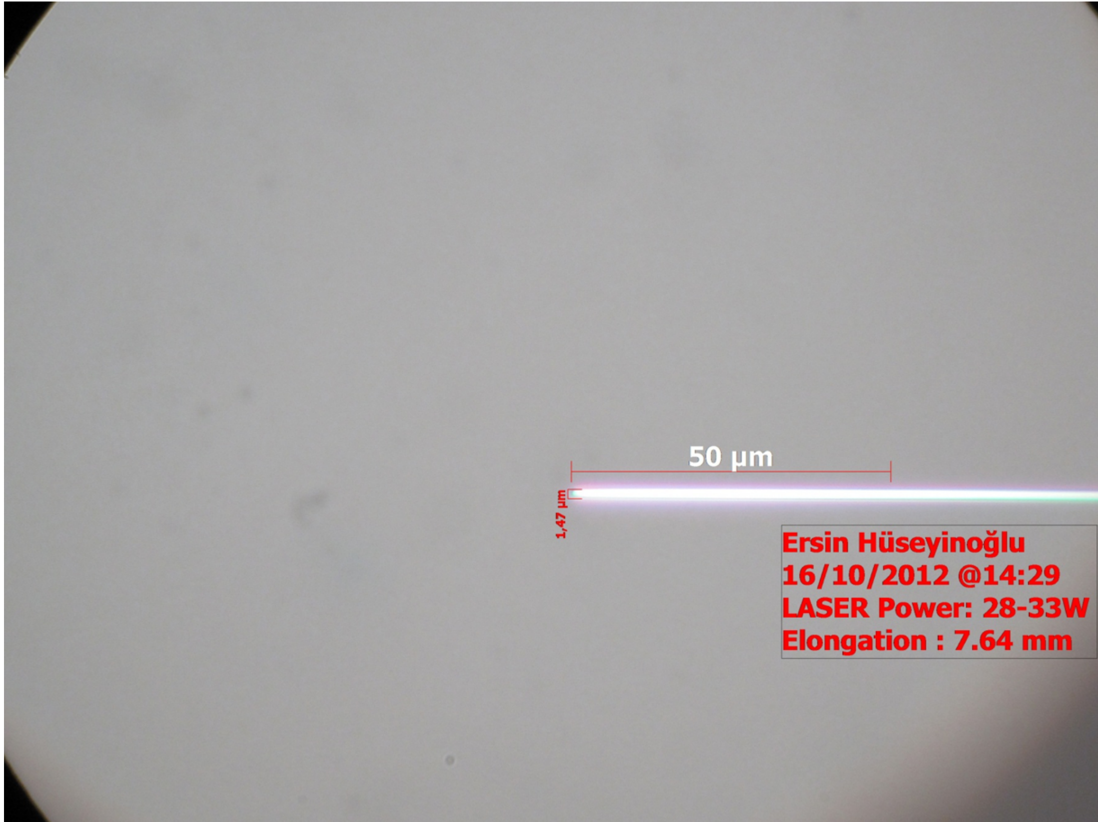

Figure 3.8: An optical image of a broken tapered fiber following to a failed tapering process.

Another problem that can be seen while tapering is adiabaticity. It is important to achieve adiabatic tapering since the non-adiabatic process can lead to huge optical loss while transmission. In an ideal adiabatic tapering, the decrease of the fiber diameter is gradual and smooth. This smooth change in the diameter ensures the high transmission efficiency with minimum loss in power loss. In the case of non-adiabatic tapering, the loss in the transmission becomes problematic due to the back reflections. In Figure 3.9, an optical image of a tapered fiber as a result of a non-adiabatic process.

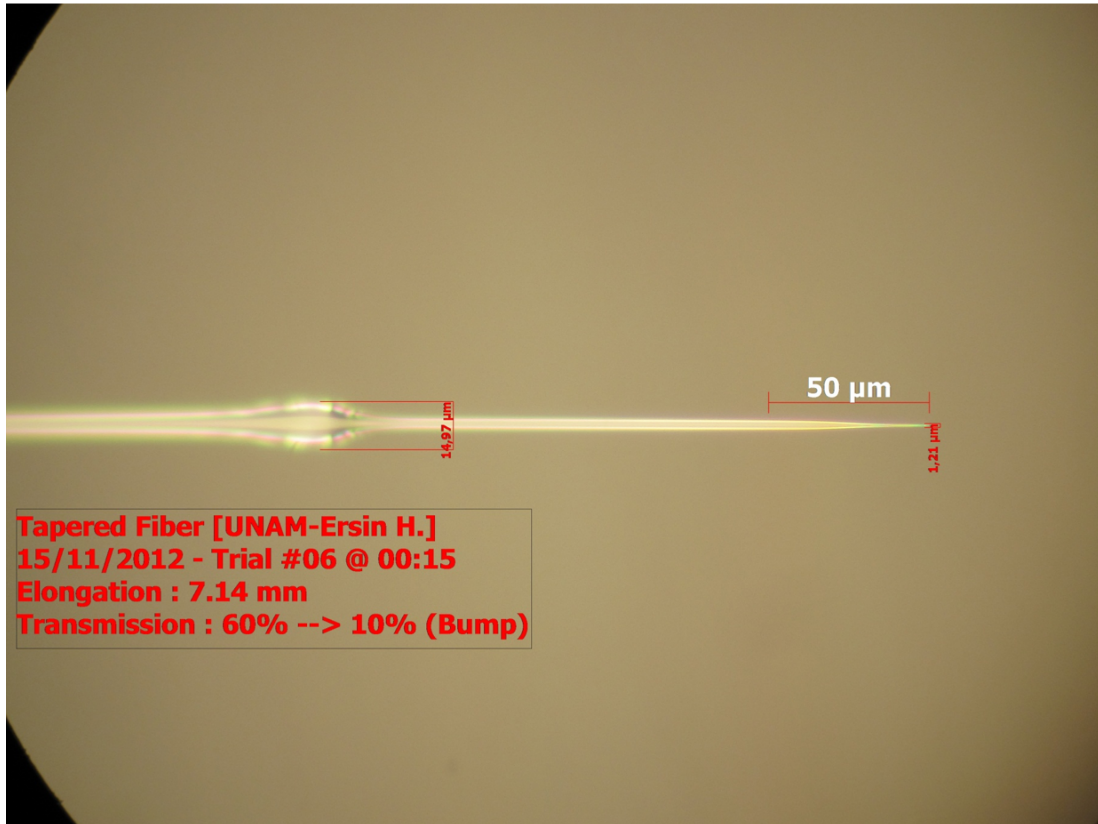

Figure 3.9: An optical image of a non-adiabatic tapered optical fiber.

3.3.2 Fiber Tapering with Hydrogen Torch

Although fiber tapering is achieved by carbondioxide laser, it has low repeatability because of the unstable power output of the laser used in the setup. This issue led to an increase in the time duration spent for fiber tapering and hindered the optical experiments that should follow the tapering. Although optimizations were done to increase the efficiency and the repeatability of the tapering with laser, it became a necessity to change the setup in favor of a hydrogen torch instead of the carbondioxide laser. The carbondioxide laser and the lens shown in Figures 3.6 and 3.7 were removed from the setup, and a hydrogen torch was placed 3.10.

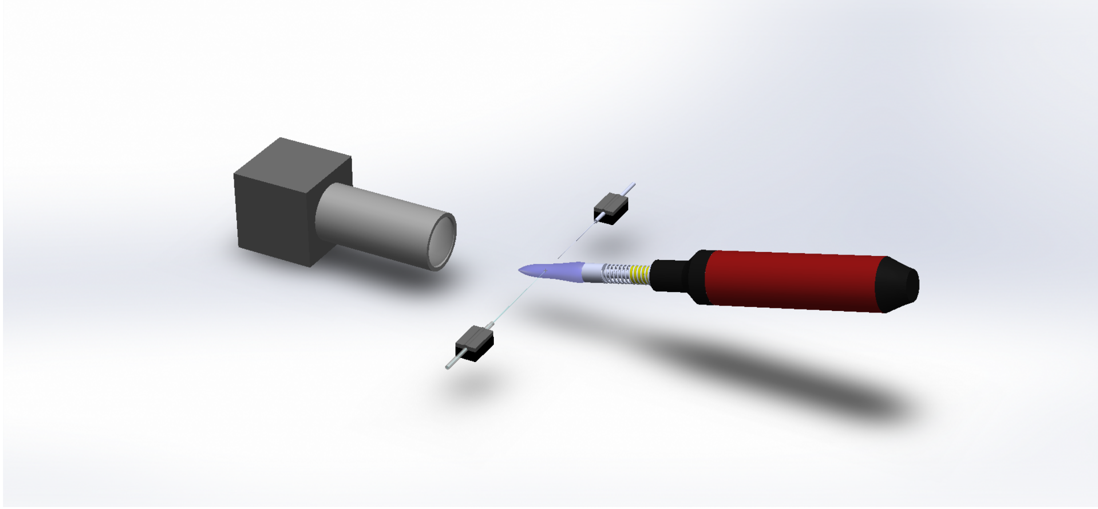

Figure 3.10: Drawing of the tapering system with hydrogen torch.

Apart from the torch that replaced the laser, the tapering setup stayed the same. Initially, the polymer coating of the fiber is removed, then it is cleaned by using IPA and then placed onto the fiber holders that are fixed on the linear stages at the opposite sides. The hydrogen torch is fired and then moved to the close proximity to the fiber.

The heating process begins while light from the probe laser (Santec) is transmitted through the fiber. While the diameter of the fiber (both the core and the cladding) begins to decrease gradually during the tapering process, the tapered region of the fiber begins to support multimode while the rest of the fiber cannot. At this stage, the fluctuations can be seen in the transmission spectrum. As the diameter of the fiber gradually approaches to the order of the transmission wavelength, the fluctuations begin to decrease and then diminish. Ideally, this taper diameter is the targeted diameter, and if the process allows a smooth tapering profile with good adiabadicity, it is possible to have a low-loss tapered optical fiber. Transmission spectra taken during the fiber tapering process in previous optimization periods were given in Figure 3.11 as an example of an ideal tapering process.

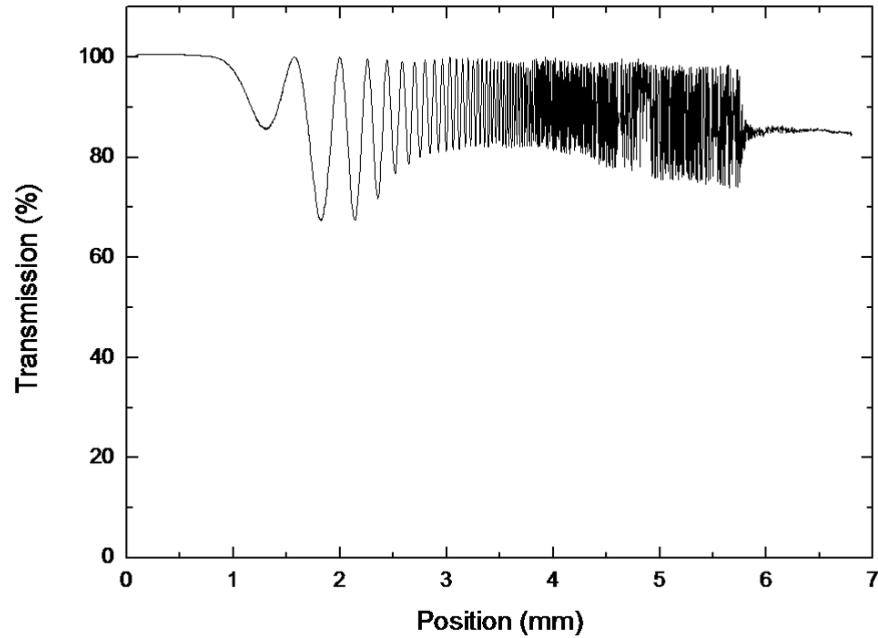

Figure 3.11: Transmission spectrum recorded during the fiber tapering process.

As it can be seen, the tapering is achieved successfully with a low loss with high transmission at 80%. It can be seen that while tapering, the fiber begins to support multimode, and that manifests itself on the transmission spectrum. After fiber was pulled 6mm opposide sides equally, the fiber stops to support multimode and becomes single-mode again.

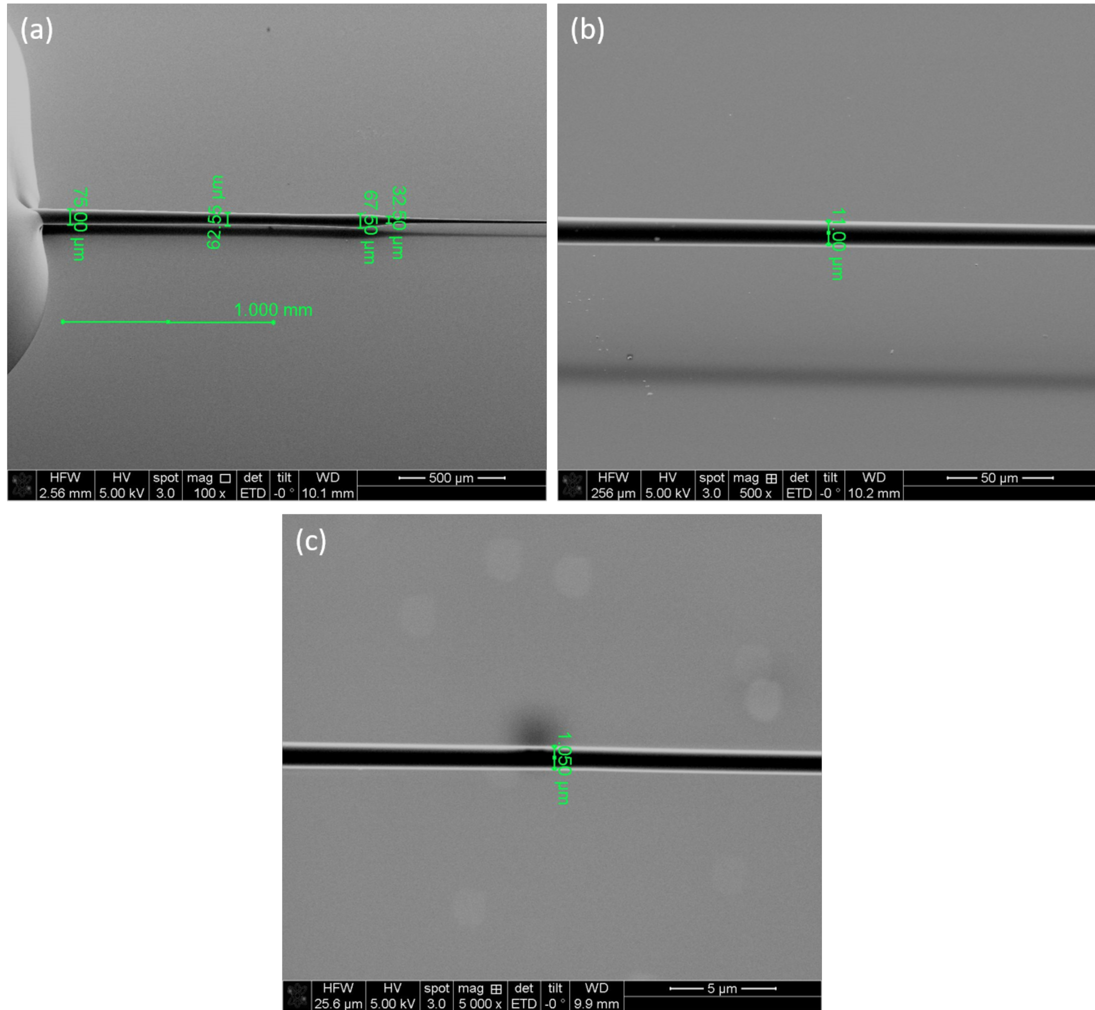

Figure 3.12: SEM images of a successfully tapered fiber. Three consecutive images were from the thickest to thinnest waist diameter.

The targeted taper diameter is the diameter close to the transmission wavelength or sub-wavelength. In our tapering experiments, our tapering setup achieved sub-wavelength diameters of approximately 1 µm (Figure 3.12). Following the successful fiber tapering, a resonator can be coupled to the tapered fiber, as can be seen in in Figure 3.13.

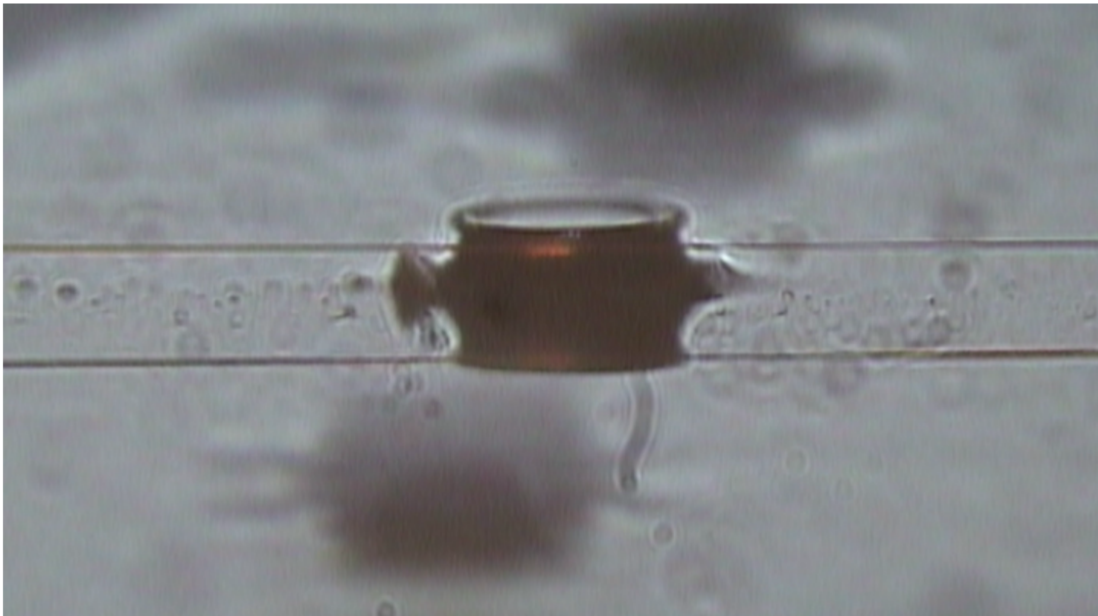

Figure 3.13: Light coupling to a toroidal resonator from a tapered silica fiber. The fiber is moved to close proximity to the toroidal resonator while monitoring the transmission. The drop in the transmission indicates a successful light coupling.

Chapter 4

Mass Production of Toroidal Resonators by Fast Reflowing with Scanning LASER

4.1 Fabrication Process of Silica Toroidal Resonator and Its Limitations

Even though the wide application range of optical surface-tension-induced microresonators (STIMs) is promising and has potential for wide commercialization, there is one limiting factor for their commercialization; manufacture. This has two facets; the first one is the process itself is time-consuming, and the second one is that, similar to every fabrication process, it is susceptible to deviations from its original design. The problem of production time is related to the tedious process of resonator fabrication, and this process is especially time consuming when producing toroidal resonators. The production process of toroidal resonators consists of two separate phases; microfabrication (conducted in the clean room) and reflowing.

Reflowing is the process that gives the final shape to the STIM, and this process is time consuming. Apart from two exceptions, such as extremely high-temperature fabrication of wafer-scale silica resonators [62] and fabrication of 2D arrays of chalcogenide microspheres [32], fast and affordable mass production of STIMs has not been demonstrated yet. Although the two exceptional aforementioned works [32, 62] utilized furnaces, the common approach for fabricating toroidal silica resonators is to fabricate silica disk resonators on a silicon pillar on top of a wafer by using the silica microfabrication process already settled by microelectronics applications. Then heating the disk resonator by a laser to induce heat hence reflowing the disk geometry into the toroidal form [33, 35, 63]. The laser source is carbondioxide laser since it emits light at the wavelength of 10.6 µm that can be absorbed well by silica but not by silicon in comparison. While the silica disk is heated up due to absorption up to a temperature that allows reflowing, the silica pillar acts as a heat sink since it does not absorb in that wavelength range. This leads to a reflowing process that can be used to achieve the final product of the toroidal resonator. The crucial part of the process is to optimize the laser power density to allow a successful process. Inadequate heating due to low power leads to partial reflowing [64] that may render the resonator non-useable for the desired application, while excessive heating ends up with a distorted-shaped resonator.

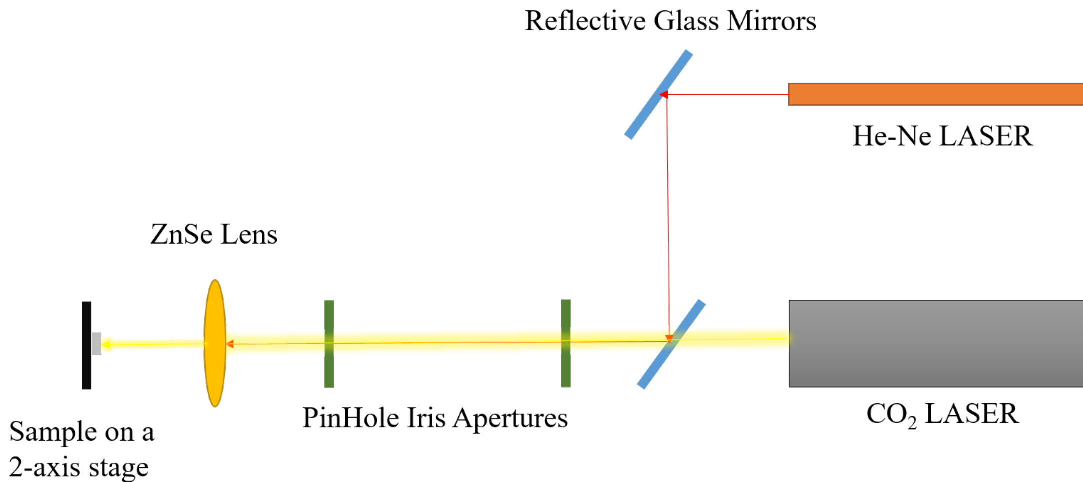

Figure 4.1: Reflowing setup with fixed carbondioxide laser

In Figure 4.1, the illustration details the reflowing setup used for reflowing resonators used in my previous batches. A carbondioxide laser is used for heating the samples through a zinc-selenide (ZnSe) lens, while a He-Ne laser is used for alignment purposes. Even though the process seems easy to achieve, it is time-consuming. In order to fabricate on-chip STIMs, especially microtoroidal resonators, a carbondioxide laser is needed to be focused on the resonator so the laser energy that is required for the reflowing can be absorbed. This procedure needs to be done to each resonator one by one, and if you have a set of resonators, all need to be placed into the reflowing setup and then reflowed with the laser one by one each time. Absorption and reflowing themselves do not take long periods of time; however, placing and aligning the resonator to the laser takes time. Due to this process, even though standard microfabrication techniques allow us to mass-produce resonators, mass-scale fabrication of STIM hits a bottleneck at reflowing step. Therefore, if a method is proposed to reduce the time required for reflowing, it can greatly help the mass production of the toroidal silica resonators hence helping the commercialization of the resonators to be used for a wide range of applications.

A method is proposed for the reflowing process to decrease the required time. Instead of using a fixed alignment carbondioxide laser, using a laser engraver that is capable of scanning a plane (X-Y plane) which is also capable of setting focus on the Z-axis, it is possible to scan an entire surface of a wafer with a set of resonators on top. The process is fast and repeatable, and the laser settings such as scanning speed, focus, scanning range, and the power level can be arranged and modified for specific requirements.

4.2 Mass Reflowing by Using Commercial CO_2 Laser Engraver

In this work, the motivation was to achieve a fast, cost-effective, and reliable method for mass fabrication of wafer-scale microtoroids (Figure 4.2). This kind of method may increase the usage of toroidal resonators and lead to utilization in a wide range of applications in the photonics industry.

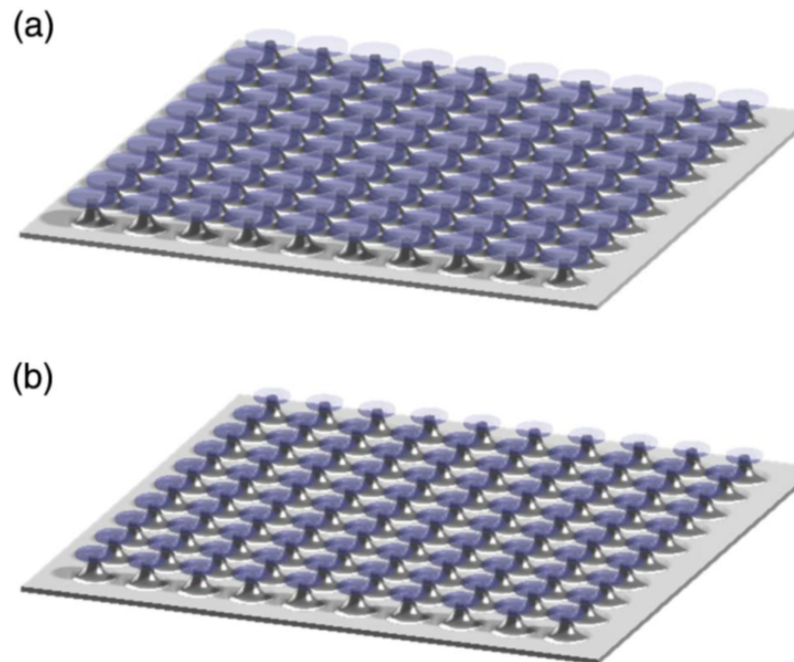

Figure 4.2: (a) Array of microdisks produced on a chip by standard microfabrication techniques. (b) The array of microdisks is reflowed to produce high Q-factor microtoroids.

4.2.1 LASER Engraver

Instead of using a fixed alignment carbondioxide laser, an engraver carbondioxide laser is chosen in raster scan mode in order to reflow a set of disks on top of a substrate. A commercial product Zing LASER Engraver (Figure 4.3an inset picture) is used in this work. Although having several parameters, one of the most important parameters in this process is the temperature of the reflow. If the silica is not adequately heated, it leads to partial – hence incomplete – reflowing, and if the temperature is too high to heat the silica, it can distort the geometry further hence rendering the whole batch (set) of the resonators unusable.

The optimum temperature is crucial for reflowing. Therefore, it is important to set the parameters of the LASER accordingly to achieve the optimum value. Since the absorption of the emitted laser light also depends on the thickness of the silica, it is imperative to change the parameters for different thickness values of the silica layer. The amount of energy absorbed is directly proportional to the path length of the light traveled within the silica layer due to the Beer-Lambert Law. In order to achieve the optical power suitable to reach the adequate temperature for reflowing, a set of variables can be controlled, such as; focus (in the z-direction), rastering speed, and laser power. By using a suitable combination of those parameters, it is possible to reflow in mass-scale a set of disk resonators rapidly.

The maximum power of the LASER is 30 Watts, and the power for the reflowing is set to 12%. The scan speed was 2% which corresponds to a scanning speed of 15 mm/s. It is also possible to set the resolution, and it was set as 1000 DPI in order to obtain uniform reflow. It is possible to use different variations of these values to fine-tune the reflowing for specific requirements. The scan was done by setting a rectangular pattern generated in a custom AutoCAD software associated with the Zing LASER. Since the output power can only be set in discrete steps, the substrate with microdisks was located 4 mm out of focus, closer to the laser head apparatus, in order to enable the fine-tuning of the optical power.

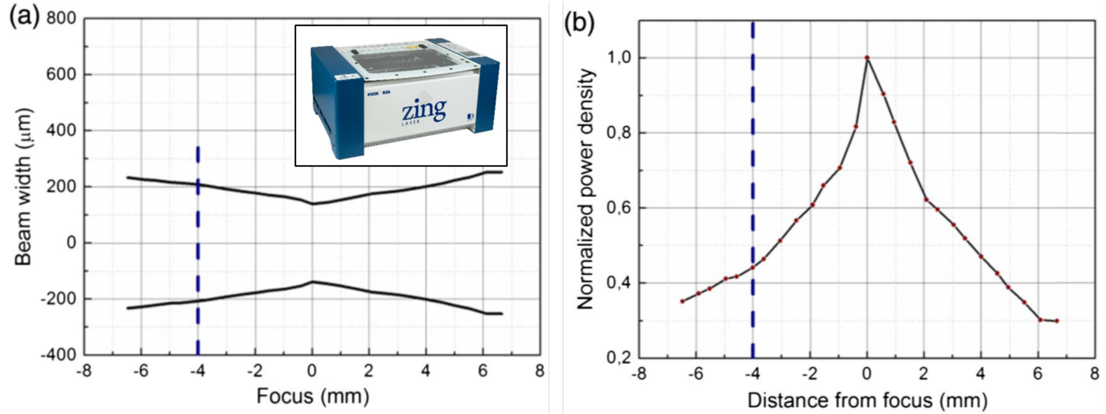

Figure 4.3: The effect of the distance on power density for reflowing and the observation of the CO_2 laser beam shape. (a) The thickness of the lines engraved onto the plexiglass substrate is considered the beam radius. The dashed line indicates the distance selected for the reflowing process. (b) Power density decreases with the inverse of the square of the spot radius.

In order to observe the reflowing performance and determine the laser beam shape of the engraving laser, two sets of trials were done. Initially, lines were drawn on a plexiglass sample with different distances between the sample and the laser head in order to figure out the change in the beam width when the laser is utilized out of focus. The thickness of the lines that were engraved onto the sample was considered as the beam radius of the laser. Figure 4.3.a indicates the beam diameter with respect to the distance from the focus. The beam waist was measured as 140 µm when the laser head was at focus, and it extends to 200 µm if the laser head is out of focus by 4 mm. At the focus, the power density was calculated as 58.5 MWm^{-2} at 12% power, while it corresponds to 26.3 MWm^{-2} when the laser head is 4 mm out of focus (Figure 4.3.b). This reduction has given enough fine-tuning control for reflowing, so the silica is heated enough to reshape as toroidal geometry while not much leading distortion in the toroidal shape.

4.2.2 Fabrication Process and Reflowing

A Silicon wafer with a 2.5 µm thermal oxide layer on top was used in order to fabricate silica disk resonators on top of silicon pillars. The fabrication procedure of the silica microdisks is the same as detailed in Chapter 2. The substrates were first patterned by using UV lithography, and then silica disks were created on top of the silicon layer by simply removing the silica unprotected by the patterned photoresist layer by using buffered HF solution (BOE). Following silica etching, the substrate did undergo the SF_6 plasma etching process to form silicon pillars under silica disks and a cleaning process (using acetone and IPA) to remove the photoresist.

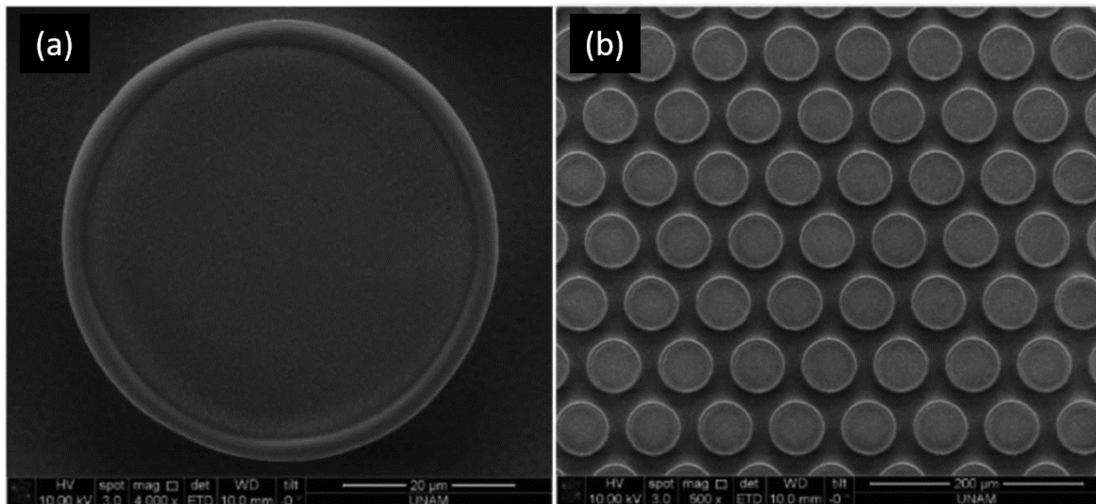

Figure 4.4: Scanning electron microscope images of (a) A single toroid in the array and (b) array of toroids on a chip.

Utilizing raster scanning reflow instead of individual reflowing enables high throughput fabrication of surface-tension-induced microresonators (STIMs). By using raster scanning, it is possible to reflow significantly more samples than the conventional way in a short amount of time. It is, of course, possible to fabricate various geometrical shapes instead of just toroidal shapes. By using a raster scanning laser, microdisk resonators fabricated in the clean room were reflowed. Scanning electron microscope (SEM) images of the reflowed resonators were taken and those microresonators on chip were shown in Figure 4.4.

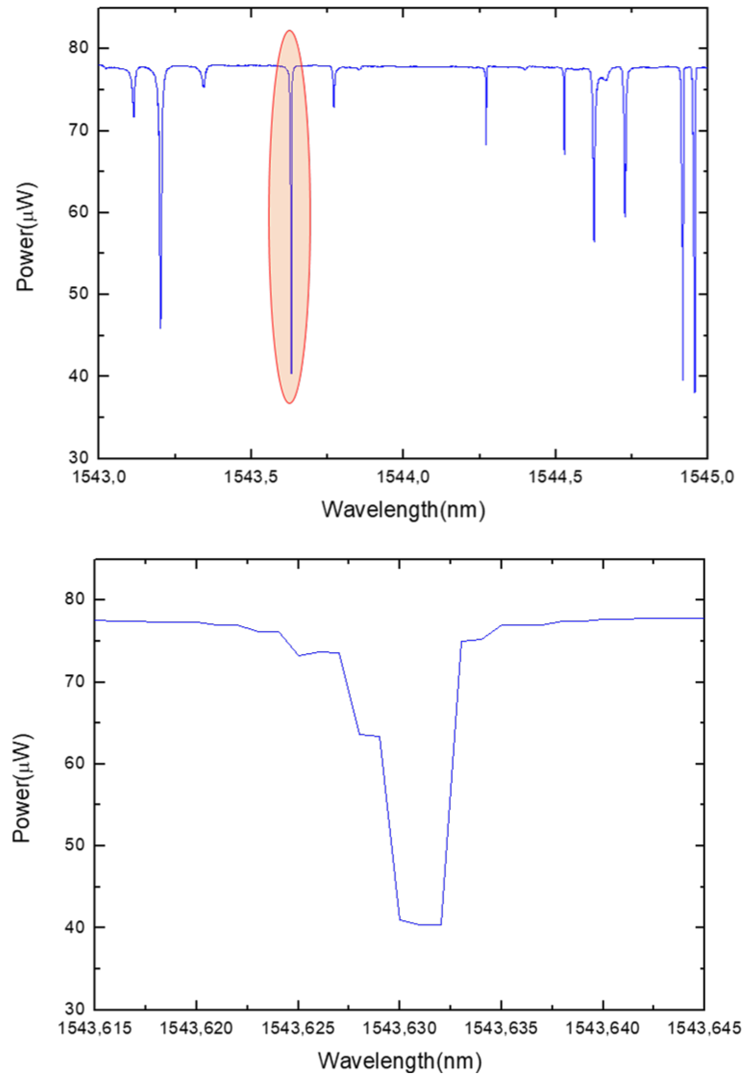

Figure 4.5: (a) Resonant mods recorded from a toroidal microresonator fabricated using raster scan diode laser. (b) One mod from the spectrum was chosen and detalied scan was conducted.

One of the fabricated silica toroidal resonators (on 2 x 30 mm substrates) were optically coupled by using tapered SMF-28 fiber connected to the Santec tunable external cavity laser and to the Newport optical power meter. Santec laser was operated at the telecommunication C-band (around 1550nm) while being controlled by custom-made software. A power meter has connected to the oscilloscope, and all the data were collected via the same custom-made software used to control the Santec laser.

The dips in the optical spectrum after the optical coupling was achieved were gathered and analyzed (Figure 4.5). The Q-factor of the resonator coupled was measured on the order of 10^5. Although it is expected to have Q-factors on the order of 10^6, this is still at acceptable level. Another resonator was coupled and Q-factor of that resonator was found to be 10^6 (Figure 4.6).

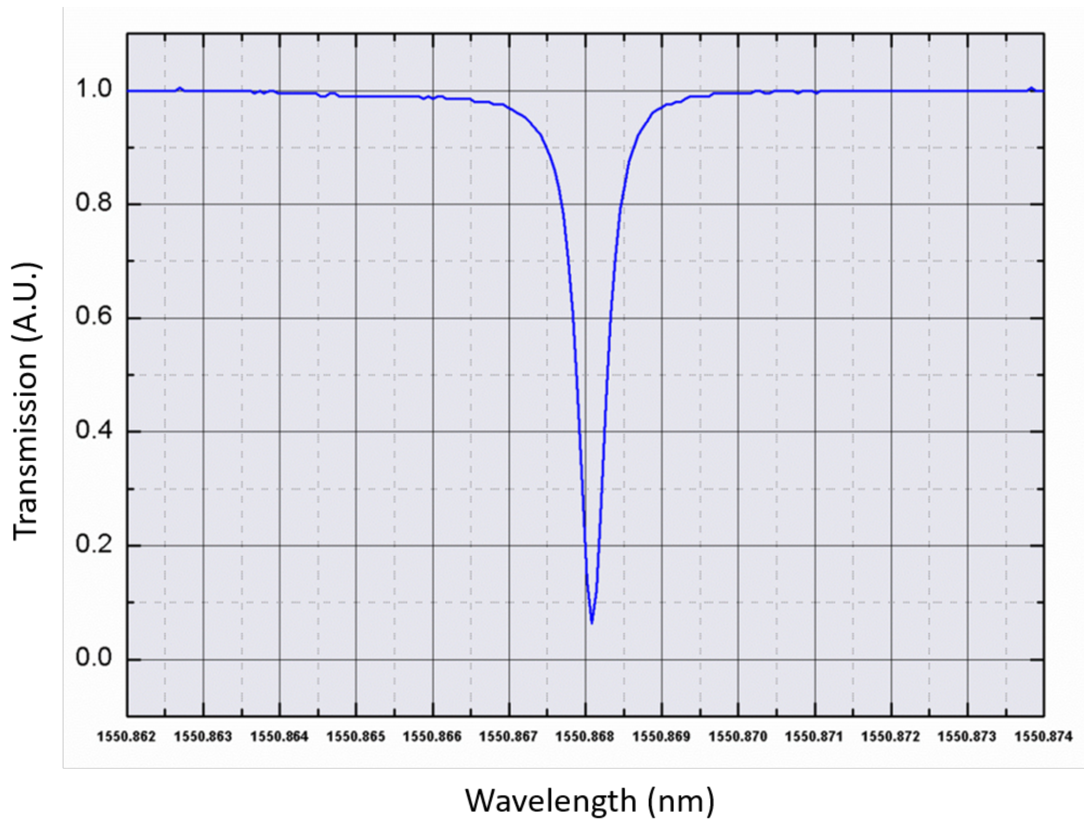

Figure 4.6: Resonant mod recorded from another toroidal microresonator fabricated using diode laser.

Another resonator was selected and coupled to the tapered fiber. A mod was selected and Lorentzian fit was performed to the gathered data by utilizing a custom MATLAB script on a selected resonant mode (Figure 4.7). The FWHM of the resonance was measured as 0.5 pm; therefore Q-factor was calculated as 3 x 10^6. The Q-factor reported in this work is lower than some of the other reports related to the silica microtoridal resonators, although it should be noted that the difference between those resonators and the resonator manufactured for this work is the silicon etching process. Silicon can be etched by using either XeF_2 or SF_6, and in this work, SF_6 was used within the ICP system. XeF_2 has very good selectivity, and it is extremely selective to etch silicon while silica is left unetched while the selectivity of the SF_6 is not on par with the XeF_2. Due to this difference, the Q-factor of the resonators produced is lower than the best reported on the order of 1-2 magnitude. However, it is still at acceptable levels for experimentation.

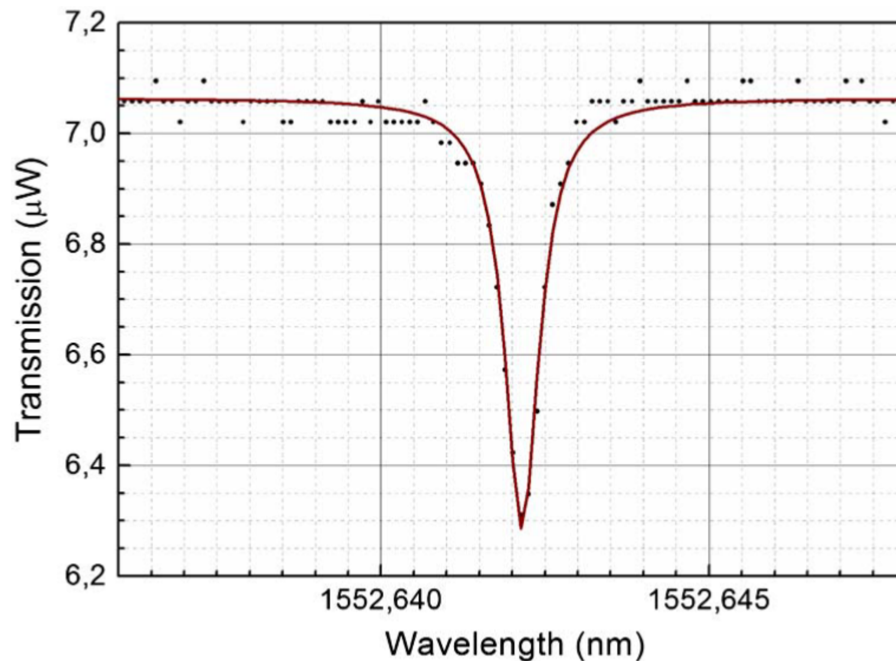

Figure 4.7: Resonant mod recorded from a toroidal microresonator fabricated using raster scan laser. Real data are shown with dots, and the line is a Lorentzian fit. Full width half maxima (FWHM) is measured as 0.5 pm and the Q-factor is 3 x 10^6.

Even though toroidal resonators have high Q-factors and low mode volumes, which make them desirable for a variety of applications, they are not the only resonator types being used in photonic applications. A variety of geometries such as ring, disk, racetrack, and elliptical are being used in other applications. Additionally, with this setup, it is also viable to scan the whole surface of a chip containing an array of structures with different geometries. For instance, on-chip resonators with integrated waveguides provide certain advantages over stand-alone resonator chips since those structures do not need the additional and tedious task of optical coupling. However, there is a problem with producing both surface-tension-induced microresonator and waveguide on a single chip because reflowing process increases the gap between the fabricated resonator and the waveguide. In a recent report, a method was demonstrated in order to fabricate on-chip devices that incorporate both STIM and waveguide [65]. It is possible to use the raster scanning method on this kind of structure as well.

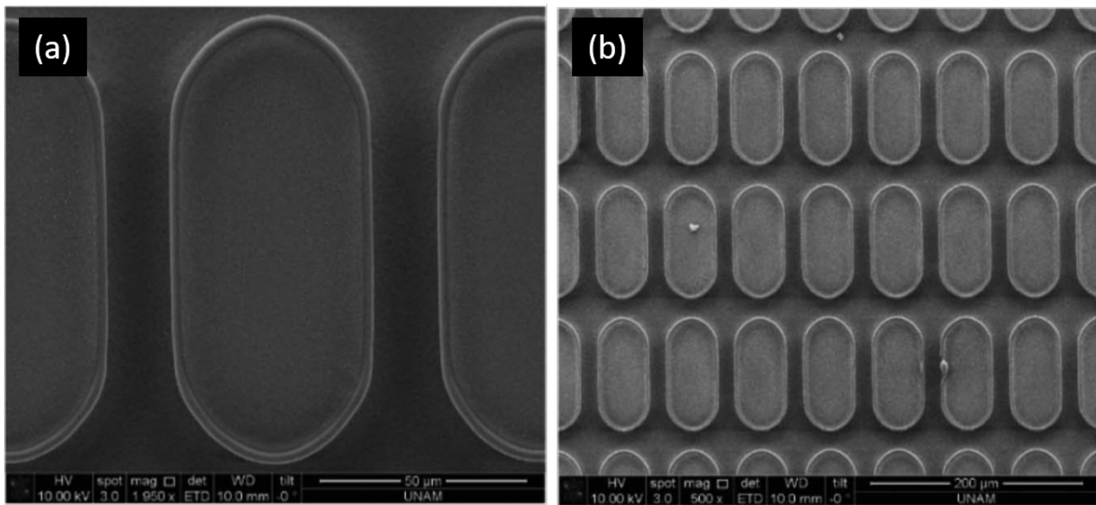

Figure 4.8: Scanning electron microscope images of (a) A single racetrack resonator in the array and (b) an array of racetrack resonators on a chip.

Racetrack resonators are also a good choice for applications. In one specific work, they were utilized due to their convenience since it is possible to alter one arm of the racetrack geometry for specific purposes and used as platforms for loss measurements [66]. Racetrack resonators can also reach high Q-factors such as 10^6, and it is also possible to increase the coupling gap size and the fabrication tolerance by using racetrack resonators [67]. Another advantage that racetrack

resonators have over toroidal or spherical resonators is the two-dimensional geometry that enables them to be used in on-chip applications. Instead of light coupling by using one of the long arms of the racetrack resonator, it is also possible to couple light via the bend. One specific work used this bend directional coupling to selective couple light into their high Q-factor ($> 10^6$) racetrack resonators [68]. Due to their obvious utilization, following the toroidal resonator production, further trials were conducted for racetrack resonators (Figure 4.8).

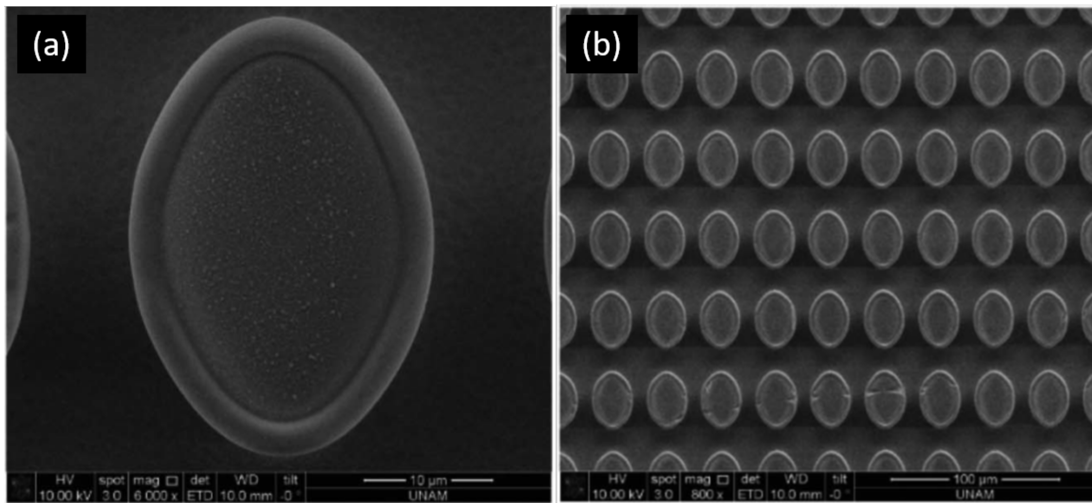

Figure 4.9: Scanning electron microscope images of (a) A single ellipsoid resonator in the array and (b) an array of ellipsoid resonators on a chip.

Elliptical resonators (Figure 4.9) are also another resonator type that is being used for several instances since their deformed symmetrical geometry increases the directionality of both light collection and emission. This fact can be taken advantage of to enhance optical coupling into the resonator and unidirectional light emission from the resonator itself. Recently it was shown that an elliptical optical resonator with a wavelength size notch could be utilized for emitting a highly unidirectional light. The notch acts as a focus of the elliptical resonator, and resonating light from the notch is directed towards the opposite end of the resonator, and through that end, the light is emitted as parallel rays [69]. Although the deviation from the perfect symmetry decreases the Q-factor of the resonator – the more distorted the shape, the lower the Q-factor – this method permits those resonators to be utilized in applications where directed beams are needed. In another work, an elliptical resonator was used for long-range energy

transfer. By utilizing quantum dots (QDs) at each focal point of the elliptical resonator, the plasmonic resonator was shown to enhance the energy transfer between two points [70].

As demonstrated in Figures 4.4, 4.8, and 4.9 , the scanning laser mode approach was used to fabricate toroidal, racetrack and ellipsoid resonators. Even though the approach was only used to produce resonators with only three different geometries, it is possible to use the same technique for other geometries such as polygonial [71] and triangular [72] when they are required.

In conclusion, utilizing the raster scan laser engraver has a great potential to improve the throughput of the toroidal resonator production as well as other STIM resonators due to having obvious advantages over a single reflowing process. It should also be noted that not only throughput is improved, but also batch processing is introduced at the reflowing stage instead of reflowing the resonators one by one. Following the toroidal resonator fabrication with raster scan laser, the fabrication method was also tried for two different geometries; elliptical and racetrack. The method permits the reflow of resonators with elliptical and racetrack geometries allowing the wafer-scale high-Q-factor microresonator arrays. This can lead to better integration of resonators into all-optical circuits. The method is also not limited to the three geometries mentioned above but can be used for other geometries specifically designed to satisfy various requirements. Furthermore, precise control over transferred power by altering the focus and power levels allows much better control of temperature. It is possible to reflow resonators fabricated from different materials that require different reflowing temperatures. Mass fabrication of the resonators in a rapid manner can promote the usage of optical resonators in photonic applications.

Chapter 5

Permanent Shift on Resonant Modes of Chalcogenide Coated Silica Microtoroids

There are various applications of the WGMRs, and one of them is optical modulation. Although fiber optics revolutionized communications by allowing vast amounts of data transfer by light and enhanced the speed of data transfer vastly, the data still needs to be processed by electronic circuits prior to and after the data transfer. The demand for light generation and modulation applications and techniques increased following the growing attention on photonic circuits, especially knowing that the photonic circuits can multiply the speed of data processing done by existing silicon-based electronic circuits. Optical modulators and switches can be realized by using the WGM resonators by utilizing their dependency on the environmental stimuli (such as temperature, pressure, electrical and optical signals, etc.) on the manifested resonant modes. By applying the external stimuli, it is possible to use resonators as optical modulators and switches.

Whispering gallery mode resonators can also be utilized as detectors and sensors by using a similar principle of utilizing external stimuli. Any stimuli that affect the refractive index ratio (between the resonator and the environment)

and/or the morphology of the resonator result in the change of the resonant modes of the resonator. Bio-chemical agents can be detected by using this knowledge, even down to a single molecule from bigger agents. Considering the increased needs of the health industry; in order to detect existing and new pathogens and viruses fast and reliably, water security; to determine whether they are contaminated or not, an optical device that can utilize optical resonators may enhance the abilities of those industries. In addition to those applications, WGMRs are also being used for optomechanics, nonlinear and quantum optics, as well as Raman lasing. Due to the high number of possible applications, intensive research on the subject of optical WGM resonators is being done in order to utilize their light confinement abilities and the photons confined by resonators.

The aforementioned applications rely on the light confinement feature of the resonators, their manifested resonant modes, and the tuneability of these modes. These modes can be altered by external stimuli, and by doing so, the resonators can be used as detectors and sensors to detect the changes in environmental parameters. The external stimuli can be mechanical, thermal, optical, biological, or chemical agents.

In order to obtain optical resonators with tuneable modes, several approaches were proposed. An electro-optic modulation was reported by utilizing silicon microspheres. By applying a potential difference, a silicon resonator was stimulated, and its refractive index was changed. As a result of this change in the refractive index, a mode shift was demonstrated [12]. In another work, lithium niobate (LN) resonators were utilized to demonstrate mode shift when subjected to electrical stimuli. A potential difference was applied to resonators and achieved a shift in the resonant mode spectrum due to the electro-optic properties of the lithium niobate [73]. It is also possible to utilize the thermo-optic effect in order to achieve a shift in the resonant mode spectrum. One reported approach used nematic liquid crystals utilizing their thermo-optic properties in order to get optical response under thermal stimuli. A shift in the resonant modes was demonstrated under thermal stimuli [74]. In another work, optically trapped droplet resonators formed by liquid crystals were used in order to achieve a shift in the mode spectrum. By altering the temperature, the phase of the liquid crystals

was changed, and this phase change initiated the mode shift [75]. Polymer-based microresonators were utilized in another reported work. A polymethyl methacrylate (PMMA) has a negative thermo-optic coefficient, and a hollow optical fiber made from PMMA was used to achieve a shift in resonant mode spectrum under thermal stimuli [76].

From the previous reports, it is clear that it is possible to modify and modulate the resonant modes in a facile and reversible way. Although, as soon as the stimulus that affects the resonant modes is removed, the change in the resonant modes is reversed. As mentioned before, one of the setbacks for the wide-scale utilization of the WGMRs in optical devices and methods is that the errors during the fabrication process of the WGMRs lead to deviance from the designed parameters, such as the radius and the roughness of the resonators. Any small variance from the desired radius value causes a shift in manifested resonant modes during optical coupling, thus hindering their implementation for applications. Since it would not be practical to alter the radius following fabrication, the only way to tune the resonant modes is to change the refractive index. Therefore, instead of a temporary shift in the resonant modes, the aim is to alter the modes permanently. Suppose a method can be provided to change the resonant modes of resonator post-production permanently. In that case, this can potentially be used to alter the resonator's modes in a controllable and irreversible way. This may provide a possible means for overcoming another problem hindering the commercialization of optical resonators.

5.1 Chalcogenides

Due to their wide mid-IR transparency, low-phonon energy, and high nonlinearity [77, 78], chalcogenides are commonly utilized for a variety of photonics applications such as color-switching and IR spectroscopy [79, 80, 81]. Due to the photosensitive nature of the chalcogenides [77], light exposure induces phase changes within the structure of the chalcogenide material in the exposed area.

This alteration in the structure of the material leads to a change in the optical properties of the material. Therefore, being one of the optical properties, the refractive index of the material is modified within the light-exposed region. Absorption is also another affected optical property, and due to this change in the absorption, this process of altering the phase of chalcogenide is also referred photodarkening.

It is possible to induce crystallization, a phase change in the structure, on chalcogenide films by utilizing a laser. It was demonstrated that an amorphous $Ge_2Sb_2Te_5$ (GST) film was exposed to laser light, and crystallization was induced as a result [82]. It was demonstrated photoinduced refractive index change in the arsenic selenide (As_2Se_3) fibers [83], and arsenic sulfide (As_2S_3) microfibers [84]. Localized WGM microresonators were produced by exploiting the photosensitive nature of chalcogenide material. Arsenic selenide microfibers were subjected to laser light, and by inducing the phase change, a localized optical resonator was produced [84]. A similar approach was reported in the tuning of resonant modes of a photonic crystal as well. By exposing the photonic crystal (PC) to laser light, the refractive index of the PC was modified [85].

So, chalcogenide's photosensitive nature can be utilized in order to induce a phase change in its structure if exposed to optical stimuli. It is also possible to use the material itself to fabricate optical resonators. Here, we proposed that silica toroidal microresonators can be coated with a thin chalcogenide layer, and this layer can be utilized to permanently tune the resonant modes of the resonator. $Ge_2Sb_2Te_5$ (GST) is chosen as the coating material to be coated onto the silica microtoroids fabricated in our previous works.

5.2 Fabrication of Chalcogenide Coated Silica Resonators

For this work, a 500 µm thick silicon wafer with a 2.5 µm thermally grown oxide layer on top was purchased from Addison Engineering. Toroidal resonators were fabricated by combining the microfabrication steps detailed in Chapter 2 and reflowing step by raster scanning method demonstrated in Chapter 4. The fabrication steps are detailed in Figure 5.1.

Initially, the wafer was diced into rectangular pieces of 20x30 mm substrates. Each of these substrates (Figure 5.1a) was stored to be used in fabrication batches. In each fabrication batch, an array of resonators were fabricated on top of each substrate. The second step is spin-coat the substrate with the hexamethyldisilazane (HMDS purchased from Merck) (Figure 5.1b) in order to enhance the bonding process between the silica and the photoresist, which is to be used later for photolithography. Following the coating of the substrate with HMDS, the substrate was spin-coated with (Merck) AZ4533 photoresist (Figure 5.1c). The substrate, then, was patterned by using photolithography. The substrate that was patterned with lithography (Figure 5.1d) was then immersed into a (Merck) AZ400K chemical in order to develop the patterned photoresist (Figure 5.1e). The developing step left disk-shaped photoresist-coated regions on top of the silica. Then the substrate was wet-etched by using Buffer Oxide Etchant (BOE 7:1). The regions under the disk-shaped regions were protected while the rest was etched completely (Figure 5.1f). This step left disk silica layers on top of the silicon, and following the silica etching, the substrate was placed into the Inductively Coupled Plasma (ICP) and underwent the silicon etching process. As a result of this isotropic silicon etching, silica disks on silicon pillars were formed on top of the substrate (Figure 5.1g).

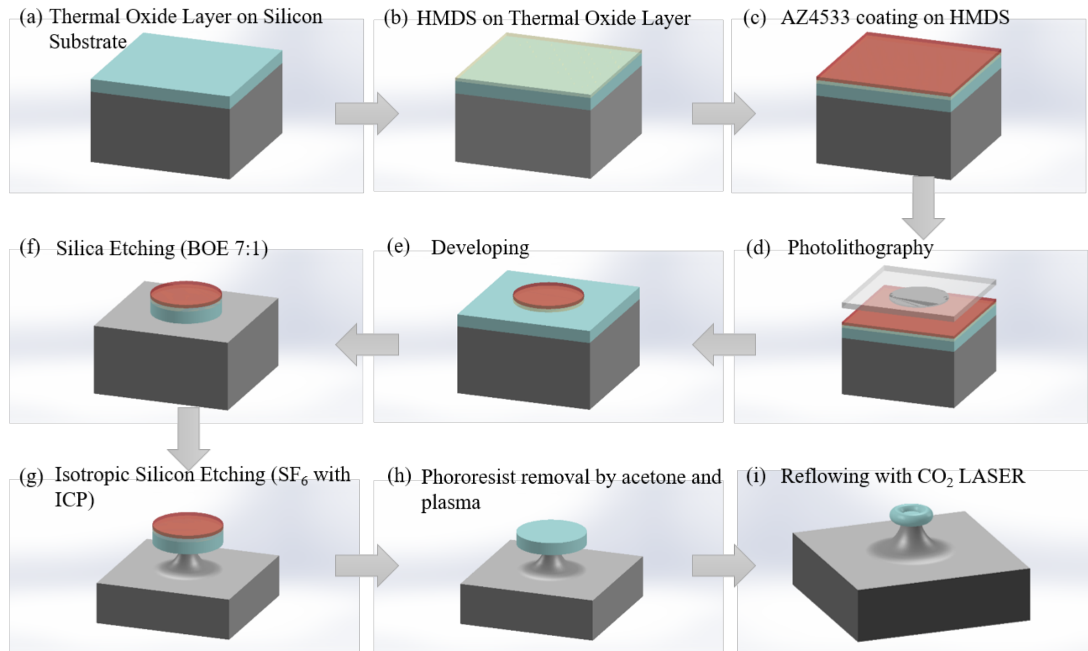

Figure 5.1: Silica microtoroid fabrication procedure from wafer to a toroidal resonator. (a) 20x30mm rectangular substrates diced from the wafer. (b) HMDS coating (yellow color) onto the substrate to enhance the bonding between the oxide layer (blue color) and photoresist. (c) Photoresist coating (red color) onto the substrate. (d) A designed mask with patterns on it is used to pattern the substrate by using photolithography. (e) The photoresist developing process is done in order to harden the photoresist to allow patterns on the substrate. (f) By using buffer oxide etchant (BOE 7:1), silica etching is done. The area under photoresist patterns is protected while the rest is etched. (g) Silicon etching is done after silica etching. The area under the silica undergoes isotropic etching to form a pillar while the rest is etched completely. (h) The photoresist is removed from the structure since there is no need for it anymore. (i) Silica microdisks on silicon pillars produced as a result of microfabrication are reflowed by using a CO_2 laser engraver.

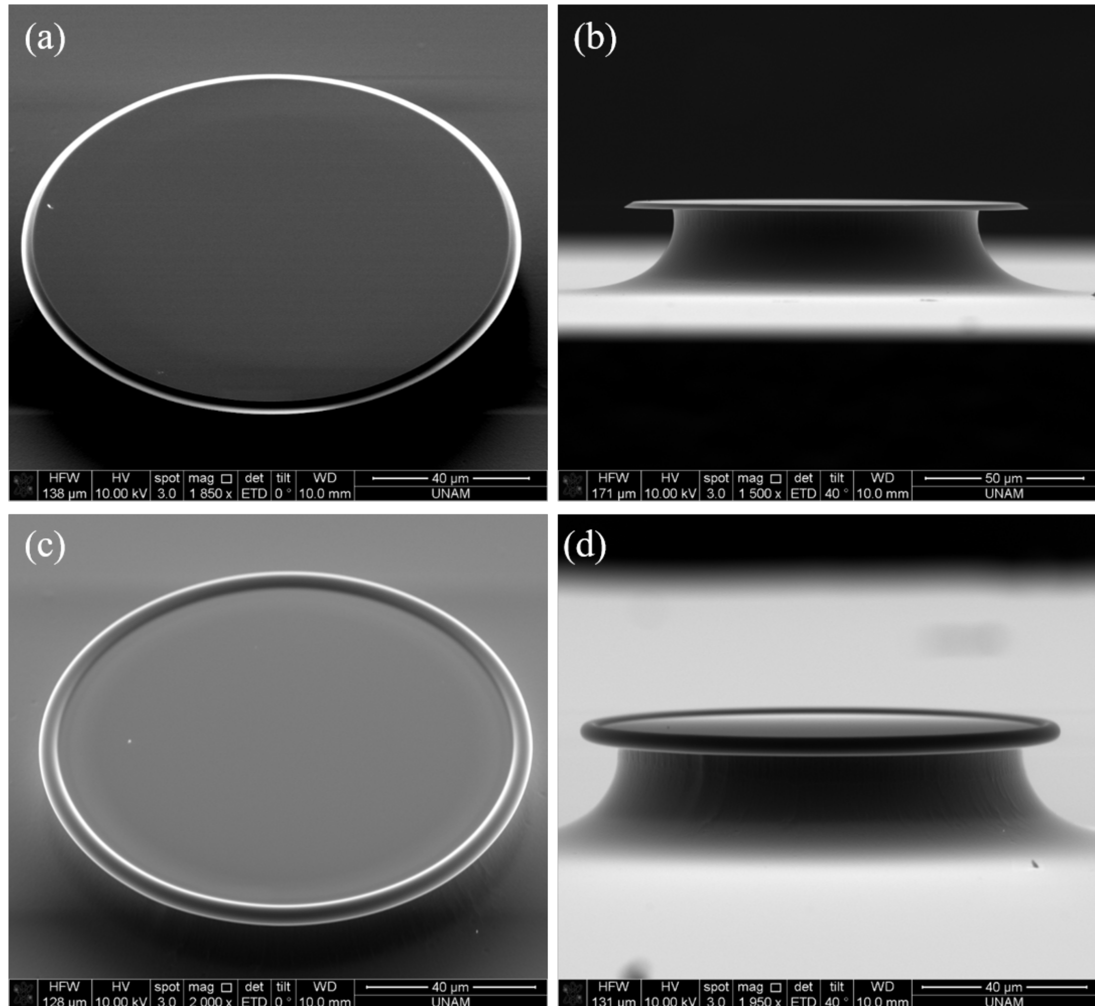

Figure 5.2: (a) Tilted view and (b) side view of a fabricated silica disk resonator taken by SEM. (c) Tilted view and (d) side view of a fabricated silica toroidal resonator.

The remaining photoresist and chemicals were removed from the substrate by using acetone, IPA chemicals, and plasma asher (Figure 5.1h). After microfabrication, an array of silica microdisk resonators were formed on the substrate, and in order to reshape them into toroidal resonators, they were reflowed by using a CO2 laser (Figure 5.1i). The silica microtoroid resonator was fabricated as a result of microfabrication, is shown in Figure 5.2.

Following the fabrication of the silica microtoroid array on the substrate, a thin GST layer is required to be coated onto it. In order to coat GST onto the substrates, the sputtering technique was used (Figure 5.3). Two sets of resonator arrays were produced, one coated with a 5 nm layer while the second one was coated with a 10 nm layer.

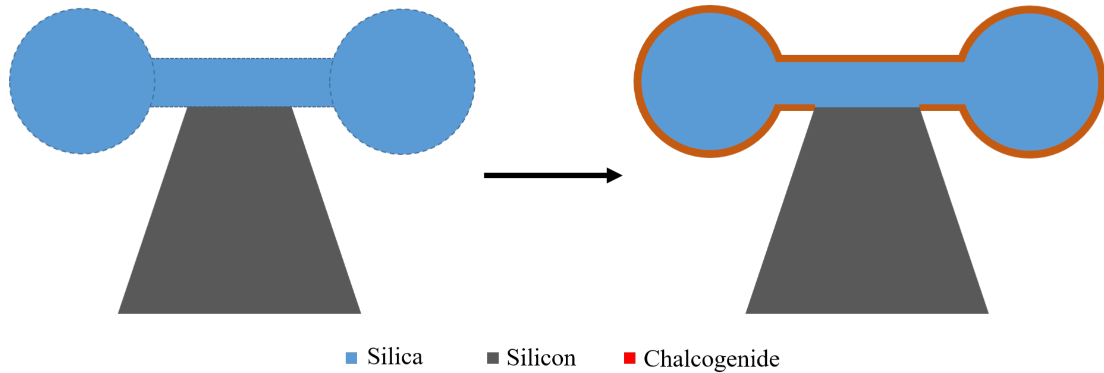

Figure 5.3: GST chalcogenide layer coated onto the microtoroid arrays on the substrate, creating a layer on the silica microtoroids.

In order to experiment on the fabricated resonators, silica optical fiber was tapered for the light coupling. ThorLabs SMF-28 single-mode silica fiber was used in this study. The tapering process was done as detailed in Chapter 3. One end of the optical fiber was connected to the diode laser, while the other end was plugged into the photodetector connected to the power meter. The polymer coating of the fiber was stripped from a small region of 2 cm, and the fiber was placed onto two fiber holders that left the stripped region in between those holders. The holders were fixed to two piezoelectric stages at the opposite ends and controlled by a motion controller. Then the fiber was pulled in opposite directions while a hydrogen torch flame was heating up the silica fiber. Following the adiabatic tapering process, ensured by sufficient heating, slow pulling speed, and constant visual monitoring via a CCD camera system, tapered fiber was fixed to be used for optical coupling.

5.3 Permanent Mode Tuning

A three-axis piezoelectric stage (Thorlabs Nanomax-TS stage with Thorlabs BPC303 Controller) was placed between the translational stages in close proximity to the tapered region of the silica fiber. The substrate with an array of silica microtoroids coated with a 5 nm GST layer was fixed onto the three-axis stage. The diode laser was switched on, and a wavelength scan between 1510-1620 nm was initiated. While the laser is sweeping between the start and stop wavelengths, 1510 nm and 1620 nm, respectively, the transmission was monitored and recorded by an oscilloscope that was gathering data from the power meter that was connected to the photodetector.

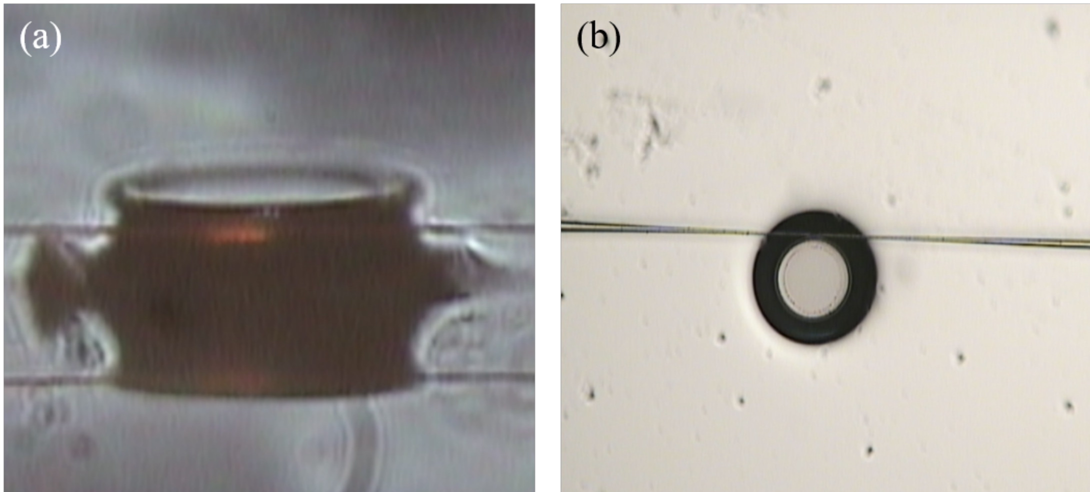

Figure 5.4: Optical images of a microtoroid coupled to a tapered silica fiber. (a) Side view of the resonator. (b) Top view of the resonator.

The GST-coated silica microtoroid was moved in close proximity to the tapered fiber while the transmission was monitored. When dips appeared in the transmission spectrum at specific wavelengths, stage movement was stopped. One specific transmission dip was selected, and a new sweeping range was set to the diode laser in order to cover only that specific transmission dip. The position of the resonator, then, was arranged in fine-tuning mode to maximize the coupling, and after reaching the lowest possible transmission dip, the stage position was fixed (Figure 5.4).

The Q-factor of resonators was investigated at first in order to see the effect of the chalcogenide coating on the Q-factor. Our toroidal silica microresonator fabrication process resulted in resonators with high-Q-factors at the order of 10^6. Initially, one silica microtoroid was selected from the batch and coupled to the tapered fiber. The Q-factor of that resonator was measured as 2.7 x 10^6 (Figure 5.5a). The resonator was then coated with a 5 nm thick GST layer. Following the coating, the resonator was coupled to the tapered fiber again. Q-factor post-coating was calculated as 2.1 x 10^5 (Figure 5.5c).

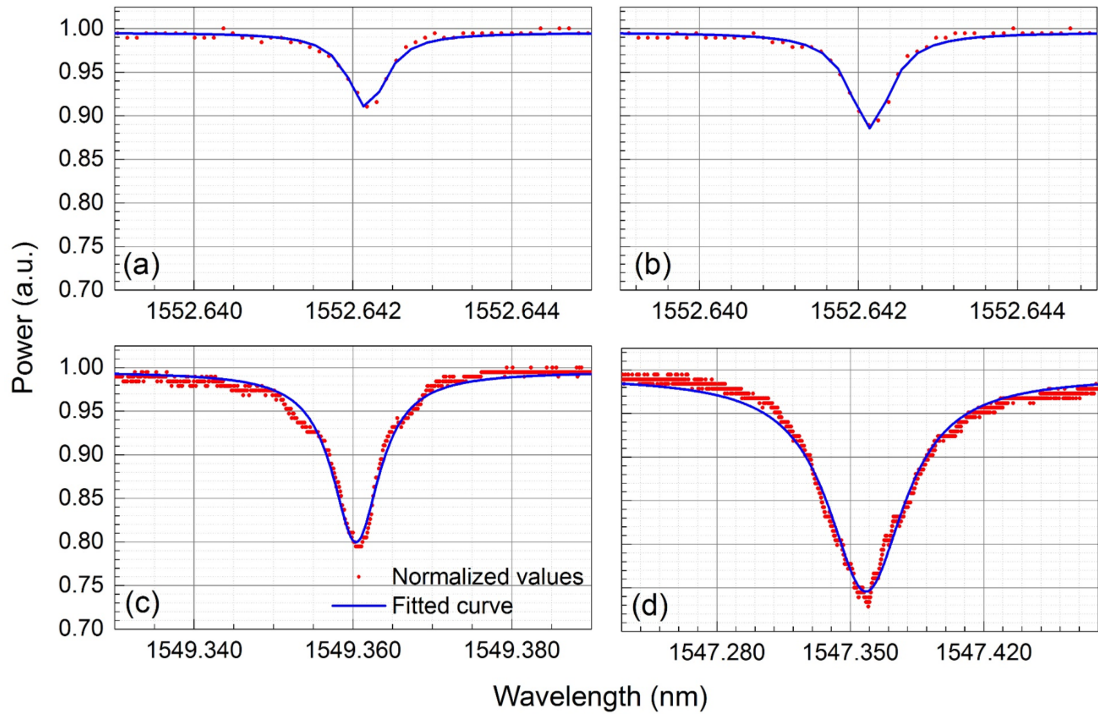

Figure 5.5: (a) Resonant mode of a bare silica microtoroid within the first batch prior to GST coating. (b) Resonant mode of a 5 nm coated resonator. (c) Resonant mode of a bare silica microtoroid within the second batch prior to GST coating. (d) Resonant mode of a 10 nm coated resonator.

Similar to the first Q-factor investigation, a microtoroid was selected from the second batch, and then optical characterization was done prior to the GST layer coating. The Q-factor of the bare silica microtoroid was measured as 2.5 x 10^6 (Fig 5.5b). After the coating step, the Q-factor of the 10 nm coated resonator was down to 3.2 x 10^4 (Fig 5.5d). This drop in the Q-factor was expected. The

reflowing process makes smoother surfaces that permit STIMs to have better Q-factors. However, the coating step introduced additional surface roughness to the resonator surface. Therefore, the coating caused an order of magnitude drop in Q-factor in the 5 nm coated sample, while it caused two orders of magnitude drop for the 10 nm coated sample.

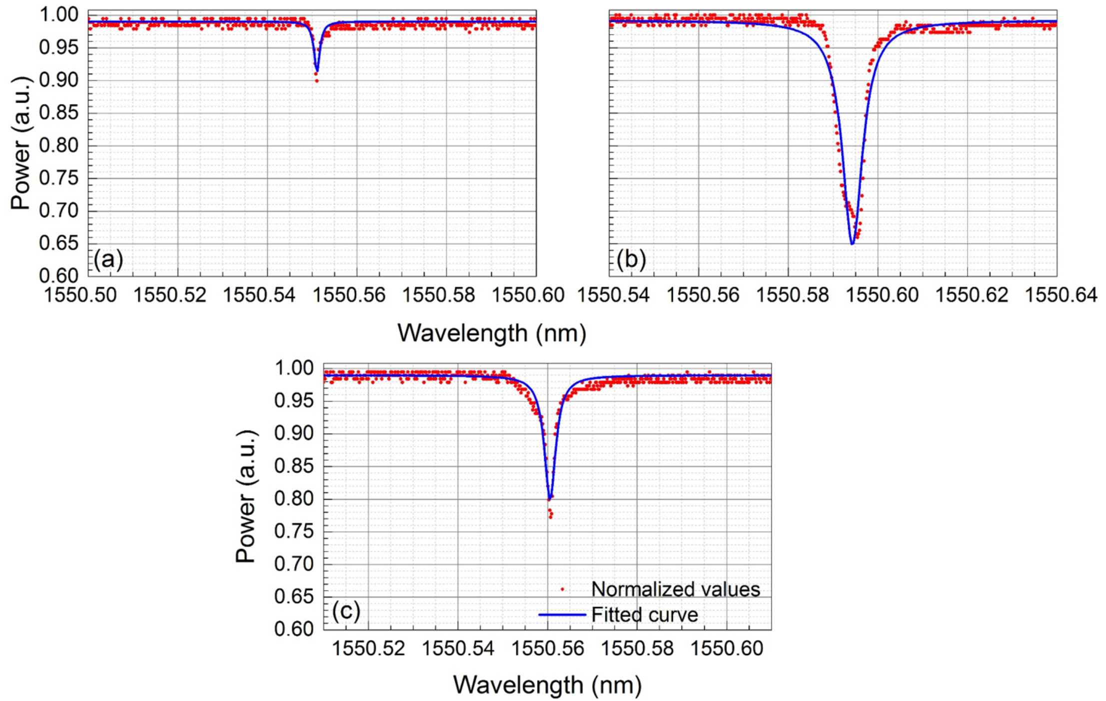

Figure 5.6: Permanent tuning of a resonant mode of 5 nm GST-coated Silica microtoroid. The transmission spectrum of the mode (a) prior to laser illumination, (b) during the laser illumination, and (c) after the laser illumination.

A silica microtoroid with a 5 nm GST layer was coupled to the tapered fiber. A resonant mode was selected, and then the diode laser was switched on. A new custom-made laser (with an emission wavelength of 450 nm) was aligned and focused on top of the GST-coated silica microtoroid. While the diode laser was sweeping between the wavelength range covering the resonant mode, the custom-made laser was switched on, and the resonator was exposed to laser light for 30 seconds. During this time period, the transmission spectrum was recorded. Following 30 seconds, the custom-made laser was switched off, and the transmission spectrum was recorded after the laser exposure. The transmission spectrum data were analyzed, and three transmission spectra graphs were plotted (Figure 5.6).

Figure 5.6a shows the initial transmission spectrum of the resonator at the selected resonant mode. This spectrum shows the resonant mode prior to exposure to the laser illumination. During the laser illumination, a clear red shift of the resonant mode was shown in Figure 5.6b. This red shift was the result of two different mechanisms. The first one is the phase change caused by the photodarkening process. The second mechanism that caused the shift is the change due to the temperature increase on the resonator because of the laser heating. The temperature increase caused thermal expansion that led to an increase in the resonator diameter. The resonant mode of a resonator depends on the optical path length of the light, which is affected by the diameter and the refractive index of the resonator. The diameter change of the resonator led to a change in the optical path, and this change manifested itself as a shift in the resonant mode. When the laser illumination ceased, laser heating would not contribute to the mode shift. The third spectrum (Figure 5.6c) shows the resonant mode at the end of the photodarkening process after 30 seconds of laser exposure. As expected, a blue shift occurred with respect to the second spectrum since laser heating was stopped. However, there is still a shift in comparison to the initial spectrum. This shift indicated a permanent shift in the resonant mode due to the photodarkening process. The GST layer underwent a phase change induced by light illumination, and as a result, 0.1 pm permanent tuning was demonstrated for the 5 nm GST-coated silica microtoroid.

Similarly, Figure 5.7 shows the results for the 10 nm GST-coated silica microtoroid for the same conditions applied to the 5 nm sample. An initial transmission spectrum of a resonant mode was recorded and shown in Figure 5.7a. When the coated resonator was illuminated by the custom-made laser, a clear shift was recorded during the illumination period. The shift in the resonant mode during the laser exposure is shown in Figure 5.7b. Finally, Figure 5.7c shows the transmission spectrum after the photodarkening. As expected, the same temperature-dependent change in the resonant mode was observed as a result of laser heating. Following the photodarkening process, a permanent shift of 0.2 pm in the resonant mode of the 10 nm coated sample was demonstrated.

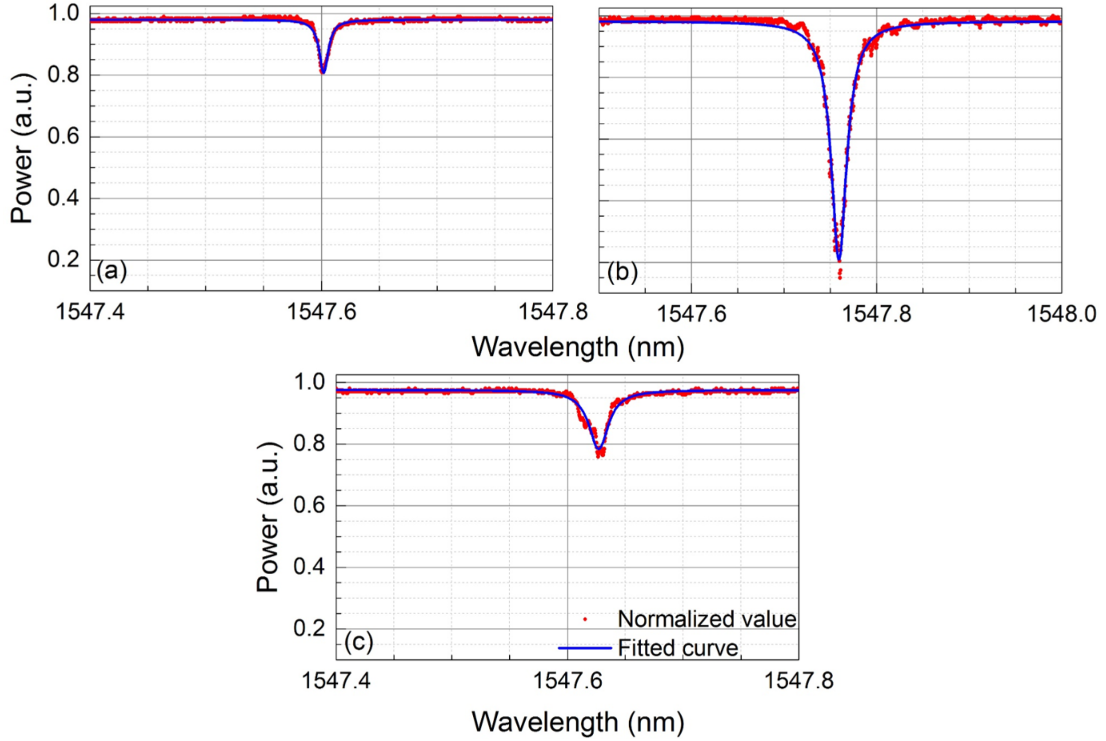

Figure 5.7: Permanent tuning of a resonant mode of 10 nm GST-coated Silica microtoroid. The transmission spectrum of the mode (a) prior to laser illumination, (b) during the laser illumination, and (c) after the laser illumination.

In both cases, distinguishable changes in the transmission dip were observed during the laser illumination step (Figures 5.6b and 5.7b). The transmission was reduced greatly as well as the mode shift. This decrease in transmission is related to laser heating as well. Due to the laser heating, the diameters of the resonators were increased; therefore, the distance between the resonator and the tapered fiber was decreased. The narrower coupling distance led to better coupling efficiency, which was clearly not achieved prior to the photodarkening procedure.

As a result, silica microtoroids were fabricated with the combination of silicon microfabrication and reflowing techniques, and later, $Ge_2Sb_2Te_5$ was deposited onto the resonator arrays on the silicon substrates. This chalcogenide layer was then utilized in order to achieve photoinduced phase change in the GST in order

to permanently tune the resonant modes of the resonators. During the photodarkening process, resonant modes of the coated samples were shifted due to both the photoinduced phase change in the GST and the thermal expansion of the resonator caused by the laser heating. The permanent changes caused after the photodarkening were 0.1 nm and 0.2 nm for 5 nm and 10 nm coated samples, respectively.

The thickness of the coating layer, duration of the exposure, and the area subjected to laser exposure contribute to the total permanent mode shift of the resonator. Even though the experiments were done for two different coating thicknesses, thicker layers are expected to have larger shifts. The large the area exposed, the large the index change is expected. Similarly, a larger shift can be expected for the longer duration of exposure. This method was demonstrated to alter the resonant modes of WGMRs in a permanent manner.

Since only $Ge_2Sb_2Te_5$ was utilized as a coating layer, the modification of the optical modes was limited with the red shift corresponding to an increase in the resonant wavelength. Both positive and negative tuning was reported for chalcogenide material [86], so for further research, more materials may be explored for coating. Once a comprehensive chart is deduced from a set of different materials and phase change conditions, it may be possible to use this method in order to fine-tune the optical resonant modes of resonators with different geometries permanently. Tuning the resonant modes can be used to compensate for inherited fabrication errors that led to deviations in the resonant mode spectrum.

Chapter 6

Conclusions

Whispering gallery mode resonators, with their optical properties and utilization, allow a variety of possibilities for photonics research and industry. A high q-factor WGM resonator enhances the light-matter interaction when the light is coupled, and this can be used to improve the nonlinear optical phenomena that generally require high optical intensity. WGM resonators can be used as optical modulators and filters. They can also be employed as detectors with high sensitivity to detect biological and chemical agents since the enhanced light-matter interaction emphasizes the changes in the environment. Any change – due to a biological or chemical agent – manifests itself as a distinguishable resonance shift. Depending on the utilization method of the resonator, it is possible to develop a sensor that can detect down to a single molecule and even differentiate specific agents via functionalization.

Due to the choice of using toroidal resonators in experiments, it was the logical choice to select tapered optical fiber as an efficient light coupling method. Evanescent field coupling by using tapered fiber is a good method due to its high coupling efficiency. A homemade setup was designed and built to taper the optical fiber with a carbon-dioxide laser. Even though it was successful, the carbon dioxide laser's power stability was problematic, which led to limitations

in the process' repeatability and throughput. The carbon-dioxide laser was replaced by a hydrogen torch for practical reasons. It was cost-effective and fast to align. Tapering was achieved much more reliable afterward with this method. The method allowed us to taper fibers with high transmission (approx. 80%) and sub-wavelength diameters (approx. 1.0 µm).

Even though having clear advantages, the utilization of WGM resonators is not widespread at the current moment. This is because their usage is mostly hindered due to several limitations. First of all, it is not an easy task to mass-produce optical resonators, especially resonators that require heat-induced reflowing such as toroidal resonators. Toroidal resonators have high q-factors and low mod volumes, which make them great candidates for photonics research and applications. However, their fabrication method, which involves clean room fabrication and then reflowing process, is not easy. In order to make the mass production of toroidal resonators easier, a new technique is presented in this thesis. Instead of a carbon-dioxide laser with fixed alignment, which is generally used to reflow process for toroidal resonators, a raster scanning carbon-dioxide laser was utilized. Toroidal resonators on a single chip with high q-factors (10^5-10^6) were fabricated by using this technique [87]. Toroidal resonators with q-factors of 10^5-10^6 are not the state-of-the-art level; however, in this work, the primary aim was to be able to decrease the reflowing time of the high number of resonators. Reflowing of resonators with different geometry types was achieved by this method. Reflowing was optimized by tuning the combination of the focus, scan speed, and power of the laser. Resonators with different geometrical types (disk, racetrack, elliptical) were fabricated on substrates, and each substrate included a high number of resonators on the order of 100. This approach provides a fast and high throughput method for the reflowing process that can be used easily. Since this method was demonstrated on various geometries without problem, complementary work can be done if this method is to be used on on-chip resonators with a built-in waveguide. It is possible to fabricate a disk resonator with a waveguide in close proximity within the limits of photolithography. By designing a geometry that allows the distance between resonator and waveguide stays the same at some degree, raster scanning can be used to reflow both the waveguide and resonator

or separately depending on the beam waist of the laser. Further research can be done to optimize the raster scanning to tune the coupling distance as well.

Also, a method for permanently tuning the resonant modes of a resonator was demonstrated. $Ge_2Sb_2Te_5$ (GST) is a photosensitive material that undergoes a change in its structure when subjected to light within a specific wavelength range. The change in the structure leads to a permanent change in the refractive index. Therefore, by using this photodarkening process, it is possible to permanently change the resonant modes of a GST-coated resonator. A thin GST layer was coated onto the resonators following their fabrication and reflowing. This additional thin layer provides means to alter the refractive index of the resonator after the production. In our experiments, permanent mode tuning of 0.01 nm and 0.02 nm were successfully demonstrated for resonators coated with 5 nm and 10 nm GST layers, respectively [88]. For further research, it is possible to coat the resonators with other photosensitive materials in order to analyze their response to stimuli. By mapping out different responses from different materials and for different photodarkening parameters, a more comprehensive picture can be gathered to utilize for permanent mode tuning of resonators. It may be possible to use this method for fine-tuning the resonant modes of a fabricated resonator and, by doing so, rectifying the deviations in the resonant mode spectrum resulting from fabrication errors.

Bibliography

[1] L. Rayleigh, "The problem of the whispering gallery," *Philosophical Magazine Series 1*, vol. 20, pp. 1001–1004, 1910.

[2] A. Beiser, *Concepts of Modern Physics (SIE)*. McGraw-Hill Education, 1963.

[3] B. E. Saleh and M. C. Teich, *Fundamentals of Photonics*. John Wiley & Sons, 2019.

[4] K. J. Vahala, "Optical microcavities," *Nature*, vol. 424, no. 6950, pp. 839–846, 2003.

[5] F. Vollmer, S. Arnold, and D. Keng, "Single virus detection from the reactive shift of a whispering-gallery mode," *Proceedings of the National Academy of Sciences*, vol. 105, no. 52, pp. 20701–20704, 2008.

[6] L. He, Ş. K. Özdemir, J. Zhu, W. Kim, and L. Yang, "Detecting single viruses and nanoparticles using whispering gallery microlasers," *Nature Nanotechnology*, vol. 6, no. 7, pp. 428–432, 2011.

[7] Y. Zhi, X.-C. Yu, Q. Gong, L. Yang, and Y.-F. Xiao, "Single nanoparticle detection using optical microcavities," *Advanced Materials*, vol. 29, no. 12, p. 1604920, 2017.

[8] X.-C. Yu, S.-J. Tang, W. Liu, Y. Xu, Q. Gong, Y.-L. Chen, and Y.-F. Xiao, "Single-molecule optofluidic microsensor with interface whispering gallery modes," *Proceedings of the National Academy of Sciences*, vol. 119, no. 6, p. e2108678119, 2022.

[9] M. S. Luchansky and R. C. Bailey, "High-q optical sensors for chemical and biological analysis," *Analytical Chemistry*, vol. 84, no. 2, pp. 793–821, 2012.

[10] A. M. Armani, R. P. Kulkarni, S. E. Fraser, R. C. Flagan, and K. J. Vahala, "Label-free, single-molecule detection with optical microcavities," *Science*, vol. 317, no. 5839, pp. 783–787, 2007.

[11] H. K. Hunt and A. M. Armani, "Label-free biological and chemical sensors," *Nanoscale*, vol. 2, no. 9, pp. 1544–1559, 2010.

[12] E. Yuce, O. Gurlu, and A. Serpenguzel, "Optical modulation with silicon microspheres," *IEEE Photonics Technology Letters*, vol. 21, no. 20, pp. 1481–1483, 2009.

[13] I. Kiyat, A. Aydinli, and N. Dagli, "Low-power thermooptical tuning of soi resonator switch," *IEEE Photonics Technology Letters*, vol. 18, no. 2, pp. 364–366, 2006.

[14] L. Zhou and A. W. Poon, "Silicon electro-optic modulators using pin diodes embedded 10-micron-diameter microdisk resonators," *Optics Express*, vol. 14, no. 15, pp. 6851–6857, 2006.

[15] S. Gulde, A. Jebali, and N. Moll, "Optimization of ultrafast all-optical resonator switching," *Optics Express*, vol. 13, no. 23, pp. 9502–9515, 2005.

[16] V. Sandoghdar, F. Treussart, J. Hare, V. Lefevre-Seguin, J.-M. Raimond, and S. Haroche, "Very low threshold whispering-gallery-mode microsphere laser," *Physical Review A*, vol. 54, no. 3, p. R1777, 1996.

[17] O. Boyraz and B. Jalali, "Demonstration of a silicon raman laser," *Optics Express*, vol. 12, no. 21, pp. 5269–5273, 2004.

[18] S. B. Gorajoobi, G. S. Murugan, and M. N. Zervas, "Design of rare-earth-doped microbottle lasers," *Optics Express*, vol. 26, no. 20, pp. 26339–26354, 2018.

[19] J. R. Ong and S. Mookherjea, "Quantum light generation on a silicon chip using waveguides and resonators," *Optics Express*, vol. 21, no. 4, pp. 5171–5181, 2013.

[20] B. J. Hausmann, I. Bulu, P. Deotare, M. McCutcheon, V. Venkataraman, M. Markham, D. Twitchen, and M. Loncar, "Integrated high-quality factor optical resonators in diamond," *Nano Letters*, vol. 13, no. 5, pp. 1898–1902, 2013.

[21] T. J. Kippenberg, R. Holzwarth, and S. A. Diddams, "Microresonator-based optical frequency combs," *Science*, vol. 332, no. 6029, pp. 555–559, 2011.

[22] J. Richard, J. Hamilton, and Y. Pang, "Fabry-perot optical resonator at low temperatures," *Journal of Low Temperature Physics*, vol. 81, no. 3, pp. 189–198, 1990.

[23] J. M. Vaughan, *The Fabry–Perot interferometer: history, theory, practice and applications*. Routledge, 2017.

[24] S. McCall, A. Levi, R. Slusher, S. Pearton, and R. Logan, "Whispering-gallery mode microdisk lasers," *Applied Physics Letters*, vol. 60, no. 3, pp. 289–291, 1992.

[25] B. Gayral, J. Gérard, A. Lemaıtre, C. Dupuis, L. Manin, and J. Pelouard, "High-q wet-etched gaas microdisks containing inas quantum boxes," *Applied Physics Letters*, vol. 75, no. 13, pp. 1908–1910, 1999.

[26] D. S. Gardner and M. L. Brongersma, "Microring and microdisk optical resonators using silicon nanocrystals and erbium prepared using silicon technology," *Optical Materials*, vol. 27, no. 5, pp. 804–811, 2005.

[27] X. Lu, J. Y. Lee, P. X.-L. Feng, and Q. Lin, "Silicon carbide microdisk resonator," *Optics Letters*, vol. 38, no. 8, pp. 1304–1306, 2013.

[28] X. Lu, J. Y. Lee, P. X.-L. Feng, and Q. Lin, "High q silicon carbide microdisk resonator," *Applied Physics Letters*, vol. 104, no. 18, p. 181103, 2014.

[29] J. Zhang, R. Wu, M. Wang, Y. Liang, J. Zhou, M. Wu, Z. Fang, W. Chu, and Y. Cheng, "An ultra-high-q lithium niobate microresonator integrated with a silicon nitride waveguide in the vertical configuration for evanescent light coupling," *Micromachines*, vol. 12, no. 3, p. 235, 2021.

[30] M. Sumetsky, "Optimization of optical ring resonator devices for sensing applications," *Optics Letters*, vol. 32, no. 17, pp. 2577–2579, 2007.

[31] S. I. Shopova, Y. Sun, A. Rosenberger, and X. Fan, "Highly sensitive tuning of coupled optical ring resonators by microfluidics," *Microfluidics and Nanofluidics*, vol. 6, no. 3, pp. 425–429, 2009.

[32] O. Aktas, E. Ozgur, O. Tobail, M. Kanik, E. Huseyinoglu, and M. Bayindir, "A new route for fabricating on-chip chalcogenide microcavity resonator arrays," *Advanced Optical Materials*, vol. 2, no. 7, pp. 618–625, 2014.

[33] D. Armani, T. Kippenberg, S. Spillane, and K. Vahala, "Ultra-high-q toroid microcavity on a chip," *Nature*, vol. 421, no. 6926, pp. 925–928, 2003.

[34] A. Polman, B. Min, J. Kalkman, T. Kippenberg, and K. Vahala, "Ultralow-threshold erbium-implanted toroidal microlaser on silicon," *Applied Physics Letters*, vol. 84, no. 7, pp. 1037–1039, 2004.

[35] E. Ozgur, P. Toren, O. Aktas, E. Huseyinoglu, and M. Bayindir, "Label-free biosensing with high selectivity in complex media using microtoroidal optical resonators," *Scientific Reports*, vol. 5, no. 1, pp. 1–9, 2015.

[36] S. Serajmohammadi, H. Alipour-Banaei, and F. Mehdizadeh, "All optical decoder switch based on photonic crystal ring resonators," *Optical and Quantum Electronics*, vol. 47, no. 5, pp. 1109–1115, 2015.

[37] M. Seifouri, V. Fallahi, and S. Olyaee, "Ultra-high-q optical filter based on photonic crystal ring resonator," *Photonic Network Communications*, vol. 35, no. 2, pp. 225–230, 2018.

[38] Y. Zhang, C. Zeng, D. Li, G. Gao, Z. Huang, J. Yu, and J. Xia, "High-quality-factor photonic crystal ring resonator," *Optics Letters*, vol. 39, no. 5, pp. 1282–1285, 2014.

[39] G. Mie, "Beiträge zur optik trüber medien, speziell kolloidaler metallösungen," *Annalen der Physik*, vol. 330, no. 3, pp. 377–445, 1908.

[40] P. Debye, "Der lichtdruck auf kugeln von beliebigem material," *Annalen der Physik*, vol. 335, no. 11, pp. 57–136, 1909.

[41] R. D. Richtmyer, "Dielectric resonators," *Journal of Applied Physics*, vol. 10, no. 6, pp. 391–398, 1939.

[42] M. Gastine, L. Courtois, and J. Dormann, "Electromagnetic resonances of free dielectric spheres," *IEEE Transactions on Microwave Theory and Techniques*, vol. 15, no. 12, pp. 694–700, 1967.

[43] E. Hecht, "Optics 4ed," 2002.

[44] A. N. Oraevsky, "Whispering-gallery waves," *Quantum Electronics*, vol. 32, pp. 377–400, may 2002.

[45] A. Serpengüzel, G. Griffel, and S. Arnold, "Excitation of resonances of microspheres on an optical fiber," *Optics Letters*, vol. 20, no. 7, pp. 654–656, 1995.

[46] G. Griffel, S. Arnold, D. Taskent, A. Serpengüzel, J. Connolly, and N. Morris, "Morphology-dependent resonances of a microsphere–optical fiber system," *Optics Letters*, vol. 21, pp. 695–697, May 1996.

[47] N. Dubreuil, J. C. Knight, D. K. Leventhal, V. Sandoghdar, J. Hare, and V. Lefèvre, "Eroded monomode optical fiber for whispering-gallery mode excitation in fused-silica microspheres," *Optics Letters*, vol. 20, no. 8, pp. 813–815, 1995.

[48] D. W. Vogt, A. H. Jones, H. G. L. Schwefel, and R. Leonhardt, "Prism coupling of high-Q terahertz whispering-gallery-modes over two octaves from 02 THz to 11 THz," *Optics Express*, vol. 26, no. 24, pp. 31190–31198, 2018.

[49] V. B. Braginsky, M. L. Gorodetsky, and V. S. Ilchenko, "Quality-factor and nonlinear properties of optical whispering-gallery modes," *Physics Letters A*, vol. 137, no. 7-8, pp. 393–397, 1989.

[50] T. Ling and L. J. Guo, "A unique resonance mode observed in a prism-coupled micro-tube resonator sensor with superior index sensitivity," *Optics Express*, vol. 15, no. 25, pp. 17424–17432, 2007.

[51] D. W. Vogt, A. H. Jones, and R. Leonhardt, "Free-space coupling to symmetric high-q terahertz whispering-gallery mode resonators," *Optics Letters*, vol. 44, no. 9, pp. 2220–2223, 2019.

[52] J. Zhu, Ş. K. Özdemir, H. Yilmaz, B. Peng, M. Dong, M. Tomes, T. Carmon, and L. Yang, "Interfacing whispering-gallery microresonators and free space light with cavity enhanced rayleigh scattering," *Scientific Reports*, vol. 4, no. 1, pp. 1–7, 2014.

[53] N. Gaber, M. Malak, X. Yuan, K. N. Nguyen, P. Basset, E. Richalot, D. Angelescu, and T. Bourouina, "On the free-space gaussian beam coupling to droplet optical resonators," *Lab on a Chip*, vol. 13, no. 5, pp. 826–833, 2013.

[54] Z. Ballard, M. D. Baaske, and F. Vollmer, "Stand-off biodetection with free-space coupled asymmetric microsphere cavities," *Sensors*, vol. 15, no. 4, pp. 8968–8980, 2015.

[55] T. A. Birks and Y. W. Li, "The shape of fiber tapers," *Journal of Lightwave Technology*, vol. 10, no. 4, pp. 432–438, 1992.

[56] H. S. Haddock, P. Shankar, and R. Mutharasan, "Fabrication of biconical tapered optical fibers using hydrofluoric acid," *Materials Science and Engineering: B*, vol. 97, no. 1, pp. 87–93, 2003.

[57] M. Cai, O. Painter, and K. J. Vahala, "Observation of critical coupling in a fiber taper to a silica-microsphere whispering-gallery mode system," *Physical Review Letters*, vol. 85, no. 1, p. 74, 2000.

[58] S. Spillane, T. Kippenberg, O. Painter, and K. Vahala, "Ideality in a fiber-taper-coupled microresonator system for application to cavity quantum electrodynamics," *Physical Review Letters*, vol. 91, no. 4, p. 043902, 2003.

[59] B. E. Little, J.-P. Laine, and H. A. Haus, "Analytic theory of coupling from tapered fibers and half-blocks into microsphere resonators," *Journal of Lightwave Technology*, vol. 17, no. 4, p. 704, 1999.

[60] M. J. Humphrey, E. Dale, A. Rosenberger, and D. Bandy, "Calculation of optimal fiber radius and whispering-gallery mode spectra for a fiber-coupled microsphere," *Optics Communications*, vol. 271, no. 1, pp. 124–131, 2007.

[61] J. C. Knight, G. Cheung, F. Jacques, and T. Birks, "Phase-matched excitation of whispering-gallery-mode resonances by a fiber taper," *Optics Letters*, vol. 22, no. 15, pp. 1129–1131, 1997.

[62] K. A. Knapper, K. D. Heylman, E. H. Horak, and R. H. Goldsmith, "Chip-scale fabrication of high-q all-glass toroidal microresonators for single-particle label-free imaging," *Advanced Materials*, vol. 28, no. 15, pp. 2945–2950, 2016.

[63] F. Monifi, J. Friedlein, Ş. K. Özdemir, and L. Yang, "A robust and tunable add–drop filter using whispering gallery mode microtoroid resonator," *Journal of Lightwave Technology*, vol. 30, no. 21, pp. 3306–3315, 2012.

[64] Y. Z. Yan, S. B. Yan, G. Q. Jiang, Z. Ji, S. H. Wang, J. J. Xiong, and W. D. Zhang, "Fabrication of planar microtoroid cavities using high-power laser," in *Advanced Materials Research*, vol. 60, pp. 347–352, Trans Tech Publ, 2009.

[65] X. Zhang and A. M. Armani, "Silica microtoroid resonator sensor with monolithically integrated waveguides," *Optics Express*, vol. 21, no. 20, pp. 23592–23603, 2013.

[66] A. M. Jones, C. T. DeRose, A. L. Lentine, A. Starbuck, A. T. Pomerene, and R. A. Norwood, "Racetrack resonator as a loss measurement platform for photonic components," *Optics Express*, vol. 23, no. 22, pp. 28883–28895, 2015.

[67] Y.-X. Yin, X.-J. Yin, X.-P. Zhang, G.-W. Yan, Y. Wang, Y.-D. Wu, J.-M. An, L.-L. Wang, and D.-M. Zhang, "High-q-factor silica-based racetrack microring resonators," in *Photonics*, vol. 8, pp. 43–, MDPI, 2021.

[68] L. Zhang, L. Jie, M. Zhang, Y. Wang, Y. Xie, Y. Shi, and D. Dai, "Ultrahigh-q silicon racetrack resonators," *Photonics Research*, vol. 8, no. 5, pp. 684–689, 2020.

[69] M. O. Scully, "Collimated unidirectional laser beams from notched elliptical resonators," *Proceedings of the National Academy of Sciences*, vol. 107, no. 52, pp. 22367–22368, 2010.

[70] F. V. Antolinez, J. M. Winkler, P. Rohner, S. J. Kress, R. C. Keitel, D. K. Kim, P. Marqués-Gallego, J. Cui, F. T. Rabouw, D. Poulikakos, *et al.*, "Defect-tolerant plasmonic elliptical resonators for long-range energy transfer," *ACS Nano*, vol. 13, no. 8, pp. 9048–9056, 2019.

[71] C. Li, L. Zhou, S. Zheng, and A. W. Poon, "Silicon polygonal microdisk resonators," *IEEE Journal of selected topics in quantum electronics*, vol. 12, no. 6, pp. 1438–1449, 2006.

[72] M. Hentschel, Q. J. Wang, C. Yan, F. Capasso, T. Edamura, and H. Kan, "Emission properties of electrically pumped triangular shaped microlasers," *Optics Express*, vol. 18, no. 16, pp. 16437–16442, 2010.

[73] C. Wang, M. Zhang, B. Stern, M. Lipson, and M. Lončar, "Nanophotonic lithium niobate electro-optic modulators," *Optics Express*, vol. 26, no. 2, pp. 1547–1555, 2018.

[74] V. Kavungal, G. Farrell, Q. Wu, A. K. Mallik, and Y. Semenova, "Thermo-optic tuning of a packaged whispering gallery mode resonator filled with nematic liquid crystal," *Optics Express*, vol. 26, no. 7, pp. 8431–8442, 2018.

[75] A. Jonáš, Z. Pilát, J. Ježek, S. Bernatová, T. Fořt, P. Zemánek, M. Aas, and A. Kiraz, "Thermal tuning of spectral emission from optically trapped liquid-crystal droplet resonators," *Journal of the Optical Society of America B*, vol. 34, no. 9, pp. 1855–1864, 2017.

[76] V. Anand, S. Mathew, B. Samuel, P. Radhakrishnan, and M. Kailasnath, "Thermo-optic tuning of whispering gallery mode lasing from a dye-doped hollow polymer optical fiber," *Optics Letters*, vol. 42, no. 15, pp. 2926–2929, 2017.

[77] B. J. Eggleton, B. Luther-Davies, and K. Richardson, "Chalcogenide photonics," *Nature Photonics*, vol. 5, no. 3, pp. 141–148, 2011.

[78] M. D. Pelusi, V. G. Ta'eed, L. Fu, E. Magi, M. R. Lamont, S. Madden, D.-Y. Choi, D. A. Bulla, B. Luther-Davies, and B. J. Eggleton, "Applications of highly-nonlinear chalcogenide glass devices tailored for high-speed all-optical signal processing," *IEEE Journal of Selected Topics in Quantum Electronics*, vol. 14, no. 3, pp. 529–539, 2008.

[79] F. F. Schlich, P. Zalden, A. M. Lindenberg, and R. Spolenak, "Color switching with enhanced optical contrast in ultrathin phase-change materials and semiconductors induced by femtosecond laser pulses," *ACS Photonics*, vol. 2, no. 2, pp. 178–182, 2015.

[80] G. Bakan, S. Ayas, E. Ozgur, K. Celebi, and A. Dana, "Thermally tunable ultrasensitive infrared absorption spectroscopy platforms based on thin phase-change films," *ACS Sensors*, vol. 1, no. 12, pp. 1403–1407, 2016.

[81] G. Bakan, S. Ayas, T. Saidzoda, K. Celebi, and A. Dana, "Ultrathin phase-change coatings on metals for electrothermally tunable colors," *Applied Physics Letters*, vol. 109, no. 7, p. 071109, 2016.

[82] V. Weidenhof, I. Friedrich, S. Ziegler, and M. Wuttig, "Laser induced crystallization of amorphous ge 2 sb 2 te 5 films," *Journal of Applied Physics*, vol. 89, no. 6, pp. 3168–3176, 2001.

[83] I. V. Kabakova, L. Zou, G. A. Brawley, C. Florea, I. D. Aggarwal, J. S. Sanghera, E. C. Mägi, E. Li, and B. J. Eggleton, "Dynamics of photoinduced refractive index changes in as 2 s 3 fibers," *Applied Optics*, vol. 51, no. 30, pp. 7333–7338, 2012.

[84] F. Luan, E. Magi, T. Gong, I. Kabakova, and B. J. Eggleton, "Photoinduced whispering gallery mode microcavity resonator in a chalcogenide microfiber," *Optics Letters*, vol. 36, no. 24, pp. 4761–4763, 2011.

[85] A. Faraon, D. Englund, D. Bulla, B. Luther-Davies, B. J. Eggleton, N. Stoltz, P. Petroff, and J. Vučković, "Local tuning of photonic crystal cavities using chalcogenide glasses," *Applied Physics Letters*, vol. 92, no. 4, p. 043123, 2008.

[86] N. Singh, D. D. Hudson, R. Wang, E. C. Mägi, D.-Y. Choi, C. Grillet, B. Luther-Davies, S. Madden, and B. J. Eggleton, "Positive and negative phototunability of chalcogenide (amtir-1) microdisk resonator," *Optics Express*, vol. 23, no. 7, pp. 8681–8686, 2015.

[87] E. Ozgur, E. Huseyinoglu, and A. Dana, "Wafer-scale arrays of high-q silica optical microcavities," *Applied Optics*, vol. 56, no. 9, pp. 2489–2493, 2017.

[88] E. Huseyinoglu, E. Özgür, G. Bakan, B. Ortaç, and A. Dana, "Permanent tuning of optical resonant modes of chalcogenide-coated microresonators," *Applied Optics*, vol. 59, no. 16, pp. 4814–4820, 2020.